AFOSR-TR- ~~ 60

FR-21538
October 1992

②

FIBER COATING BY SPUTTERING FOR HIGH TEMPERATURE COMPOSITES

FINAL TECHNICAL REPORT

PERIOD OF PERFORMANCE
15 MAY 1989 THROUGH 14 AUGUST 1992

DTIC
ELECTE
NOV 2 5 1992
S A D

SPONSORED BY
DEFENSE ADVANCED RESEARCH PROJECTS AGENCY
ARLINGTON, VA 22203
ARPA ORDER NUMBER 6838
MANAGED BY AFOSR UNDER CONTRACT NUMBER F49620-89-C-0066

M.L. Emiliani
Program Manager &
Principal Investigator

Pratt & Whitney
Government Engines & Space Propulsion
P.O. Box 109600
Mail Stop 706-06
West Palm Beach, FL 33410-9600
(407)796-6716

92-30161

92 11 24 024

6c. ADDRESS *(City, State, and ZIP Code)*	10. SOURCE OF FUNDING NUMBERS			
Bolling Air Force Base Building 410 Washington, DC 20332-6448	PROGRAM ELEMENT NO. 61102 S	PROJECT NO. 6838	TASK NO. 00	WORK UNIT ACCESSION NO.

11. TITLE *(Include Security Classification)*

Fiber Coating by Sputtering for High Temperature Composites

12. PERSONAL AUTHOR(S)

M. L. Emiliani

13a. TYPE OF REPORT Final Technical	13b. TIME COVERED FROM 5/15/89 TO 8/14/92	14. DATE OF REPORT *(Year, Month, Day)* 1992, 10, 15	15. PAGE COUNT 74

16. SUPPLEMENTARY NOTATION

17.	COSATI CODES		18. SUBJECT TERMS *(Continue on reverse if necessary and identify by block number)*
FIELD	GROUP	SUB-GROUP	sputtering, coating, debond, composites
			fracture energy, fracture toughness,
			identation

19. ABSTRACT *(Continue on reverse if necessary and identify by block number)*

The objective of this activity was to support researchers at the University of California at Santa Barbara in their development of micromechanics models and new or improved high temperature composite systems. This was achieved through the application of sputtered and sol-gel coatings onto monolithic metal and ceramic foils and plates, respectively, as well as high strength monofilament ceramic fibers. The base program aided in the identification and deposition numerous different types of coatings for the several composite systems under evaluation at UCSB. At the conclusion of the base program, promising composite systems were identified for further study and processing via continuous sputtering and sol-gel processing. In addition to providing coated materials to UCSB, P&W also engaged in focused studies of coatings found to be promising by UCSB researchers. The base program study examined as-sputtered Y_2O_3 coatings deposited onto various substrates to understand why this coating improves the toughness of Nb-reinforced TiAl. The option program study characterized tungsten and molybdenum coatings applied by hollow cathode magnetron sputtering, and aluminum oxide coatings applied by sol-gel processing.

20. DISTRIBUTION / AVAILABILITY OF ABSTRACT ☒ UNCLASSIFIED/UNLIMITED ☐ SAME AS RPT. ☐ DTIC USERS	21. ABSTRACT SECURITY CLASSIFICATION UNCLASSIFIED	
22a. NAME OF RESPONSIBLE INDIVIDUAL Larry Burggraf	22b. TELEPHONE *(Include Area Code)* (202) 767-4960	22c. OFFICE SYMBOL NE

FINAL TECHNICAL REPORT

REPORTING PERIOD: 15 MAY 1989 TO 14 AUGUST 1992

ARPA ORDER NUMBER: 6838

PROGRAM CODE NUMBER: 9D10

CONTRACTOR: Pratt & Whitney, United Technologies Corporation

DATE OF CONTRACT: 15 May 1989

EXPIRATION DATE OF CONTRACT: 14 August 1992

CONTRACT NUMBER: F49620-89-C-0066

PROGRAM MANAGER & PRINCIPAL INVESTIGATOR: M.L. Emiliani

TITLE: "Fiber Coating by Sputtering for High Temperature Composites"

DTIC QUALITY INSPECTED 4

DISCLAIMER
The views and conclusions contained in this document are those of the author(s) and should not be interpreted as necessarily representing the official policies or endorsements, either expressed or implied, of the Defense Advanced Research Projects Agency or the U.S. Government.

Accesion For	
NTIS CRA&I	☑
DTIC TAB	☐
Unannounced	☐
Justification	
By	
Distribution /	
Availability Codes	
Dist	Avail and/or Special
A-1	

TABLE OF CONTENTS

TABLE OF CONTENTS, CONTINUED

1.0 SUMMARY

Objective and Scope

This contract is part of a three-year DARPA-sponsored initiative in fiber coatings for structural composites that began in mid-1989. The purpose of the initiative was to provide a rational basis for the design and fabrication of fiber reinforced intermetallic and ceramic matrix composites with high strength at elevated temperature. In particular, interface coatings would be developed for selected composite systems that provided the requisite interfacial thermochemical and thermomechanical properties. The latter is manifest in the ability of the fiber/matrix interface to debond in the presence of a crack, as aided by interfacial coatings.

This multidisciplinary program sponsored activities in the areas of thermochemical modeling, mechanical modeling, fabrication and testing of composite coupons, and coatings technology. The coatings technology focused on continuous fiber processing via physical vapor deposition (sputtering), chemical vapor deposition, and sol-gel.

The objective of the Pratt & Whitney (P&W) activity was to support DARPA-sponsored researchers at the University of California at Santa Barbara (UCSB) in their development of micromechanics models and new or improved high temperature composite systems. This was achieved through the application of sputtered and sol-gel coatings onto monolithic metal and ceramic foils and plates, respectively, as well as high strength monofilament ceramic fibers. Pratt & Whitney's activity was split into two components: base and option programs, each approximately 18 months in duration.

The base program aided in the identification and deposition numerous different types of coatings for the several composite systems under evaluation at UCSB. Both single and dual layer coatings were applied exclusively by batch coating. At the conclusion of the base program, promising composite systems were selected for further study. The option program focused on the deposition of downselected single and dual layer coatings via continuous sputtering and sol-gel processing. Included in both programs was extensive process development to deposit high quality coatings by both batch and continuous techniques. The Appendix lists all of the coatings deposited in the base and option programs delivered to researchers at UCSB.

In addition to providing coated materials to UCSB, P&W also engaged in focused studies of coatings found to be promising by UCSB researchers. The base program study (Section 3.0) examined as-sputtered Y_2O_3 coatings deposited onto various substrates to understand why this coating improves the toughness of Nb-reinforced TiAl. The coating was characterized by numerous techniques to correlate the fracture toughness and debonding characteristics of as-deposited coatings on niobium versus that found in hot pressed TiAl/Nb laminates. Additionally, this research also attempted to determine the general attributes of successful debond coatings so that candidate coatings can be selected using predictive guidelines. The option program study (Section 4.0) characterized tungsten and molybdenum coatings applied by hollow cathode magnetron sputtering, and aluminum oxide coatings applied by sol-gel processing.

It is worth noting that Industry/University collaboration was excellent, and contributed greatly to the success of both DARPA-sponsored programs.

Results

Reactively sputtered Y_2O_3 coatings 1-2 μm thick were characterized and found to consist of columnar grains of stoichiometric BCC Y_2O_3 with $a_0 = 1.0602$ nm. Nanoindenter® and Vickers indentation tests were performed to correlate the fracture toughness and debond characteristics of as-deposited Y_2O_3 coatings on Al_2O_3 and polycrystalline niobium, and Nb coatings on single crystal Y_2O_3, to that found in TiAl/Nb and Al_2O_3/Al_2O_3 laminates produced and evaluated by UCSB. The calculated fracture toughness of sputtered Y_2O_3 on sapphire was similar to reported values for bulk Y_2O_3. However, a wide variation in interfacial fracture toughness was obtained by indentation methods, and is attributed to the microstructure of as-deposited coatings and to weak bonding between as-deposited yttria and the substrates. These results indicate that yttrium oxide coatings applied to niobium have an atomically sharp interface that has a lower fracture energy compared to Nb/Al_2O_3, resulting in improved interfacial debonding and composite fracture toughness.

The success of a particular material as a debond coating was found to depend upon several factors including coating thickness, surface and bulk impurities, local stress state, coating mechanical properties, bond strength between the coating and reinforcement or matrix, thermodynamic stability, and microstructure. An attempt was made to correlate these interdependent factors, but was not successful. It is apparent that additional studies must be performed to better quantify the attributes common to fiber/coating/matrix systems that exhibit desirable fracture behavior, and enable the use of predictive guidelines to select debond and protective coatings.

Dual layer Al_2O_3/Mo and Al_2O_3/W coated sapphire monofilament fiber were characterized by transmission electron microscopy and found to have an outer coating of ~3 μm of sol-gel alumina and an ~1 μm inner coating of either molybdenum or tungsten. The sol-gel outer coating consisted of microcrystalline gamma alumina (cubic spinel). Both the Mo and W coatings consisted of columnar grains, 20-40 nm in diameter, and extending across the full coating width.

Oxygen and carbon impurities were detected by Auger electron spectroscopy in the Mo coating, while only oxygen was found in the W coating. Oxygen signals were greater near the sol-gel alumina and sapphire fiber interfaces. Evidence for 3-6 nm regions of tungsten oxide in the W coating near the sapphire monofilament was found by low resolution lattice imaging and selected area diffraction. Both the Mo and W coatings exhibited a tendency for grain orientations with <101> parallel to the fiber radius and <110> parallel to the [0001] fiber axis.

The sol-gel Al_2O_3/Mo and sol-gel Al_2O_3/W interfaces were extremely friable, while the corresponding interfaces with the sapphire monofilament were extremely adherent. Oxide interfaces adjacent to the metal coatings contained significantly higher concentrations of oxygen than in the bulk, presumably due to sputtering and sol-gel processing conditions that exposed the fiber to ~650°C.

Additional results can be found in the Appendix, which lists several publications reporting work performed using the coated materials provided to UCSB under this contract.

2.0 INTRODUCTION

Fiber coatings will likely be required for brittle matrix composites in order to improve composite fracture toughness or reduce fiber/matrix interaction at elevated temperatures. Coatings have been successfully used to improve the thermochemical compatibility or fracture behavior of a few ductile and brittle matrix systems including boron or SiC reinforced titanium or aluminum alloys and SiC reinforced lithium aluminosilicate glass. The purpose of this research is to identify protective and debond coatings that improve the toughness of intermetallic and ceramic matrix composites, and contribute to a generalized understanding of the requirements for successful debond coatings.

The present study is part of a larger DARPA-sponsored initiative in fiber coatings for structural composites. The purpose of the initiative is to provide a rational basis for the design and fabrication of fiber reinforced intermetallic and ceramic matrix composites with high strength at elevated temperature. In particular, interface coatings would be developed for selected composite systems that provided the requisite interfacial thermochemical and thermomechanical properties. This multidisciplinary program sponsored activities in the areas of thermochemical modeling, mechanical modeling, fabrication and testing of composite coupons, and coatings technology. The coatings technology focused on continuous fiber processing via physical vapor deposition (sputtering), chemical vapor deposition, and sol-gel.

The objective of the Pratt & Whitney (P&W) activity was to support researchers at the University of California at Santa Barbara (UCSB) in their development of micromechanics models and new or improved high temperature composite systems. This was achieved through the application of sputtered and sol-gel coatings onto monolithic metal and ceramic foils and plates, respectively, as well as high strength monofilament ceramic fibers. The base program aided in the identification and deposition numerous different types of coatings for the several composite systems under evaluation at UCSB. At the conclusion of the base program, promising composite systems were identified for further study and processing via continuous sputtering and sol-gel processing.

In addition to providing coated materials to UCSB, P&W also engaged in focused studies of coatings found to be promising by UCSB researchers. The base program study (Section 3.0) examined as-sputtered Y_2O_3 coatings deposited onto various substrates to understand why this coating improves the toughness of Nb-reinforced TiAl. The option program study (Section 4.0) characterized tungsten and molybdenum coatings applied by hollow cathode magnetron sputtering, and aluminum oxide coatings applied by sol-gel processing. Industry/University collaboration was excellent throughout, and contributed greatly to the success of both DARPA-sponsored programs.

3

3.0 BASE PROGRAM FINAL REPORT

DEBOND COATING REQUIREMENTS FOR
BRITTLE MATRIX COMPOSITES

3.1 INTRODUCTION

Fiber coatings will likely be required for brittle matrix composites in order to improve composite fracture toughness or reduce fiber/matrix interaction at elevated temperatures [1-4]. Coatings have been successfully used to improve the thermochemical compatibility or fracture behavior of a few ductile and brittle matrix systems including boron [4] or SiC [5] reinforced titanium or aluminum alloys and SiC reinforced lithium aluminosilicate glass [2]. The purpose of this research is to identify protective and debond coatings that improve the toughness of intermetallic and ceramic matrix composites, and contribute to a generalized understanding of the requirements for successful debond coatings. The latter may allow the development of predictive guidelines for future coating selections in other composite systems.

Two composite systems, niobium reinforced TiAl and Al_2O_3 reinforced Al_2O_3, have exhibited improved fracture toughness through the use of chemically compatible interfacial coatings [6,7]. An elastic indentation technique, Hertzian cone cracking, has been used to assess the specific fracture energy (Γ_i) of Al_2O_3 laminate composites containing various interfacial coatings [7]. Yttria interfacial coatings, applied by sputtering or sol-gel, exhibit a specific fracture energy of 25 J/m^2. This is approximately 5 times greater than that achieved with sputtered molybdenum coatings [8], and results in incomplete debonding. Reaction between the Al_2O_3 substrate and Y_2O_3 to form YAG ($Y_3Al_5O_{12}$) was found to be responsible for the high fracture energy.

The debonding characteristics of a model Nb-reinforced TiAl composite have been evaluated using uncoated Nb, Al_2O_3-coated Nb, and Y_2O_3-coated Nb [6]. Uniaxial tension tests of precracked TiAl/Nb laminates were performed *in situ* in the scanning electron microscope. The Y_2O_3 coating produced the lowest specific fracture energy, thus allowing extensive debonding which permitted plastic deformation of the Nb over a large volume and resulting in a high work of rupture. The measured fracture toughness is thought to be due to the presence of an atomically sharp Y_2O_3/Nb interface similar to that found in Al_2O_3/Nb couples [9].

The present study examines as-sputtered Y_2O_3 coatings deposited onto rock salt (NaCl), single crystal (0001) Al_2O_3, and polycrystalline niobium to better understand why this coating improves the toughness of Nb-reinforced TiAl. As-deposited yttria coatings were characterized by scanning electron microscopy (SEM), energy dispersive X-ray spectroscopy (EDXS), transmission electron microscopy (TEM), X-ray photoelectron spectroscopy (XPS), secondary ion mass spectroscopy (SIMS), X-ray diffraction (XRD), and indentation techniques. Nanoindenter® and Vickers indentation tests [10] were used to determine the fracture toughness (K_c), interfacial fracture toughness ($K_{c,i}$), and specific fracture energy (Γ_i) of as-sputtered coatings. The results were compared to that found for diffusion bonded Al_2O_3/Al_2O_3 and TiAl/Nb laminates [6,7]. In addition, niobium coatings 1-2 μm thick were deposited onto polished single crystal Y_2O_3 wafers by sputtering to compare debonding behavior. A TEM study was also performed on Y_2O_3-coated Nb-reinforced TiAl laminate.

3.2 EXPERIMENTAL

3.2.1 Sputtered Coatings

Yttrium oxide coatings were deposited onto polished single crystal Al_2O_3 4 mm thick, commercial purity polycrystalline niobium foil 125 μm thick, and rock salt substrates. Prior to coating, Al_2O_3 and Nb substrates were ultrasonically cleaned in soapy water, rinsed in water, rinsed in ethyl alcohol, and dried by forced hot air. Sputtering was performed in a Plasma-Therm Model AMNS-1000E 1000 watt radio frequency diode sputtering unit equipped with dual opposed six inch diameter yttrium metal targets (99.9 wt.% purity). A 142 μm monofilament SiC fiber (Textron SCS-6) was also coated to determine coating thickness and microstructure by fractography. Yttrium oxide coatings were deposited by reactive sputtering using a 50%-50% mixture of research grade argon and oxygen at a total working gas pressure of $P_T = 6$ millitorr (mtorr). The substrates were not externally cooled, heated, or biased during sputtering. The top and bottom targets were maintained at 3000 volts and 500 volts, respectively. Deposition of Y_2O_3 for ~10 hrs resulted in coatings 1-2 μm thick. The only equilibrium oxide phase formed according to the Y-O phase diagram is Y_2O_3 [11].

Niobium coatings were sputter deposited onto polished Y_2O_3 wafers ~0.5 mm thick using research grade argon at $P_T = 6$ mtorr and 99.5 wt.% purity niobium metal targets maintained at 5000 volts and 500 volts. The resultant coatings were 3-4 μm thick.

3.2.2 Indentation Tests to Determine Coating Hardness & Elastic Modulus

The hardness and elastic modulus of as-sputtered coatings was determined using a Nano Instruments Inc. Nanoindenter® [12]. This instrument is a sub-micron indentation tester that uses a triangular diamond indenter with the same projected area to-depth ratio as the Vickers square pyramid indenter. The maximum load that can be applied by this technique is 0.1 N. Coating hardness and modulus was determined by taking five or more indentations at depths ranging from 0.04-0.7 μm.

3.2.3 Indentation Tests to Determine Coating Fracture Properties

Nanoindenter® and Vickers indentation tests were used to initiate coating fracture or interfacial debonding in Y_2O_3-coated Al_2O_3, Y_2O_3-coated Nb, and Nb-coated Y_2O_3. All coatings were evaluated in the as-sputtered condition. Loads greater than 0.1 N and up to 10 N were applied using a Vickers diamond indenter. Six measurements are typically made at each indentation depth. While there are numerous relationships for obtaining quantitative values of fracture toughness [13], only selected equations are applied in the present study. The equations used to determine coating fracture toughness (K_c), interfacial fracture toughness ($K_{c,i}$), and specific fracture energy (Γ_i) are briefly reviewed.

The fracture toughness of thin coatings can be determined by measuring radial crack lengths and the dimensions of indentations made by indentation tests [13,14]. Equations to determine fracture toughness have been empirically determined assuming the crack shape is radial-median (i.e. "halfpenny") or Palmqvist [14]. The critical indentation and crack related-dimensions are the indentation half-diagonal length, a, radial surface crack length, C, and the Palmqvist surface crack length, l (Figure 1). Equations to determine fracture toughness take the following general form for halfpenny (Equation 1) and Palmqvist (Equation 2) shaped cracks [14]:

5

$$K_C = k \frac{P}{aC^{1/2}} \qquad\qquad \text{Equation 1}$$

$$K_C = k\ (E/H_v)^{2/5} \frac{P}{al^{1/2}} \qquad\qquad \text{Equation 2}$$

where k is a constant typically between 0.001 and 0.5, P is the applied indenter load (N), H_v is the Vickers microhardness (GPa), E is the elastic modulus (GPa), and a, C, l are the indentation and crack related-dimensions (m), as shown in Figure 1. Values of K_C for selected glass and oxide ceramics have been compared to K_{Ic} fracture toughness of the same materials by traditional mechanical testing techniques [13]. The average results for both types of test were reported to be within ±30%. Thus, the values of fracture toughness obtained by indentation methods are comparable to that obtained by more elaborate mechanical tests. In general, averaged values of fracture toughness calculated using either halfpenny or Palmqvist-based equations yield similar results.
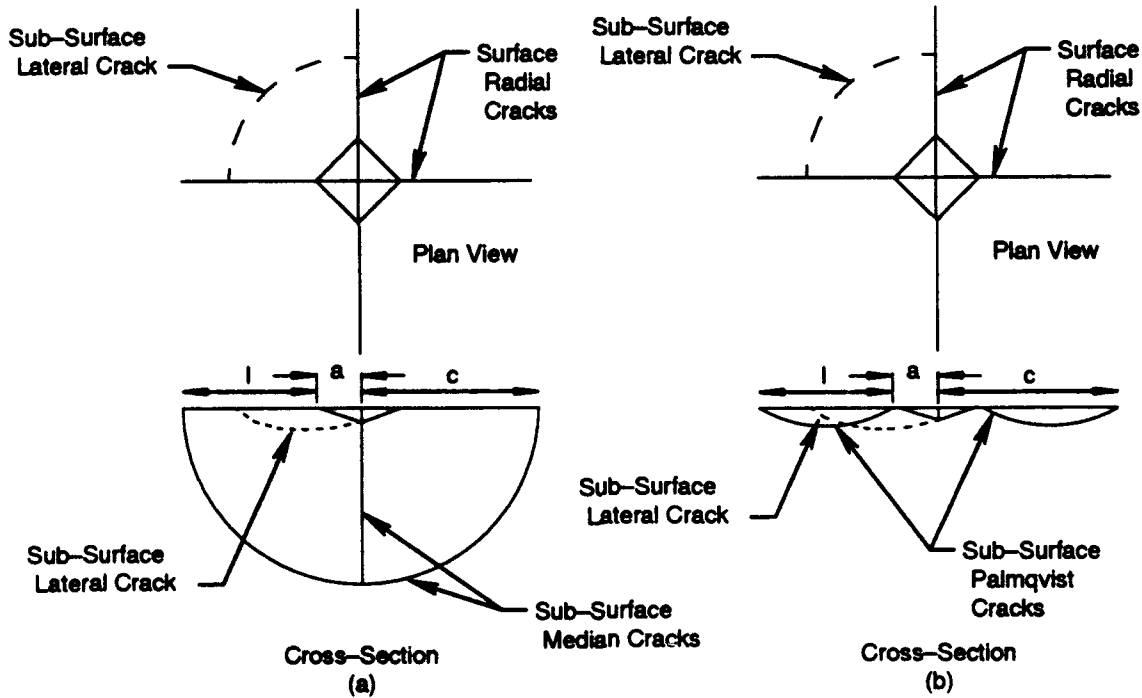

Figure 1. Schematic diagrams of Vickers indentations resulting in the formation of radial-median (a) and Palmqvist cracks (b) [14].

The interfacial fracture toughness ($K_{c,i}$) of thin coatings can also be determined from indentation tests [15]. This information also provides a measure of coating adhesion to the substrate, and is required to determine the specific fracture energy, Γ_i, of the interface. The interfacial fracture toughness can be represented by:

$$K_{c,i} = k \, t^{3/2} \, H_v^{1/2} \, \frac{[1 - P_o/P] \, P^{1/2}}{C^2} \qquad \text{Equation 3}$$

where k is a constant determined to be 0.16 in the present study, t is the coating thickness (m), H_v is the Vickers hardness of the coating (GPa), P_o is the threshold load for crack formation (MN), P is the maximum indenter load (MN), and C is the lateral crack length (m). Knowledge of the fracture toughness allows calculation of the specific fracture energy, Γ_i, and provides a basis for understanding the contribution of coatings to interfacial debonding. The fracture toughness for a Mode I (tensile) crack is [16]:

$$K_{Ic} = Y \, \sigma \, [\pi \, a^{1/2}] \qquad \text{Equation 4}$$

where Y is the geometric crack factor (typically $= \pi^{1/2}$ for a halfpenny-shaped crack), σ is the applied stress (N), and a is the half-crack length (m). The Griffith relationship for plane (biaxial) stress ($\sigma_z = 0$) is:

$$\sigma = (2 \, E \, \gamma_s/\pi \, a)^{1/2} \qquad \text{Equation 5}$$

Combining Equations 4 and 5 yields the specific fracture energy:

$$\gamma_s = \frac{K^2_{Ic}}{2 \, Y \, E} = \Gamma_i \qquad \text{Equation 6}$$

Thus, the specific fracture energy, in J/m^2, depends only upon the fracture toughness (where $K_{Ic} = K_c$ or $K_{c,i}$), geometric crack factor, and elastic modulus of the coating. The latter may vary depending upon thickness.

3.3 RESULTS

3.3.1 Characterization of Sputtered Y_2O_3 Coatings

X-ray diffraction of yttria-coated sapphire wafer was performed using a Huber Model 651 Guinier thin film goniometer. The resulting spectrum corresponds to BCC Y_2O_3 (JCPDS pattern #25-1200), Figure 2. X-ray photoelectron spectroscopy was performed using a PHI Model 5400 multiprobe. The surface contained excess physisorbed hydrocarbon or carbon and oxygen or oxide due to exposure to ambient. Oxygen in the form of OH or H_2O was detected. Argon sputtering to a depth of ~5 nm removed gross contaminants, resulting in decreased C and increased O signals. Additional sputtering to a depth of 10 nm showed only yttrium and oxygen (Figure 3). Secondary ion mass spectroscopy data was obtained using a Kratos Ion Microprobe. SIMS showed that B, C, Al, Si, K, Ti, Fe, Nb, and Nd were present in the coating ~10 nm below the free surface, all at levels of <0.1 at.%.
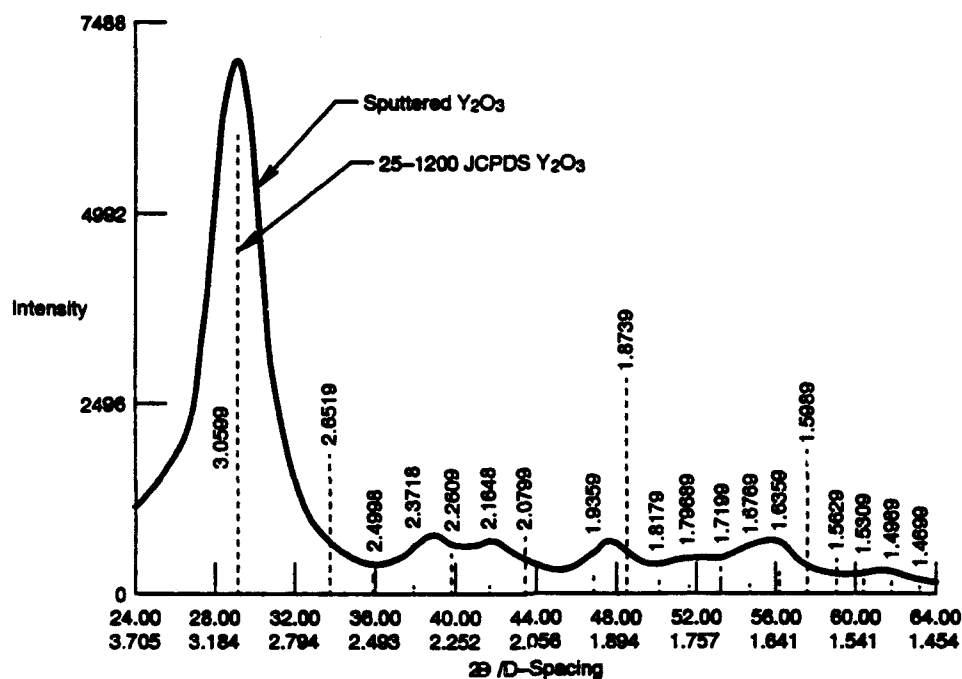
7

Figure 2. X-ray diffraction pattern of reactively sputtered Y_2O_3 showing good correlation with the JCPDS reference pattern (vertical lines).
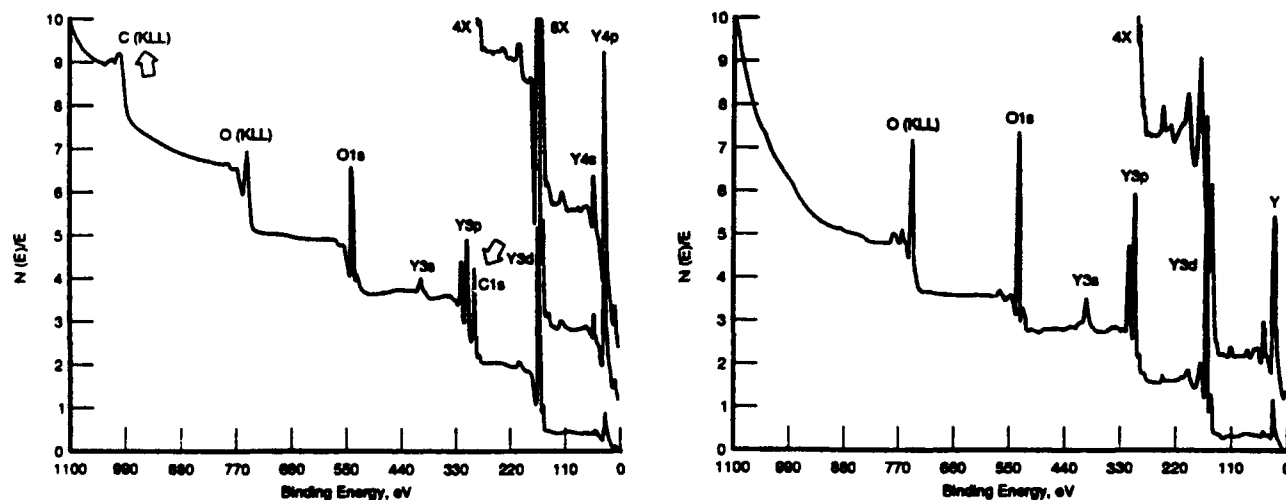

Figure 3. XPS spectra of Y_2O_3 coating. As-received (left), and 10 nm below the free surface (right). The carbon signal is prominent in as-received samples (arrows), while only Y and O are present 10 nm below the free surface.

8

The surface finish of Y_2O_3 coatings on SiC fibers was examined by SEM and found to faithfully replicate the surface finish of the substrate which consists of nodules characteristic of coatings deposited by chemical vapor deposition (Figure 4). Coating microstructure was characterized by SEM of fractured SiC fibers and found to consist of columnar grains which extend through the thickness of the coating. This is typical of that found in sputtered coatings deposited at low homologous temperature (T/T_M, where T = substrate temperature and T_M = melting temperature of Y_2O_3) [17,18]. For T_M (Y_2O_3) = 2400°C and assuming $T_{substrate} \approx$ 300°C, $T/T_M \approx 0.12$. These coatings were found to correspond well to the Zone 1 microstructure as described by Thornton [18].
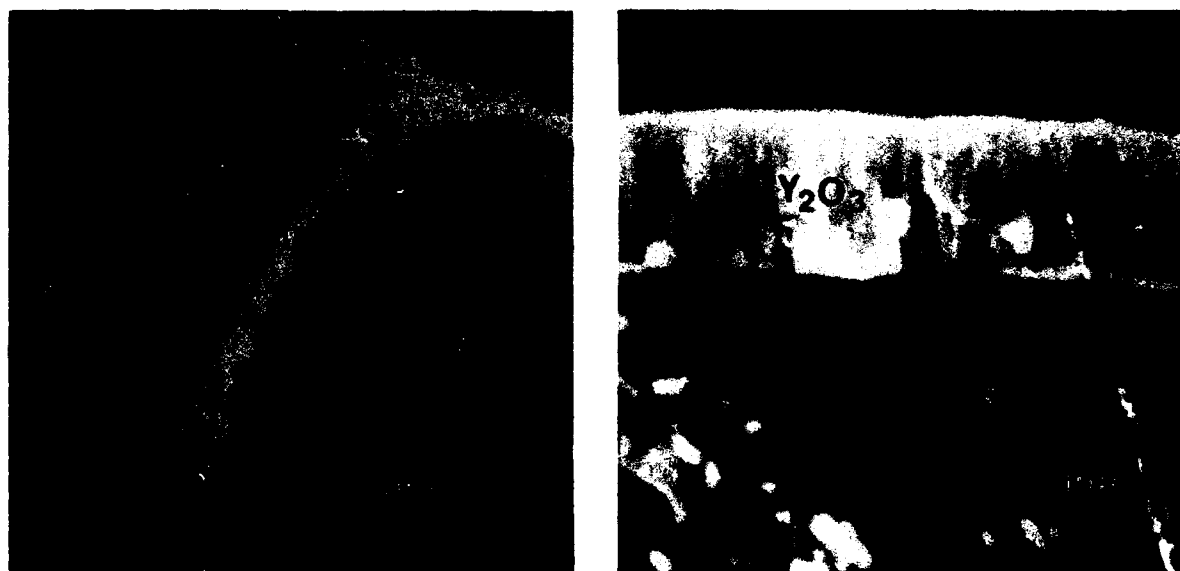
Figure 4. SEM showing the surface finish of as-deposited Y_2O_3 coating which has replicated the surface finish of the SiC fiber (left). SEM micrograph showing the thickness and structure of as-deposited Y_2O_3 coating (right). The columnar morphology of the coating is evident.

Electron transparent Y_2O_3 samples for TEM were produced by depositing a thin coating onto rock salt, dissolving the substrate in water, then collecting the oxide film on a copper grid. Y_2O_3 samples were examined using a Philips 400T at 120 kV and equipped with a Kevex Quantum energy dispersive X-ray spectrometer. Direct imaging of the coating microstructure through-thickness by transmission electron microscopy showed it contained a homogeneous distribution of fine grains 10-30 nm in diameter (Figure 5). Energy dispersive spectroscopy of the coating showed yttrium and oxygen (Figure 6). Selected area electron diffraction patterns (Figure 5, inset) contained well-defined continuous rings with spacings characteristic of body-centered cubic Y_2O_3 (Pearson Symbol cI80, Mn_2O_3 prototype structure), with a lattice parameter of a_o = 1.0602 nm.

Figure 5. Bright field (left) and dark field (right) TEM micrographs of as-sputtered Y_2O_3. Arrows on the selected area diffraction pattern (inset) bracket the two rings used to make the dark field micrograph. The coating consists of BCC Y_2O_3 with a_o = 1.0602 nm.
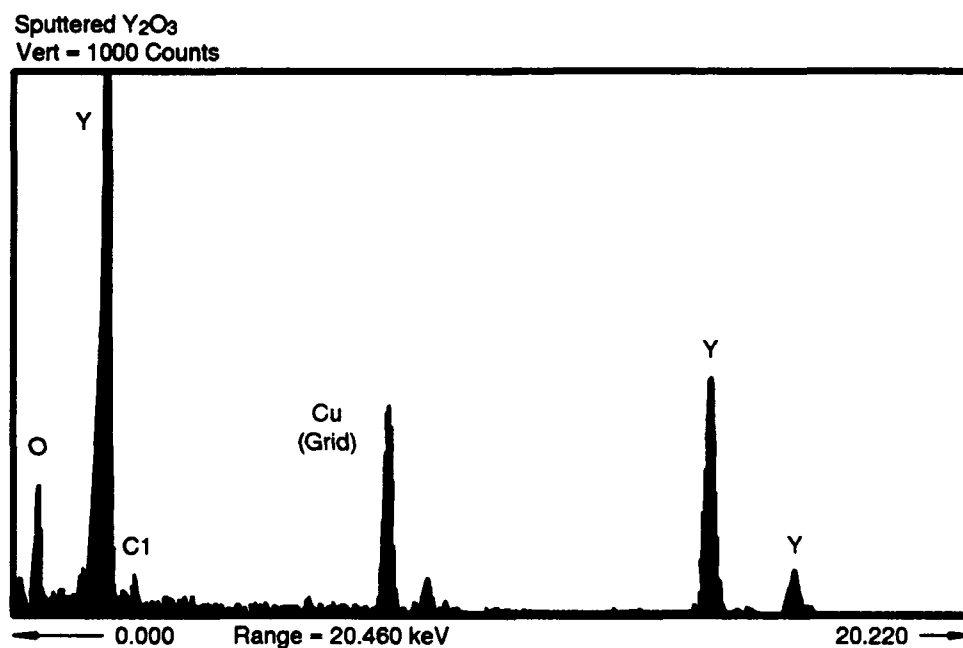

Figure 6. Energy dispersive X-ray spectrum of the Y_2O_3 coating.

10

Yttrium oxide coated niobium foils were diffusion bonded between two TiAl plates in vacuum at 1066°C under a pressure of 10 MPa for 4 hours (Figure 7) [6]. The resulting laminate was prepared for TEM by sectioning small wafers perpendicular to the $TiAl/Y_2O_3/Nb$ interface using a low-speed diamond saw. Most of the samples fractured during sectioning, grinding to final thickness, or ion milling due to the low specific fracture energy of the Y_2O_3/Nb interface.
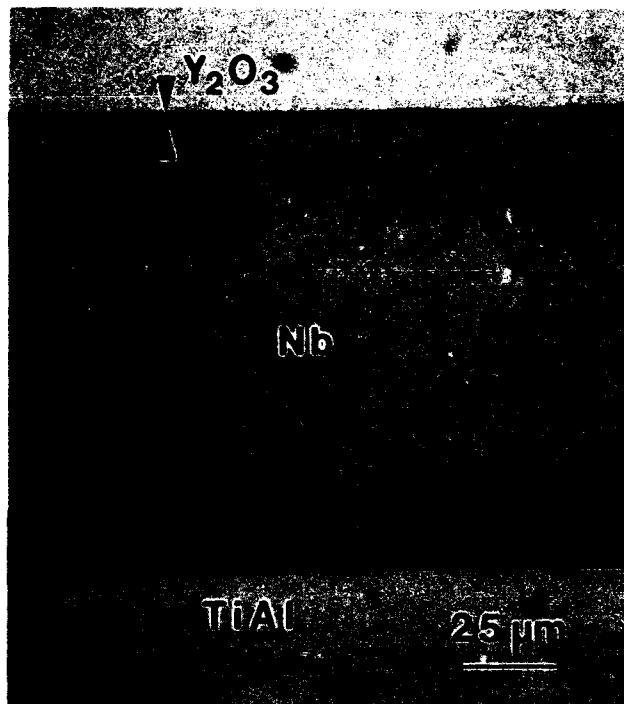

Figure 7. Light micrograph of a TiAl/Nb laminate test specimen after diffusion bonding at 1066°C for 4 hours and 10 MPa pressure. Note the absence of interfacial reaction products.

The interface between Y_2O_3 and Nb is of interest because it is the location where debonding occurs. Unfortunately, it could not be observed due to decohesion of the interface. The $Y_2O_3/TiAl$ interface is more strongly bonded and therefore could be examined by TEM. The most interesting aspect of this interface is the morphology of Y_2O_3 coating (Figure 8), which has been exposed to 1066°C for 4 hours. The Y_2O_3 coating retains a columnar morphology, with columns ~0.15 μm wide and extending through the entire thickness of the coating. Reflections from selected area diffraction patterns contained intense arcs. This, coupled with the shape of individual grains, suggests that the columnar Y_2O_3 grains contain a dense substructure of low-angle grain boundaries that have begun to coalesce. Thus, diffusion bonding resulted in little or no grain growth of the oxide coating. Selected area (Figure 8, inset) and convergent beam electron diffraction (Figure 9) of the coating shows it consists of cubic Y_2O_3 with lattice parameter of $a_o = 1.0602$ nm, and is in agreement with the results for as-deposited Y_2O_3. Direct imaging and EDXS did not reveal extensive chemical reaction between Y_2O_3 and TiAl.
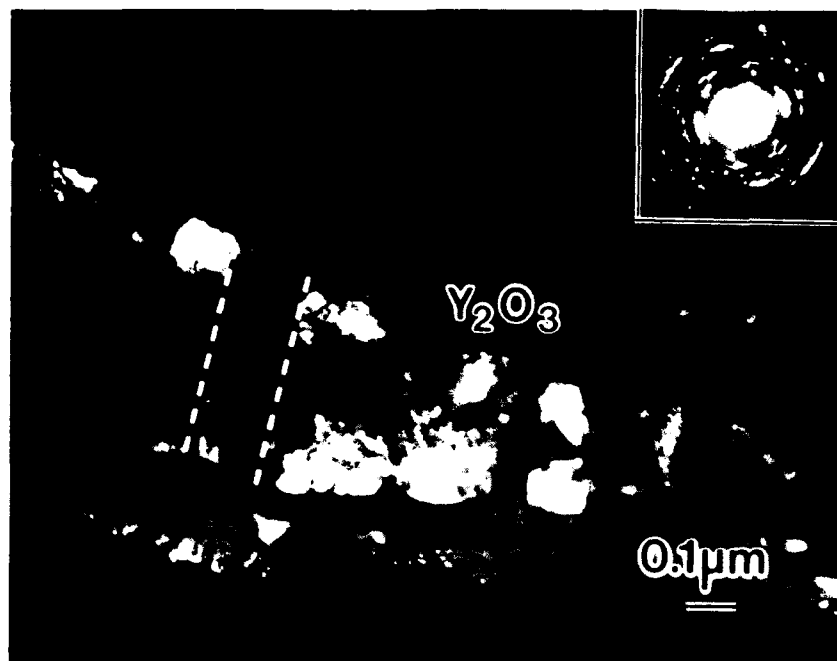
11

Figure 8. TEM micrograph of a portion of the Y_2O_3 coating and selected area electron diffraction pattern (inset) from a TiAl/Nb laminate. Note the grains remain columnar after hot-pressing at 1066°C for 4 hours.
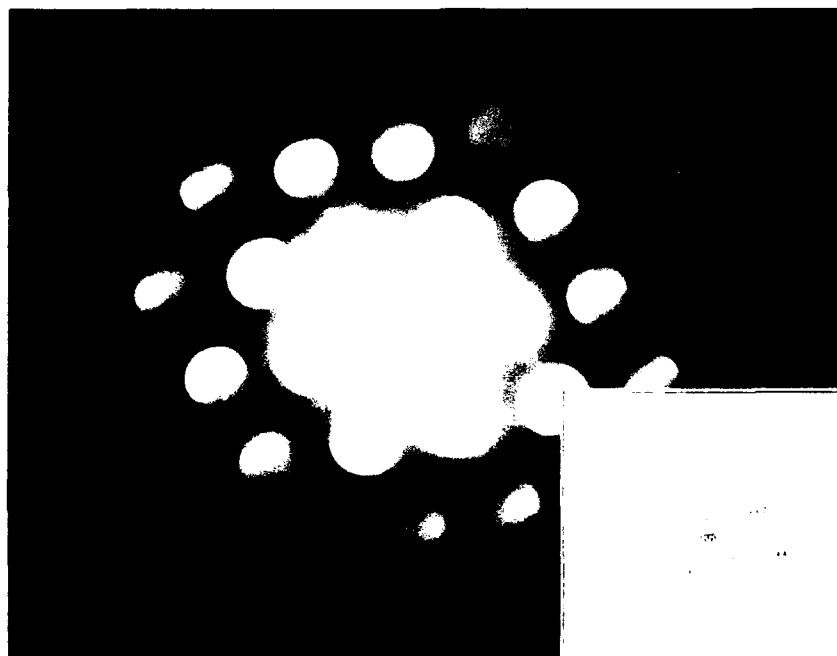

Figure 9. Convergent beam electron diffraction pattern of Y_2O_3 and corresponding computer-generated [110] zone axis pattern.

3.3.2 Indentation-Derived Coating Hardness & Elastic Modulus

The hardness of as-sputtered yttria coatings on polished sapphire substrates was determined using the Nanoindenter® by taking five or more indentations at depths ranging from 0.05-0.5 μm. Figure 10 shows the variation in coating hardness as a function of indentation depth. The rapid increase in hardness with decreasing indentation depth is due to the well-known indentation size effect [19]. However, at indentation depths ≥0.4 μm the hardness remains nearly constant at ~750 kg/mm^2 (7.5 GPa). This is in good agreement with previous results for bulk Y_2O_3 [20].

The hardness of as-sputtered Y_2O_3 coating on commercially pure polycrystalline niobium was also determined using the Nanoindenter® (Figure 11). There is a dramatic decrease at ~0.6 μm depth due to plastic deformation of the soft niobium substrate (film-substrate effect - FSE) [21]. Conversely, a rapid increase in hardness was found at indentation depths <0.1 μm due to the indentation size effect (ISE) [19]. The hardness of the Y_2O_3 coating measured at indentation depths between 0.1 μm < d < 0.5 μm is 800-850 kg/mm^2 (8-8.5 GPa). This is approximately the same hardness as that measured for as-sputtered Y_2O_3 on single crystal Al_2O_3, and agrees with that reported for bulk Y_2O_3 [20,22]. Thus, accurate values of Y_2O_3 coating hardness independent of the substrate material were determined using the Nanoindenter® at indentation depths between 0.1-0.3 μm.

The elastic modulus of Y_2O_3 coatings was also determined using the Nanoindenter® (Figure 12), assuming Poisson's ratio = 0.33. The modulus increases almost linearly from 15-27X10^3 kg/mm^2 (150-270 GPa) throughout the range of indentation depths. The elastic modulus of Y_2O_3 at ~0.5 μm indentation depths approaches that of bulk Al_2O_3 (~350 GPa), indicating that the coating modulus is very sensitive to substrate modulus. The elastic modulus of bulk Y_2O_3 is reported as ~13.4X10^3 kg/mm^2 (134 GPa) [23], and is in agreement with data generated at indentation depths of 0.05-0.1 μm.

The hardness and elastic modulus of Nb coatings on Y_2O_3 were determined from indentations ranging in depth from 0.04-0.7 μm. The hardness increased with increasing indentation depth due to the film-substrate effect (Figure 13). To minimize this effect, the ratio of indentation depth to coating thickness should be d/t < 0.1 (Figure 14a). However, indentations less than 0.4 μm may be influenced by surface roughness (Figure 14b). Because of these factors, the hardness at a depth of ~0.4 μm, H_v ≈ 2.8 GPa, is expected to be representative of the actual hardness of the Nb film. In contrast, the hardness of bulk wrought niobium is ~1.6 GPa [24]. A plot of the elastic modulus of the Nb film versus indentation depth shows less dependence upon substrate effects (Figure 15), and E = 88 GPa at an indentation depth of 0.4 μm. This value is in reasonable agreement with the literature [25].

13
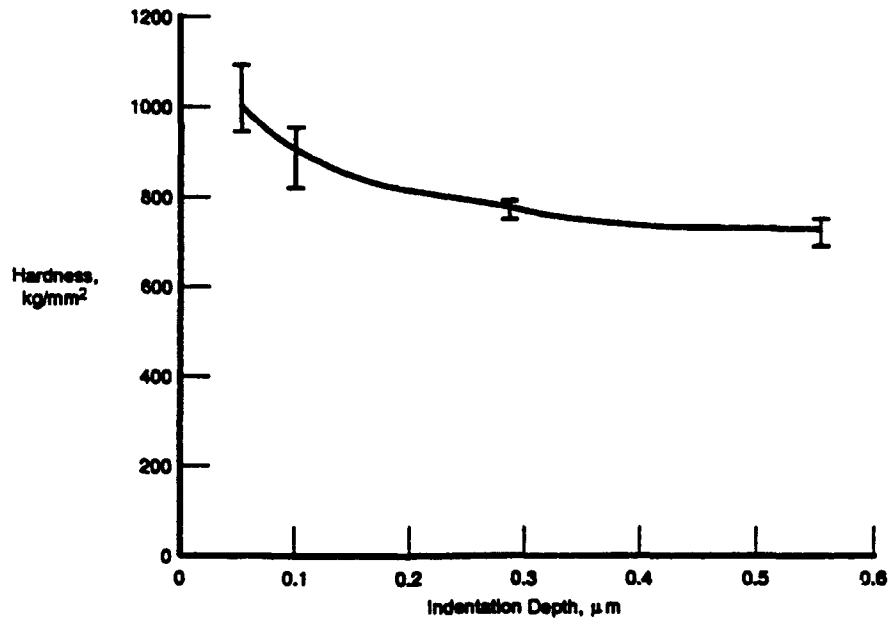
Figure 10. Hardness versus indentation depth as determined by the nanoindentation technique. The hardness of Y_2O_3 at ~0.5 μm deep indentations is ~750 kg/mm^2 (7.5 GPa). Higher hardness at smaller indentation depths are due to the indentation size effect [19].
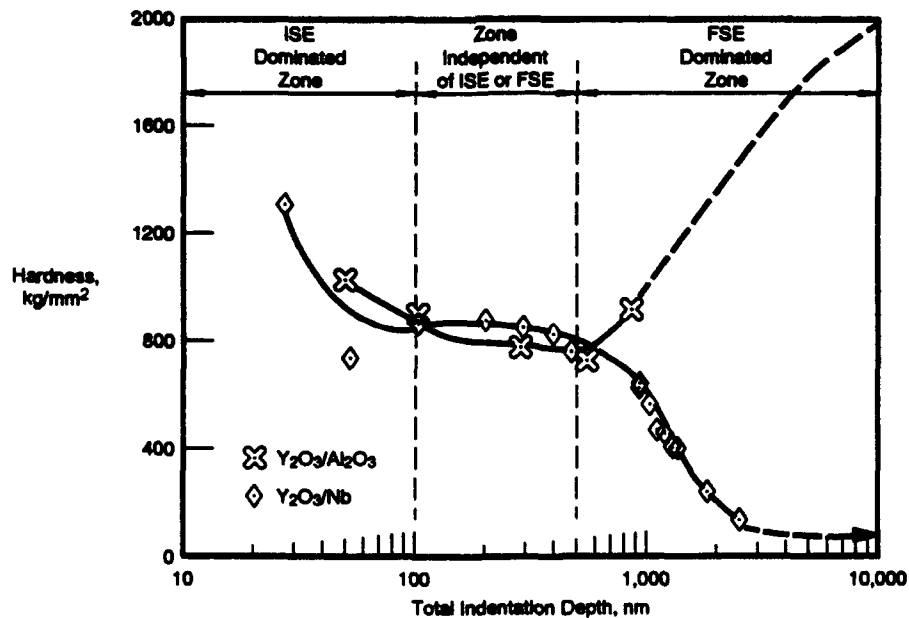
Figure 11. Plot of Nanoindenter® hardness versus indentation depth for as-sputtered Y_2O_3 coating on Al_2O_3 and niobium. High hardness values are obtained at indentation depths <0.1 μm due to the indentation size effect (ISE) [14], while the coating hardness is dominated by interaction with the substrate for d > ~0.8 μm (film-substrate effect - FSE) [21]. Note the good correlation in coating hardness for indentations depths between 0.1 and 0.5 μm.

14
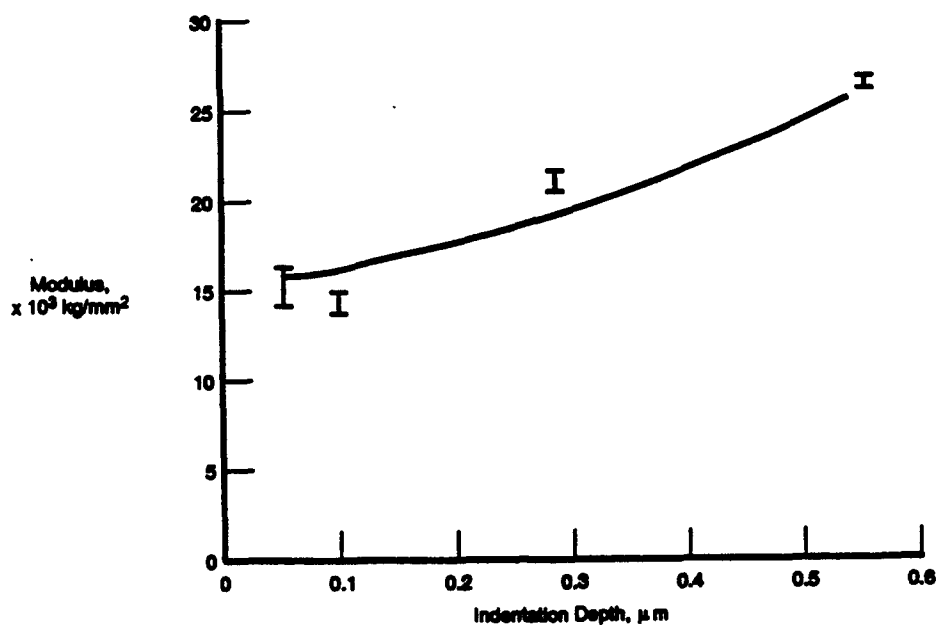
Figure 12. Elastic modulus of Y_2O_3 versus indentation depth. The modulus at small indentation depths (0.05-0.1 μm) is characteristic of bulk Y_2O_3.
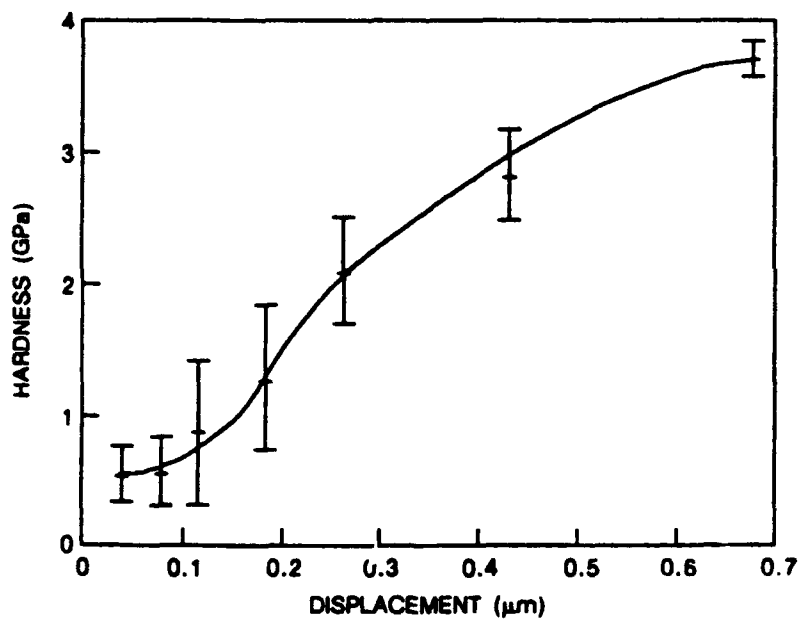
Figure 13. Hardness versus indentation depth as determined by the nanoindentation technique. The hardness of Nb at ~0.4 μm deep indentations is 2.8 GPa.

15
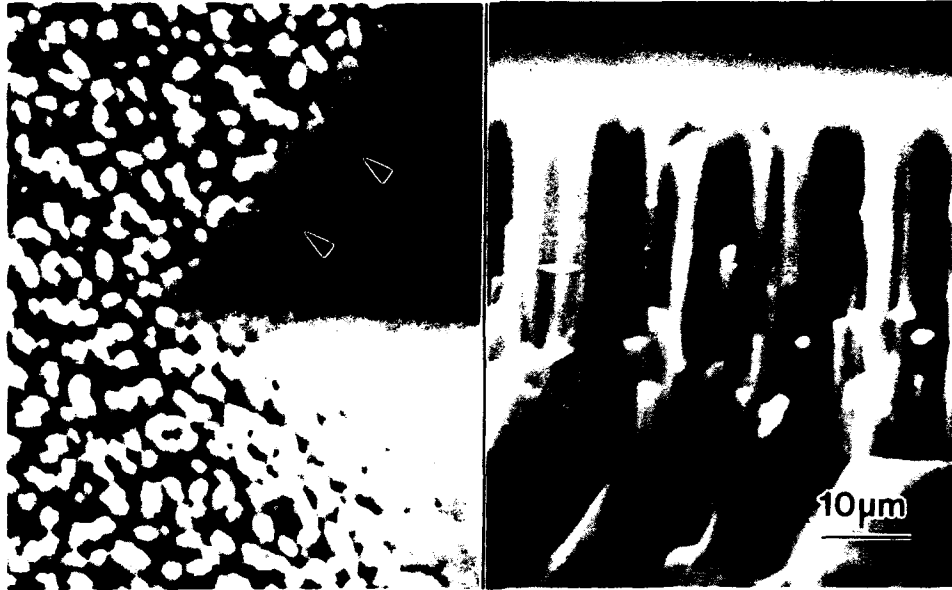
Figure 14. SEM showing the surface finish of as-deposited Nb coating which consists of domed tops ~0.2 μm in diameter (left) . Note the Vickers indentation which made only partial contact with the coating at the edged (arrows). SEM micrograph showing the thickness and columnar structure of as-deposited Nb (right).
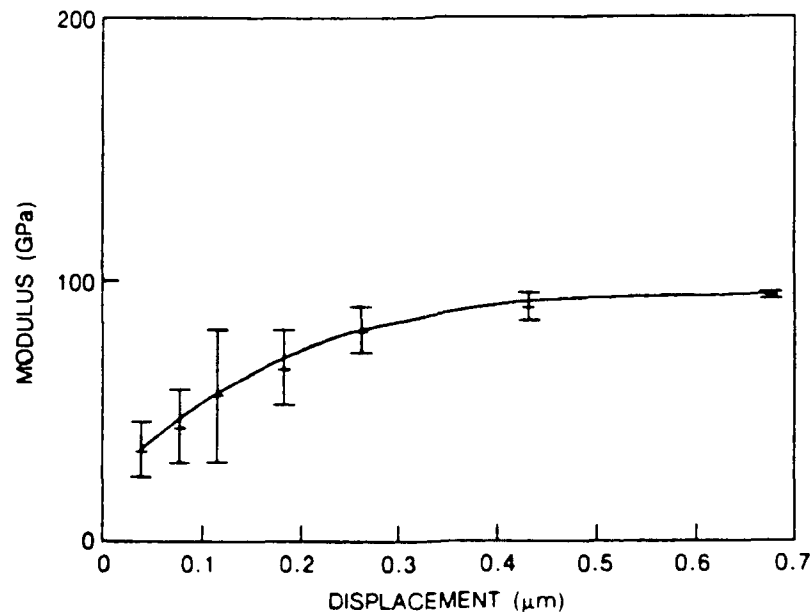
Figure 15. Elastic modulus of Nb versus indentation depth. The modulus at an indentation depth of 0.4 μm is ~88 GPa.

16

3.3.3 Y₂O₃ Coating on Sapphire

3.3.3.1 Coating Fracture Toughness (Kc)

The Nanoindenter® could not be used to determine the coating fracture toughness (K_c) because the maximum load was insufficient to initiate radial cracks. Vickers indentation tests were therefore used to obtain the desired crack morphology. The yttrium oxide coating spalled from alumina substrates at loads as low as 0.147 N (Figure 16a). Approximately 0.02 µm gold was sputtered onto the Y₂O₃ prevent coating spallation and post-indentation slow crack growth. This should not effect the fracture toughness results since the gold film is <2% of the Y₂O₃ coating thickness. Further, the hardness of the Y₂O₃ coating, as measured using the Nanoindenter®, was unaffected by the gold film.

Vickers indentation tests of gold-coated Y₂O₃ did not produce radial cracks at loads less than 0.391 N, while loads >0.538 N caused coating spallation which prevented measurement of radial cracks. Figure 16b shows radial cracks introduced in Y₂O₃ by Vickers indentation at 0.49 N load. Five indentations were made at various loads to obtain average values of radial crack length. The indenter load is plotted versus the radial crack length according to the relation [26]:

$$K_c = 0.019 \, [E/H_v]^{1/2} \, \frac{P}{C^{3/2}} \qquad \text{Equation 7}$$

where E is the elastic modulus of the coating (GPa), H_v is the Vickers hardness (GPa), P is the applied load (N), and C is the radial crack length (m). The results of the indentation tests are plotted in Figure 17. The slope of the curve is $P/C^{3/2}$ = 19.3 MN•m$^{-3/2}$. The hardness and elastic modulus of Y₂O₃ coatings on sapphire were previously found to be 8 GPa and 150 GPa, respectively. The coating fracture toughness is calculated to be K_c = 1.58 MN•m$^{-3/2}$. This value is approximately one-half that of bulk Y₂O₃ [20].

3.3.3.2 Interfacial Fracture Toughness (Kc,i)

The Nanoindenter® was used to assess adhesion of Y₂O₃ coatings on sapphire. Six indentation were performed at depths ranging from 0.3-0.7 µm. However, the coating did not delaminate at indentation depths <0.4 µm. Figure 18a shows a typical load-displacement curve for a 0.67 µm indentation, in which the delamination event is characterized by an abrupt change in slope near zero load. The maximum indenter load, P, is plotted against crack length, C, (Figure 18b). The interfacial fracture toughness is obtained from Equation 3, where k = 0.16, t = 1X10^{-6} m, H_v = 8 GPa, P_0 = 48 mN, P = 75X10^{-9} MN, and C = 3X10^{-6} m, and calculated to be $K_{c,i}$ = 0.15 MN•m$^{-3/2}$. This indicates that the Y₂O₃/Al₂O₃ interface is very weak.

3.3.3.3 Specific Fracture Energy (Γᵢ)

The specific fracture energy of the Y₂O₃ coating on sapphire is calculated using Equation 6, where the geometric crack factor Y = $\pi^{1/2}$ and the elastic modulus of the coating is E = 150 GPa. The specific fracture energy of the Y₂O₃ coating is Γ_i = 4.7 J/m². For $K_{c,i}$ = 0.15 MN•m$^{-3/2}$, the specific fracture energy of the Y₂O₃/Al₂O₃ interface is Γ_i = 0.046 J/m².

17
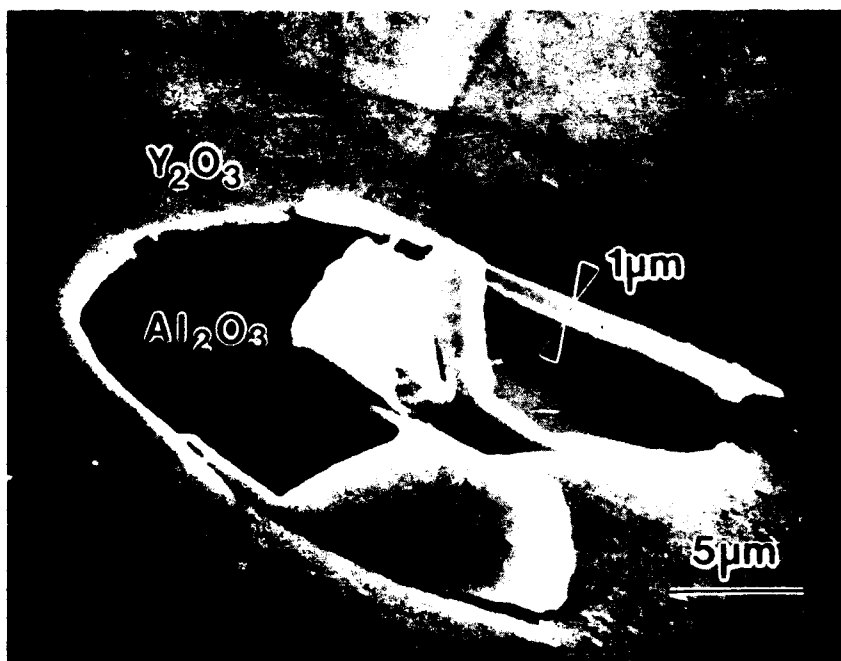
Figure 16a. SEM micrograph of Y_2O_3 coating spalled from (0001) sapphire substrate by a 0.196 N Vickers indentation. The coating thickness is ~1 μm.

Figure 16b. Backscattered SEM micrograph of a Vickers indentation in Y_2O_3 coating at 0.49 N load. Note the radial cracks at the corners of the indentation.

18

Figure 17. Plot of Vickers indentation load versus radial crack length used to determine the fracture toughness of sputtered Y_2O_3 coatings on sapphire.
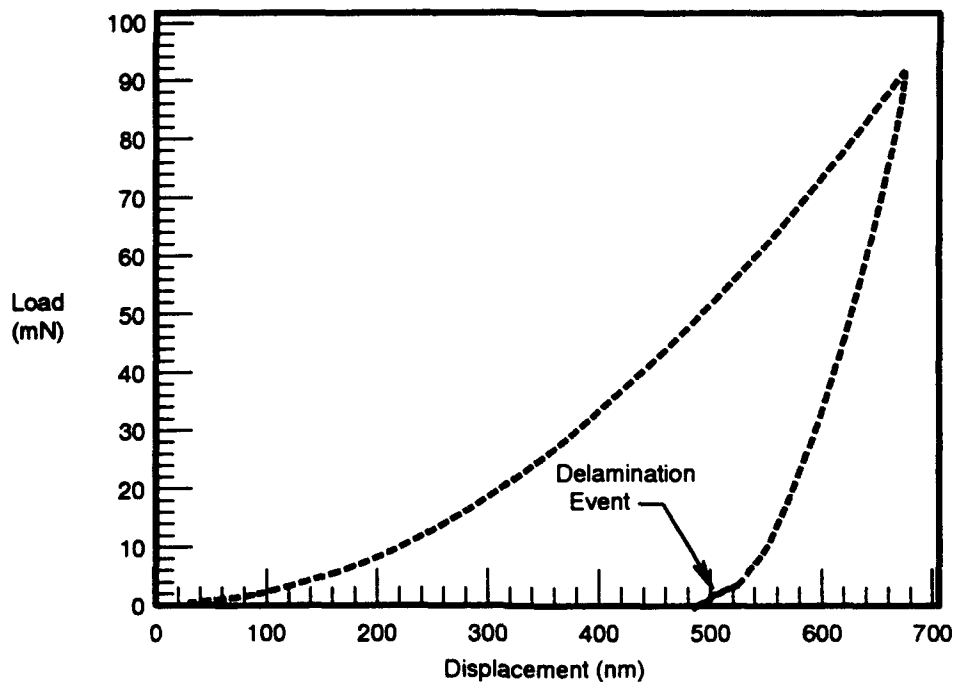
Figure 18a. Typical load-displacement curve produced using the Nanoindenter®. The coating delamination event is characterized by the change in slope near zero load.
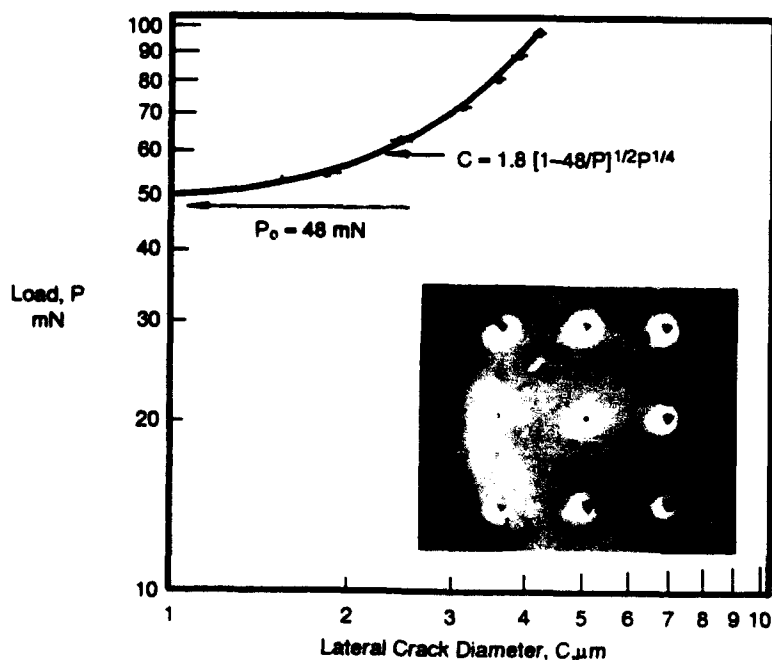
Figure 18b. Plot of Nanoindenter® load versus crack length use to determine Y_2O_3/Al_2O_3 interfacial toughness and light micrograph of several indentations (inset). Bright areas around indentations are indicative of debonding.

20

3.3.4 Y_2O_3 Coating on Polycrystalline Niobium

3.3.4.1 Coating Fracture Toughness (K_c)

The fracture toughness of as-sputtered Y_2O_3 on Nb was determined using Vickers indentation tests at loads ranging from 0.1-1 N. Y_2O_3 coatings on Nb did not exhibit a tendency to spall, unlike that found for Y_2O_3 coatings on Al_2O_3, and were thus not coated with gold. The indenter load, P, is plotted against crack length, $C^{3/2}$, and is shown in Figure 19. The coating fracture toughness is calculated using Equation 7, where $P/C^{3/2} = 2.4$ MN•m$^{-3/2}$, Vickers microhardness of Y_2O_3 is H_v = 8 GPa, coating elastic modulus E = 150 GPa, and found to be $K_c = 0.20$ MN•m$^{-3/2}$. This value is approximately one-tenth of that found for Y_2O_3-coated Al_2O_3. The differences in fracture toughness is likely due to extensive deformation of the niobium substrate (Figure 20) [10].

3.3.4.2 Interfacial Fracture Toughness $(K_{c,i})$

As-deposited Y_2O_3 coatings were not observed to debond from the Nb substrate at loads up to 0.078 N using the Nanoindenter® and 9.8 N using the Vickers indenter. However, lateral cracks formed in the Y_2O_3 coating at loads >0.078 N (Figures 20a and 20b). In contrast, as-sputtered Y_2O_3 coatings (with no gold overcoat) were observed to debond from Al_2O_3 at loads as low as 0.147 N. This result implies that the fracture toughness of the Y_2O_3/Nb interface is greater than the Y_2O_3/Al_2O_3 interface, but is not consistent with previous results where the Y_2O_3/Nb interface was found to be weaker than Al_2O_3/Nb [6] or Y_2O_3/Al_2O_3 [7].

Examination of the indentations showed that the Y_2O_3 coating did not buckle or spall at loads up to 9.8 N (Figure 20b). Instead, the cracked coating appears to be well-bonded to the Nb substrate. A plot of indenter load versus lateral crack diameter (Figure 21) does not reveal an asymptotic load at which lateral cracks vanish (Figure 18b). This suggests that cracks caused by indentation tests propagate towards the surface rather than initiate delamination at the interface.

3.3.4.3 Specific Fracture Energy (Γ_i)

The specific fracture energy of as-sputtered Y_2O_3 coating on Nb is calculated using Equation 6, where $K_c = 0.2$ MN•m$^{-3/2}$, $Y = \pi^{1/2}$, and E = 150 GPa. For The specific fracture energy of the Y_2O_3 coating is $\Gamma_i = 0.074$ J/m^2.
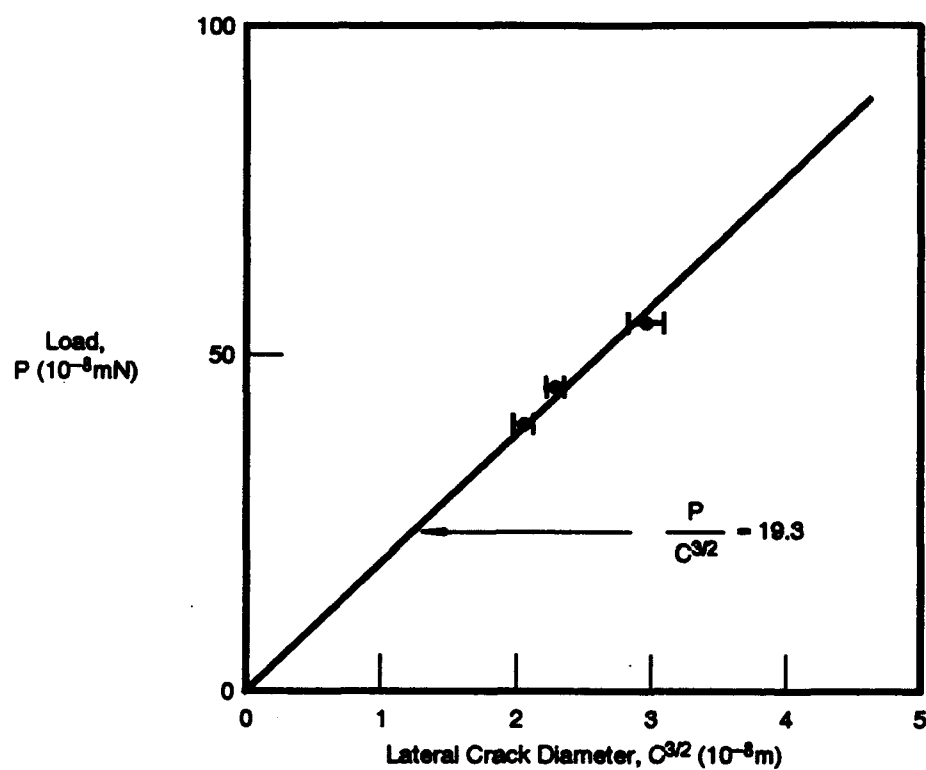
21
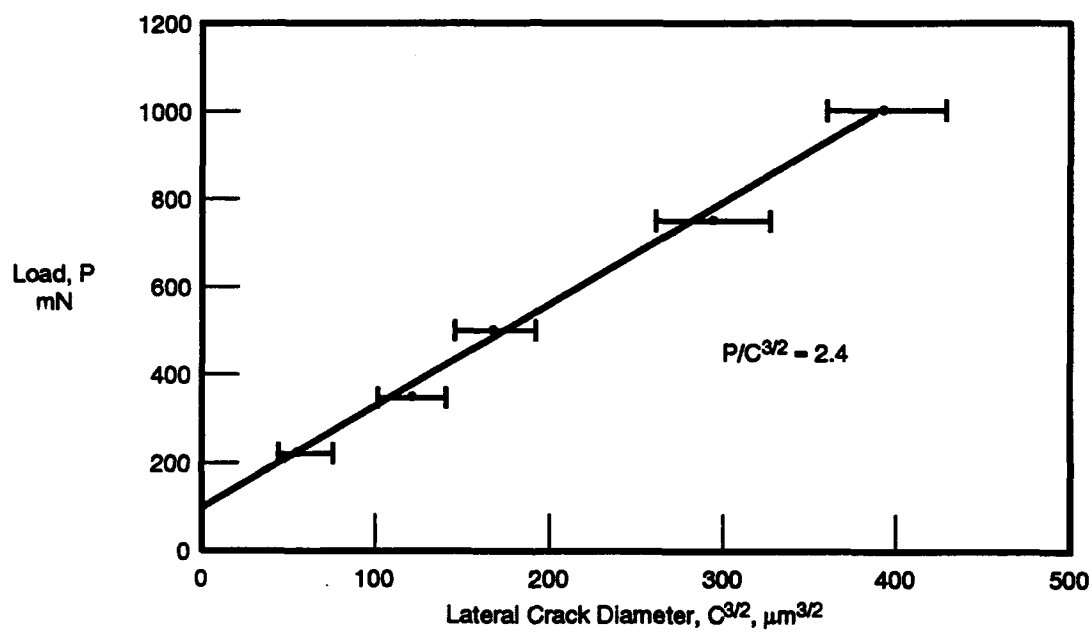
Figure 19. Plot of Vickers indentation load versus radial crack length used to determine the fracture toughness of sputtered Y_2O_3 coatings on niobium.
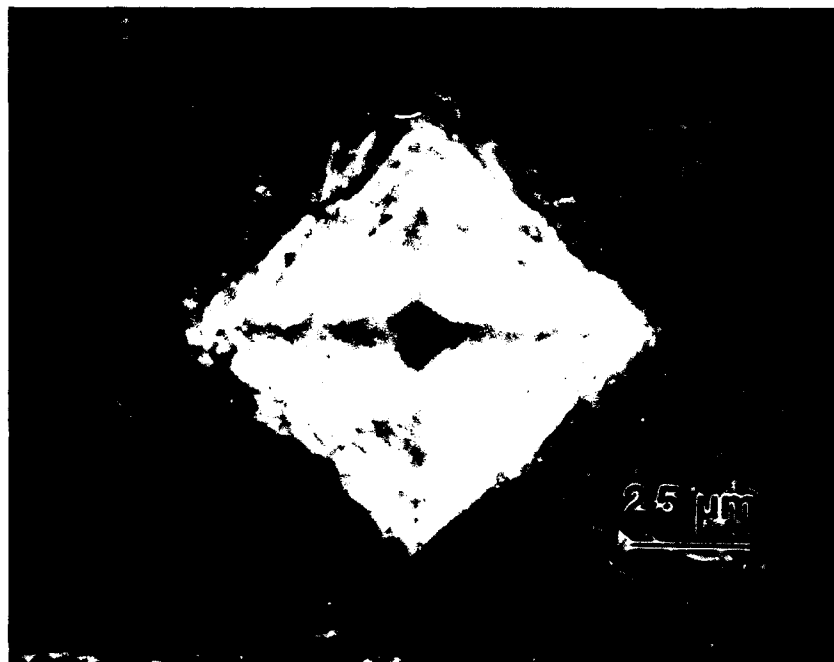
Figure 20a. Dark field optical micrograph of a 9.8 N indentation for Y_2O_3 coated niobium. Note the numerous cracks emanating from the indentation.
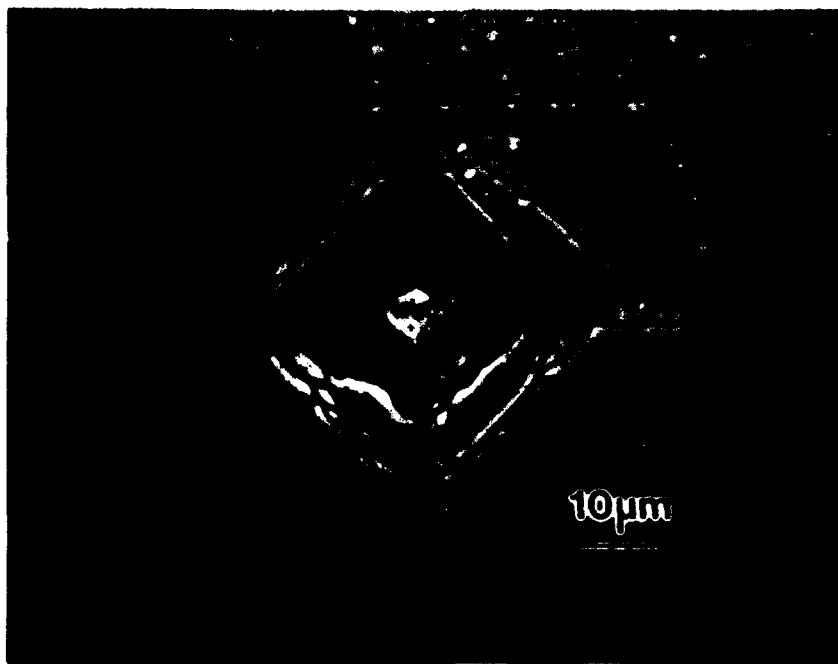
Figure 20b. Backscattered SEM micrograph of a 0.98 N indentation for Y_2O_3 coated niobium. Note the radial and lateral cracks, as well as adherence of the coating to the niobium substrate.
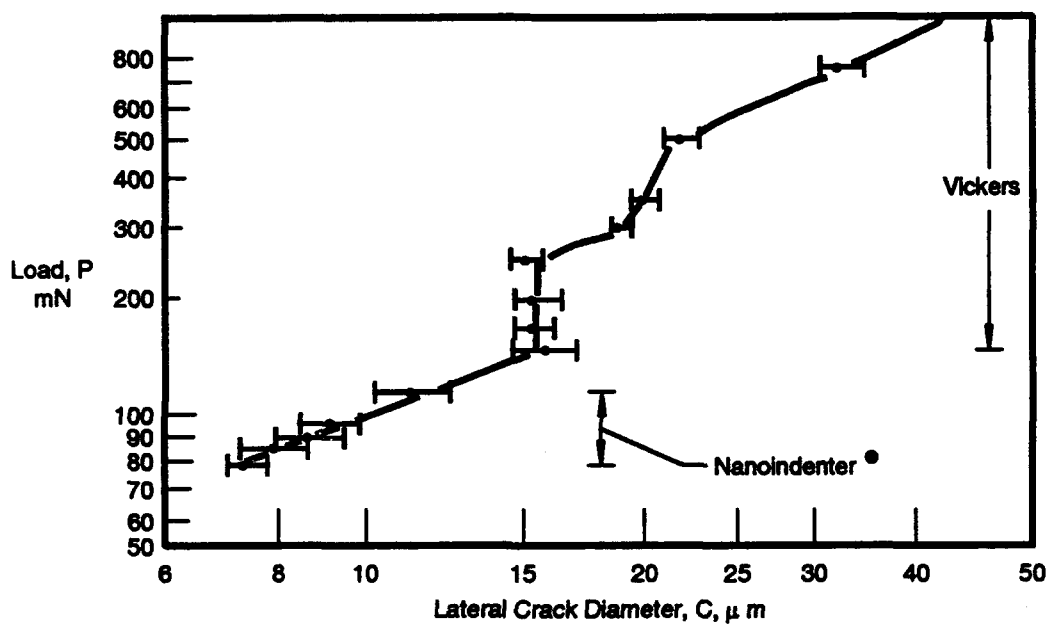
Figure 21. Plot showing the variation load versus lateral crack diameter for both Vickers (P > 120 mN) and Nanoindenter® (P < ~125 mN) tests.

3.3.5 Niobium Coating on Single Crystal Y_2O_3

3.3.5.1 Coating Fracture Toughness (K_c)

The fracture toughness of as-sputtered Nb on Y_2O_3 was determined using Vickers indentation tests at loads ranging from 2-10 N. Niobium coatings did not exhibit a tendency to crack or spall at 2 N, while radial cracks were produced at 3, 5, and 10 N (Figure 22). A plot of the indenter load, P, versus crack length, $C^{3/2}$, as measured from the Nb coating and transparent backside of the Y_2O_3 wafer is shown in Figure 23. The coating fracture toughness is calculated using Equation 7, where the average of the two curves is $P/C^{3/2} = 11.5$ MN•m$^{-3/2}$, Vickers microhardness of Y_2O_3 is $H_v = 2.8$ GPa, coating elastic modulus $E = 88$ GPa, and found to be $K_c = 1.22$ MN•m$^{-3/2}$. This value is much lower than the room temperature fracture toughness of bulk Nb [27]. The difference in fracture toughness most likely due to coating thickness, columnar microstructure, and the presence of a residual stress in as-deposited Nb.

3.3.5.2 Interfacial Fracture Toughness ($K_{c,i}$)

As-deposited Nb coatings were observed to debond from the Y_2O_3 substrate at loads as low as 0.25 N using the Vickers indenter. The delamination event was observed from the backside of the transparent Y_2O_3 substrate through the formation of interference rings (Figure 24). A plot of indenter load, P, versus lateral crack length, C, is shown in Figure 25. The interfacial fracture toughness is obtained from Equation 3, where $k = 0.16$, $t = 4 \times 10^{-6}$ m, $H_v = 2.8$ GPa, $P_o = 135$ mN, $P = 1500$ mN, and $C = 20 \times 10^{-6}$ m, and calculated to be $K_{c,i} = 0.18$ MN•m$^{-3/2}$. This value is two orders of magnitude lower than that measured in uniaxial tension tests of niobium reinforced TiAl laminates with Y_2O_3 interfacial coating [6].

3.3.5.3 Specific Fracture Energy (Γ_i)

The specific fracture energy of as-sputtered Nb on Y_2O_3 is calculated using Equation 6, where $K_c = 1.22$ MN•m$^{-3/2}$, $Y = \pi^{1/2}$, and E(Nb) = 88 GPa. The specific fracture energy of the coating is $\Gamma_i = 4.78$ J/m^2. For $K_{c,i} = 0.18$ MN•m$^{-3/2}$, the specific fracture energy of the Nb/Y_2O_3 interface is $\Gamma_i = 0.104$ J/m^2. The coating fracture toughness, interfacial fracture toughness, and specific fracture energy results presented in Sections 3.3-3.5 are summarized in Table 1.

Figure 22. SEM micrographs of indentations produced by loads of 2 N (left) and 10 N (right) showing radial cracks.
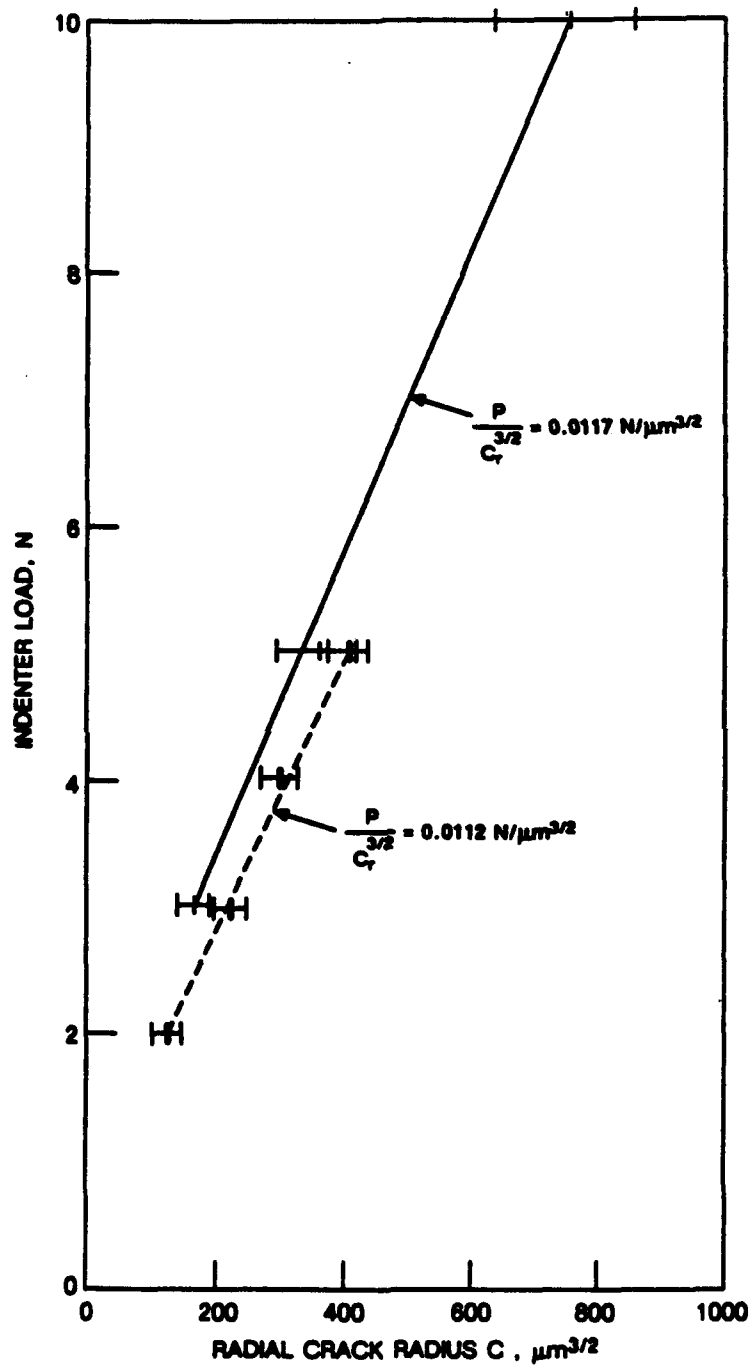
Figure 23. Plots of Vickers indenter load versus radial crack length for the Nb coating. Crack lengths were measured from the top (solid line - Figure 22) and from the back through the transparent Y_2O_3 wafer, and show good correlation.

27
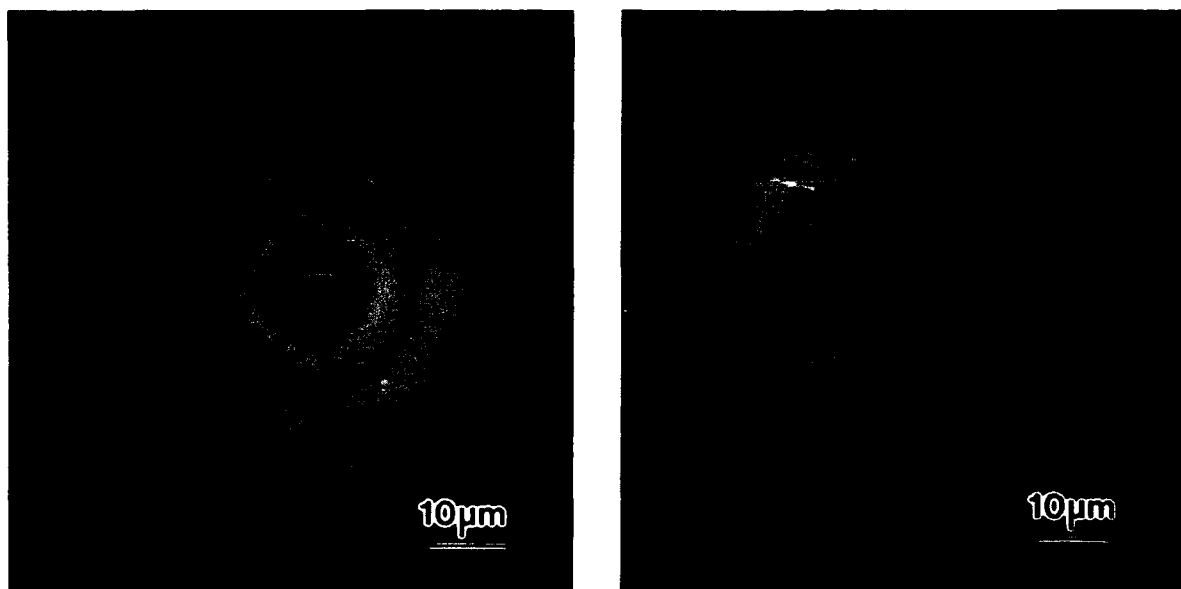
Figure 24. Light micrographs showing debonding of the Nb coating at loads of 1.5 N (left) and 3 N (right), as viewed from the transparent backside of the Y_2O_3 wafer. Radial cracks produced by the 3 N load are apparent.

$$C = 3.39[1-135/P]^{1/2}P^{1/4}$$
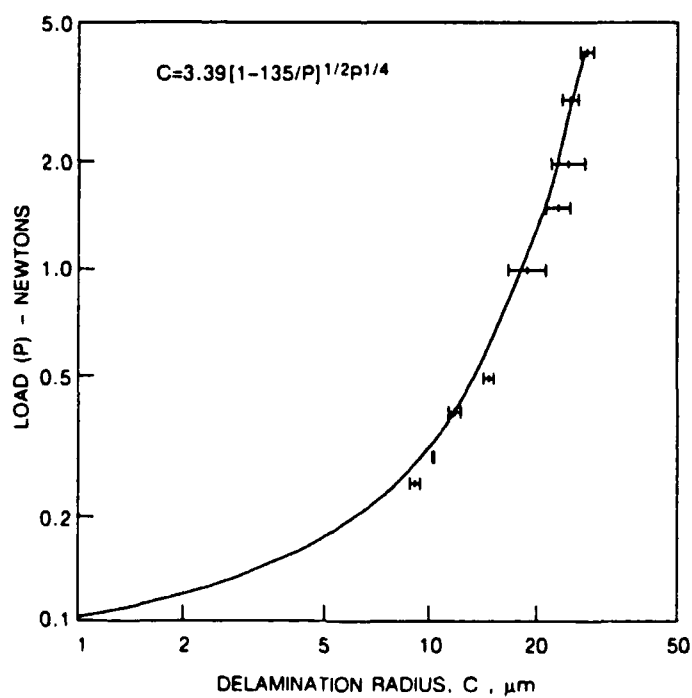
Figure 25. Plot of load versus crack length use to determine Nb/Y_2O_3 interfacial fracture toughness.

TABLE 1 SUMMARY OF COATING FRACTURE DATA

COATING/ SUBSTRATE	TEST METHOD	K_c $MN \cdot m^{-3/2}$	$K_{c,i}$ $MN \cdot m^{-3/2}$	Γ_i J/m^2
Y_2O_3/Al_2O_3	Indentation	1.58	-	4.70
Y_2O_3/Al_2O_3 Interface	Indentation	-	0.15	0.046
Y_2O_3/Al_2O_3 Interface [7]	Cone Crack	-	3.65*	25
Y_2O_3/Nb	Indentation	0.20	-	0.074
Y_2O_3/Nb Interface	Indentation	-	-	-
Y_2O_3/Nb Interface [6]	Tensile	-	3.65*	25
Nb/Y_2O_3	Indentation	1.22	-	4.78
Nb/Y_2O_3 Interface	Indentation	-	0.180	0.104
Y_2O_3/Nb Interface [6]	Tensile	-	3.65*	25
Bulk Y_2O_3 [20]	Indentation	2.85	-	15

* $K_{c,i}$ obtained from Γ_i using Equation. 6.

3.4 DISCUSSION

3.4.1 Characterization of As-Deposited Y_2O_3

Evaluation of reactively sputtered Y_2O_3 coatings shows they are stoichiometric and contain low levels of impurities. The coating microstructure is typical of that found in thin vapor deposited coatings examined through-thickness. A feature unique to vapor deposition is the range of microstructures, and hence physical and mechanical properties that can be obtained in as-deposited coatings. An experimentally determined model of the structure of metal and ceramic coatings deposited by direct current (DC) and radio frequency (RF) sputtering as a function of working gas pressure and homologous temperature, T/T_M, shows a trend from high aspect ratio columnar (Zone 1) to equiaxed (Zone 3) grains [18]. The Zone 1 microstructure consists of tapered crystallites with a fibrous internal structure, continuous voids at grain boundaries, and domed tops whose diameter increases with increasing substrate temperature. The formation of an intergranular network of voids is further enhanced by shadowing due to substrate surface roughness or preferential growth of crystallites and low adatom surface mobility. The mechanism by which grain boundaries coalesce to produce more dense columnar microstructures is attributed to increased adatom mobility caused by higher T/T_M as well as increased desorption of inert gas atoms.

Coating microstructures produced at low T/T_M are found in most vapor deposited coatings. Figure 4 shows that sputtered Y_2O_3 coatings consist of columnar grains whose length extends through the entire coating thickness. These microstructures may be the least desirable since pipe diffusion can occur easily along porous grain boundaries and result in increased interaction with the substrate during hot pressing. In addition, sputtered coatings often contain a large amount of interfacial area which should affect the thermochemical stability and mechanical properties of the matrix/reinforcement interface [28-32].

The microstructure normally found in coatings deposited at low T/T_M may contain 50-400 grains/μm^2, resulting in 15-25% grain boundary area [28,29,31,32] compared to 0.05% for bulk polycrystalline materials [28]. Coatings may contain additional interfacial area in the form of twins and stacking faults [30]. However, diffusion bonding Nb- reinforced TiAl results in a coating with better defined columnar grains, minimal reaction with the matrix or reinforcement, and composites with improved interfacial debonding and fracture toughness. This is due to the intrinsic thermochemical stability of Y_2O_3 in contact with Nb and TiAl, and thermodynamic preference to reduce interfacial area at the temperature and time used to bond the laminates together.

3.4.2 Nb/Al$_2$O$_3$ and Ti/Al$_2$O$_3$ Interfaces

Uniaxial tension tests of precracked TiAl/Nb laminates fractured *in situ* in the scanning electron microscope showed debonding occurs along the Nb/Y_2O_3 interface, which permits plastic deformation of the ductile phase over long lengths [6]. The yttria coating results in a 200% increase in work of fracture compared to Al_2O_3-coated niobium. The Nb/Y_2O_3 system has not been previously studied. However, both the Nb/Al_2O_3 [9,33,34] and Ti/Al_2O_3 [35-37] interfaces are well-characterized, and represent examples of non-reactive and reactive metal/ceramic systems, respectively. Understanding each provides a basis for determining the cause of a high work of rupture in Y_2O_3-coated Nb-reinforced TiAl.

The Nb/Al_2O_3 interface has been characterized by direct imaging using high resolution TEM [9]. Polished single crystals of niobium and Al_2O_3 were diffusion bonded at 1700°C for two hours in high vacuum ($\sim 10^{-3}$ Pa) and 10 MPa load. The couples were bonded in a (110)Nb ‖ (0001)Al$_2$O$_3$ and [001]Nb ‖ [2110]Al$_2$O$_3$ orientation relationship. Samples for high resolution TEM were obtained from the bulk couple with foil planes normal to [001]Nb and [110]Nb. High resolution TEM of the interface did not reveal the presence of a reaction layer. This is in contrast to other studies, where Nb oxides [38] or impurities present in polycrystalline Al_2O_3 or Nb segregated or catalyzed reactions at the interface during hot pressing [39]. Non-equilibrium phases may form at the interface due to diffusion of impurities to accommodate misfit strain. While Al_2O_3 is dissolved by Nb at $\sim$1700°C, no metallic Al was found in single crystal couples bonded at 1700°C for 2 hours [9]. It is possible that a small amount of Al_2O_3 was dissolved and subsequently precipitated at the interface upon cooling. This should form defects at the interface due to misfit strains developed at the interface, but none were observed. These results indicate that chemical interaction between high purity single crystal Nb and Al_2O_3 is minimal during diffusion bonding.

Another study examined the Nb/Al_2O_3 interface by internally oxidizing an Nb-3 at.% Al alloy at 1450°C [33]. No interfacial compounds were detected by high resolution TEM, and the interface was observed to be atomically flat. The outer layer of Al_2O_3 was suggested to consist of a monolayer of oxygen atoms. The Nb/Al_2O_3 interface has also been examined by XPS and Auger electron spectroscopy (AES). Several monolayers of Nb were evaporated *in situ* onto (0001) sapphire substrates heated to 1000°C [34]. High resolution spectra of Nb (3d), O (1s), and Al (2p) versus Nb coating thickness indicate the Nb donates electrons to surface oxygen atoms to form Nb-O bonds. Thus, a chemical reaction occurs between Nb and Al_2O_3, but it is limited to approximately one monolayer.

The former TEM study [9] did not discuss the presence of an oxide layer on polished Nb (1-2 nm thick) or physisorbed or chemisorbed species on Nb or sapphire. Physisorbed species such as H_2O will mostly desorb upon heating, while monolayer coverage of hydrocarbon should innocuously diffuse into an infinite sink of Nb.

30

At temperatures typical of diffusion bonding, the oxide layer on Nb will likely be reduced by bulk Nb, which has ~0.1 wt.% solubility for oxygen at 25°C. Remarkably, efforts to determine the nature of the Nb/Al$_2$O$_3$ interface exhibit similar results while utilizing samples prepared by greatly different methods and with different levels of surface contamination [9,33,34].

The Ti/Al$_2$O$_3$ system, in contrast, is highly reactive, resulting in considerable degradation of the interface [35-37]. Single crystal Al$_2$O$_3$ fibers ~300 μm in diameter were hot pressed between commercially pure α-titanium sheets ~400 μm thick at 815°C for 2 hours and 110 MPa [35], then vacuum annealed at 600-1000°C for times sufficient to produce measurable reaction zones and determine rate constants. The resulting reactions were characterized by XRD and electron microprobe. The reaction product after exposure to 1000°C for 100 hours was ~40 μm thick and found to consist of Ti$_3$Al and TiAl. Microhardness measurements were used to determine the extent of oxygen diffusion into the surrounding matrix.

Reactions between thin films of titanium on bulk alumina and on alumina-containing substrates have been extensively studied [36,37]. Single crystal alumina substrates maintained at 25°C and 1000°C were coated with titanium by evaporation, then examined by XPS [36]. At 25°C, several monolayers of titanium were found to reduce the Al$_2$O$_3$ surface and produce Ti-O bonds. In contrast, coatings deposited on substrates held at 1000°C produced both Ti-O and Ti-Al bonds. In the former, titanium bonds to a monolayer of oxygen atoms on the oxide surface, while in the latter reduction of the oxide is extensive and enables the formation of titanium-aluminum compounds.

Interfacial reactions between titanium and amorphous cordierite-based (2MgO•2Al$_2$O$_3$•5SiO$_2$) ceramic films 200 nm thick on single crystal silicon were characterized by XPS [37]. Si-O bonds were found to dissociate at room temperature with sub-monolayer coverages of titanium. Additional coverage by titanium began to reduce Al-O bonds. Vacuum annealing results in increased reaction kinetics between Ti and SiO$_2$ and Al$_2$O$_3$. However, titanium was not observed to reduce the Mg-O bond up to 800°C. Magnesium oxide-based compounds may be debond coatings worth investigating in titanium matrix composites.

It is apparent that a reactive system such as Ti/Al$_2$O$_3$ produces intermetallic reaction products that thicken with extended exposure to elevated temperature, thereby forming a more complicated interface. If the fracture energy of the reaction products is sufficient to discourage extensive debonding, then the toughness of the composite is reduced. For example, uncoated Nb plates diffusion bonded to TiAl reacted to form σ and T$_2$ phases 4-6 μm thick [6]. Tensile testing showed debonding occurred in the σ phase, which had a measured fracture energy of $\Gamma_i = 45$ J/m^2. This is sufficient to retard debonding and reduce the work of rupture by 66%. These results suggest that there may be similarity between the Nb/Al$_2$O$_3$ and Nb/Y$_2$O$_3$ systems [6,9,33,34]. The Nb/Y$_2$O$_3$ interface may be atomically sharp, similar to that found in Nb/Al$_2$O$_3$ [9]. This, coupled with a lower Y$_2$O$_3$ fracture energy, may cause the improved debonding and higher fracture toughness observed experimentally [6].

3.4.3 *Relationships to Debonding*

The success of a particular material as a debond coating will depend on a combination of several factors including coating thickness, surface and bulk impurities, local stress state, coating mechanical properties, bond strength between the coating and reinforcement or matrix, thermodynamic stability, and microstructure.

31

Coating thickness has not yet been quantified, but it is reasonable to assume that there are optimum thicknesses that may be defined by other variables in the composite system such as reinforcement size or diffusivity. Impurities in the bulk can accumulate at the interface [9], and is expected to be detrimental in most cases. The effect of surface impurities remains uncertain, but does not appear to cause difficulties in the case of Nb/Al_2O_3 [9,33,34]. However, the use of high surface area reinforcements such as multifilament fiber tows, whiskers, or particulates may require preferential treatment to avoid the introduction of large amounts of physisorbed species. Interstitials or minor alloying elements may locally stabilize unwanted phases or precipitate new phases, thereby deleteriously affecting matrix properties.

Debonding has been observed in many fiber/coating/matrix systems including $Nb/Y_2O_3/TiAl$ [6], $Al_2O_3/Mo/Al_2O_3$ [7], $Al_2O_3/porousZrO_2/Al_2O_3$ [8], SiC/C/AS [2], SiC/BN/SiC [40], and $W/Al_2O_3/TiTaAl_2$ [41]. The coefficient of thermal expansion (CTE) should be an important consideration in selecting debond coatings. In particular, the difference in relative CTE between the fiber/coating/matrix should be small ($\Delta\alpha = 1$-3 ppm/$^\circ$C). In some case the interface is in compression, while in others the interface is in a small amount of tension. There seems to be no simple rule for determining which case is most desirable, other than that the magnitude of the tensile stress can not be high.

Oxide coatings perform well in ductile phase reinforced brittle matrix systems because they fracture at low applied stress, enabling plastic deformation of the toughening phase [6]. The specific fracture energy (Γ_i) of oxide coatings is small, typically on the order of 25 J/m^2. The improved debonding obtained with Y_2O_3 versus Al_2O_3 coatings suggests the fracture energy of the former is lower. In addition, pores in the coating will affect coating fracture toughness and debonding behavior of composites [8]. Thus, prior knowledge of thin film fracture toughness, its dependence upon porosity, and control of porosity in the application of coatings can be useful in guiding future coating selection. Successful debond coatings must also be thermally stable and substantially non-reactive with respect to both the matrix and reinforcing phase. The Gibb's free energy of formation of α-Al_2O_3 and Y_2O_3 is -378.2 kcal/mole and -434.2 kcal/mole, respectively [42]. Yttria should, therefore, be more difficult to reduce by Nb and TiAl at typical diffusion bonding temperatures and times, thus retaining a sharp interface. For similar reasons, Y_2O_3 also serves as a protective coating between the niobium reinforcement and TiAl matrix.

The microstructure of sputtered Y_2O_3 was found consist of tapered crystallites extending through the thickness of the coating, perhaps resulting in pipe diffusion and increased reaction with the matrix or reinforcement. Such interaction should affect debonding by altering the interfacial chemistry. While this may occur in some systems, it has not yet been observed in the composite system under investigation. Further, sputtered Y_2O_3 coatings evaluated in Nb reinforced TiAl matrices remain columnar after hot-pressing (Figure 8). Conversely, Mo and ZrO_2 coatings in Al_2O_3/Al_2O_3 laminate specimens become equiaxed after hot-pressing [7,8]. This will also likely affect the mechanical properties of the coating, interface, or crack path. For example, thermal exposure during composite processing or coating microstructure may determine the location of debonding - i.e. within the coating, at the coating/fiber interface, or at the coating/matrix interface - whichever has the lowest specific fracture energy. No rationale has yet been developed to guide selection of the preferred debond site.

32

3.4.4 Analysis of Indentation-Derived Coating Fracture Results

3.4.4.1 Y_2O_3 Coatings on Al_2O_3

The specific fracture energy of interfaces modified with coatings was measured by Hertzian cone cracking experiments using a model single crystal Al_2O_3/Al_2O_3 composite system [7,8]. The coatings evaluated include molybdenum, yttria stabilized ZrO_2 (tetragonal structure), TiAl, m-ZrO_2 (m = monoclinic), and Y_2O_3. All coatings were deposited by sputtering, while the latter two were also applied using sol-gels, at a nominal coating thickness of 1 μm. Single ply laminate specimens were fabricated by diffusion bonding coated Al_2O_3 wafers in vacuum at 1000-1400°C under a pressure of 1 MPa. Cracks are introduced into the Al_2O_3 laminate by applying a point load using a 12.5 mm WC ball. The Hertzian crack reaches the interface and either passes through the coating or is deflected by fracture along the interfacial coating, resulting in improved toughness. Coatings which exhibited this behavior low specific fracture energies and include molybdenum (Γ_i = 3-5 J/m^2) and ~50% porous monoclinic ZrO_2 (Γ_i = 4 J/m^2). Conversely, neither sputtered or sol-gel Y_2O_3 coatings were suitable because they reacted partially with the Al_2O_3 substrate to form YAG at the interface, resulting in a high specific fracture energy (Γ_i = 25 J/m^2).

The fracture toughness and specific fracture energy of the Al_2O_3/Y_2O_3 interface measured in the present study by indentation tests is 0.15 MN•m$^{-3/2}$ and 0.046 J/m^2, respectively (Table 1). Both values are lower than expected. The difference is attributed to the evaluation of as-deposited coatings which did not react with the Al_2O_3 substrate to form YAG due to the low substrate temperature during sputtering, and the columnar microstructure. The low specific fracture energy of the Y_2O_3/Al_2O_3 interface (Γ_i = 0.046 J/m^2) is indicative of weak bonding between as-deposited Y_2O_3 coating and the alumina substrate.

3.4.4.2 Y_2O_3 Coatings on Niobium

The interfacial debonding characteristics of sputtered Al_2O_3 and Y_2O_3 interface in a TiAl/Nb composite showed that the preferred debond coating is Y_2O_3. The specific fracture energy of the Y_2O_3/Nb interface is ~25 J/m^2, and is sufficiently low in this composite system to promote extensive plastic deformation of the ductile phase over a large volume. Debonding, coupled with a ductile phase which easily work hardens, results in a composite with high toughness. Indentation test data (Table 1) shows that the calculated fracture toughness and fracture energy of as-deposited Y_2O_3 on Nb reflects failure of the Y_2O_3 coating and deformation of the Nb substrate as a single unit. Thus, measurements of $K_{c,i}$ could not be made because coating failure is not independent of the substrate.

3.4.4.3 Niobium Coatings on Y_2O_3

Indentation tests to determine the fracture toughness and fracture energy of the Nb-Y_2O_3 interface could only be assessed if the test specimen geometry were reversed - i.e. sputtered Nb coating on single crystal Y_2O_3. The interfacial fracture toughness is an order of magnitude lower than that found in uniaxial tensile tests of Nb-reinforced TiAl laminates [6]. As a result, the specific fracture energy of the Nb-Y_2O_3 interface as determined by indentation tests did not correlated to that found in tensile tests using diffusion bonded Nb-TiAl laminates.

33

3.4.4.4 Bulk Y_2O_3

The fracture toughness of bulk Y_2O_3 reportedly varies from 2.3-3.4 MN•m$^{-3/2}$ [20], resulting in Γ_i = 9.95-21.7 J/m^2. Conversely, the measured indentation-derived fracture toughness of as-deposited Y_2O_3 coating on sapphire is 1.58 MN•m$^{-3/2}$, resulting in Γ_i = 4.7 J/m^2 (Table 1). The intrinsic fracture toughness of as-deposited Y_2O_3 coating is about half that of bulk Y_2O_3. The difference is due to the evaluation of dissimilar microstructures - i.e. sub-micron columnar Y_2O_3 grains for vapor deposited Y_2O_3 versus equiaxed grains in bulk Y_2O_3. Regardless, reasonable correlation to bulk properties can be achieved via Vickers indentation testing provided the coating is deposited onto a hard substrate.

3.4.5 Factors Affecting Fracture Toughness Results

There are several factors which can affect the response of the coating to indentation tests. These include thickness, residual stress, bond strength, microstructure, and elastic modulus. The hardness, elastic modulus, and fracture properties of micron-thick coatings can be evaluated using the Nanoindenter®. However, the loads required to initiate radial cracks at the corners of the indentation may exceed that load range of this instrument, as was the case for as-deposited Y_2O_3 coatings on sapphire (Section 3.3.1). Thus, it is reasonable to assume that there is minimum thickness that is required for testing. The present study indicates that coatings ~1 μm thick are suitable for testing. This is also a useful coating thickness for applications requiring debond coatings on monofilament or multifilament fibers.

Residual tensile or compressive stresses are commonly found in as-deposited sputtered coatings, and may be caused by the sputtering equipment geometry or deposition conditions. These include target-to-substrate distance, working gas pressure, reactive gas partial pressure, substrate bias, or coating/substrate thermal expansion mismatch [43]. The residual stress in as-deposited films can affect indentation tests. For example, coatings with residual compressive stress may inhibit radial cracking and result in higher K_c. Conversely, $K_{c,i}$ may be reduced due to a propensity for the coating to buckle. Residual stress may not be a significant factor in the present study because the fracture toughness of as-deposited Y_2O_3 is in reasonable agreement with bulk Y_2O_3.

The bond between the coating and substrate must have sufficient strength to allow the coating to be probed at loads required to produce the desired coating fracture morphology. This will be most greatly influenced by post-deposition processing of the coating/substrate system such as hot-pressing. Laminate samples previously evaluated were hot-pressed at temperatures ranging from 1066-1450°C [6,7], which may result in the formation of interfacial compounds. For example, Y_2O_3 coatings on sapphire reacted to form a layer of YAG at the interface [7]. The interfacial fracture toughness of this system will be higher than as-sputtered Y_2O_3 on sapphire.

The microstructure of as-deposited Y_2O_3 coatings consists of tapered crystallites extending through the thickness of the coating and is produced by low adatom mobility due to low homologous temperature and preferential growth of crystallites [18]. This microstructure will affect the results of indentation tests because the load is applied parallel to columnar grains. The difference in fracture toughness between as-deposited Y_2O_3 and bulk Y_2O_3 is attributed to evaluation of dissimilar microstructures - i.e. sub-micron columnar Y_2O_3 grains for vapor deposited Y_2O_3 versus 1-10 μm diameter equiaxed grains in bulk Y_2O_3 [20].

Calculations to determine Γ_i utilize the elastic modulus of Y_2O_3 as determined by the Nanoindenter®. This value, 150 GPa, agrees with that previously determined for bulk Y_2O_3 [23]. The elastic modulus is determined by a uniaxial tension test where stress is linearly proportional to strain. However, this condition is not satisfied by indentation tests and for thin coatings attached to a substrate. In addition, the indenter does not load the coating in uniaxial tension, the condition under which Young's modulus is obtained. The elastic modulus is also a directional property [44], so the modulus of free-standing films deposited at low T/T_M will be anisotropic and vary depending upon orientation to the columnar grains. These factors cause uncertainty in the application of bulk elastic properties to the determination of K_c and Γ_i.

The modulus of elasticity is also a function of the type of chemical bonding in a crystal - i.e. ionic, covalent, metallic [44]. A thin free-standing film should therefore exhibit bulk elastic properties provided ratio of surface atoms to interior atoms is low. A 1 μm thick film contains ~3000 atoms through-thickness, which should be sufficient to satisfy this criterion and exhibit bulk or near-bulk properties. A similar argument may also apply to other properties of coatings 1-2 μm thick.

The elastic modulus of supported and unsupported thin films has been determined by different techniques, and varies from 0.1 to 0.9 of bulk properties [45-47]. These results indicate that elastic properties are dependent upon many variables related to mechanical test conditions, coating deposition method, and perhaps even sputter-deposition parameters. The specific fracture energy of as-deposited Y_2O_3 on Al_2O_3 was found to be 4.7 J/m^2 (Table 1). Calculation of this parameter using 75 GPa and 15 GPa (instead of 150 GPa) yields specific fracture toughnesses of 9.4 J/m^2 and 46.9 J/m^2, respectively. The specific fracture energy of as-deposited Y_2O_3 approaches that of bulk Y_2O_3 for E = 75 GPa. However, there are distinct differences in microstructure as previously noted. Thus, values of K_c and $K_{c,i}$ calculated for as-deposited Y_2O_3 on sapphire using Young's modulus for bulk Y_2O_3 may indeed be indicative of actual coating fracture properties and interfacial debonding behavior.

The calculated values for fracture toughness and fracture energy derived by indentation tests must be used carefully since numerous test-related factors can affect the results [13,14,19,48]. Many of the factors related to the coating, its deposition, or indentation test technique are difficult, if not impossible to control. However, the results presented in Table 1 show that indentation and tests can be used to determine coating fracture properties (K_c), with reasonable correlation to bulk properties. However, the interfacial fracture toughness ($K_{c,i}$) and specific fracture energy (Γ_i) could not be correlated to results obtained from laminates evaluated by tensile [6] or cone crack [7,8] tests. This is attributed to differences in test methods and sample preparation. For example, tensile tests to determine Γ_i in Nb-reinforced TiAl measures decohesion along two interfaces, while indentation tests measure only one interface. Hertzian cone crack tests are an elastic indentation test method, while Nanoindenter® and Vickers indentation tests are plastic indentation test methods. Samples prepared by RF sputtering were not exposed to the same thermal history as diffusion bonded samples.

3.5 CONCLUSION

The fracture toughness, interfacial fracture toughness, and specific fracture energy for as-sputtered Y_2O_3 coatings on sapphire and commercial purity polycrystalline Nb substrates, and Nb-coated Y_2O_3 was determined via micro- and nanoindentation techniques. The results were compared to fracture toughness studies of Al_2O_3/Al_2O_3 [7,8] and Nb-reinforced TiAl laminate coupons containing Y_2O_3 interfacial coating [6]. The calculated fracture toughness of as-deposited Y_2O_3 on sapphire was similar to reported values for bulk Y_2O_3. However, the fracture toughness of the Y_2O_3-Nb interface is lower than that previously reported. As a result, the specific fracture energy of the interface was also lower than expected, and is attributed to differences in coating microstructure and weak bonding between as-deposited coatings and the substrates.

These results were related to factors which may affect debonding and fracture toughness of brittle matrix composites. Reactive and non-reactive metal/ceramic systems were reviewed in an effort to understand why this coating performs well. It is postulated that Y_2O_3-coated Nb has an atomically sharp interface which has a lower fracture energy compared to Nb/Al_2O_3, resulting in improved debonding and fracture toughness in Nb-reinforced TiAl [6]. Additional studies must be performed to better quantify the attributes common to fiber/coating/matrix systems that exhibit desirable fracture behavior, and enable predictive guidelines to be used to select debord and protective coatings.

3.6 REFERENCES

1. A.G. Evans and D.B. Marshall, *Acta metall.* 37(1989)2567.
2. H.C. Cao, E. Bischoff, O. Sbaizero, M. Rühle, A.G. Evans, D.B. Marshall, and J.J. Brennan, *J. Amer. Ceram. Soc.* 73(1990)1691.
3. V. Gupta, A.S. Argon, and J.A. Cornie, *J. Mater. Sci.* 24(1989)2031.
4. M. Basche, R. Fanti, and F. Galasso, *Fiber Sci. Technol.* 1(1968)19.
5. F. Wawner, A.Y. Teng, and S.R. Nutt, *SAMPE Quarterly* 14(1983)39.
6. H. Dève, A.G. Evans, G.R. Odette, R. Mehrabian, M. L. Emiliani, and R. J. Hecht, *Acta metall. mater.* 38(1990)1491.
7. J. Davis, H.C. Cao, G. Bao, and A.G. Evans, *Acta metall. mater.* 39(1991)1019.
8. A.G. Evans, A. Bartlett, J.B. Davis, B.D. Flinn, M. Turner, and I.E. Reimanis, *Scripta Metall. et Mater.* 25(1991)1003.
9. W. Mader and M. Rühle, *Acta metall.* 37(1989)853.
10. L.G. Rosenfeld, J.E. Ritter, and T.J. Lardner, Interfaces In Composites, *Mater. Res. Soc. Symp. Proc.*,Vol. 170, Materials Research Society, Pittsburgh, PA, 1990. p. 11-16.
11. T.B. Massalski, Ed., Binary Alloy Phase Diagrams, Vol. 2, American Society for Metals, Metals Park, OH, 1986. p. 1799.
12. M. Abouelleil, L. Conopask, W. Nighan, W. Roman, and D. Price, *Ceramic Trans.* 15(1990)457.
13. C.B. Ponton and R.D. Rawlings, *Mater. Sci. Technol.* 5(1989)961.
14. C.B. Ponton and R.D. Rawlings, *Mater. Sci. Technol.* 5(1989)865.
15. S. Chaing, D. Marshall, and A. Evans in Surfaces and Interface of Ceramics and Ceramic/Metal Systems", J. Pask, and A. Evans, Eds., Plenum Press, New York, NY, 1981. pp. 603-617.
16. R.W. Hertzberg, Deformation and Fracture Mechanics of Engineering Materials, J. Wiley & Sons, New York, NY, 1976. pp. 255-296.
17. B.A. Movchan and A.V. Demshichin, *Phys. Met. Metall.* 28(1969)83.
18. J.A. Thornton, Ann. Rev. Mat. Sci. 7(1977)239.
19. P. Sargent in Microhardness Techniques in Materials Science and Engineering, P. Blau and R. Lawn, Eds., ASTM STP, ASTM, Philadelphia, PA, 1985. pp. 160-174.
20. G. Fantozzi, G. Orange, K. Liang, and E. Gillet, *J. Amer. Ceram. Soc.* 72(1989)1562.
21. P.J. Burnett and D.S. Rickerby, *Thin Solid Films* 148(1987)51.
22. R. Cook, M. Pascucci, and H. Rhodes, *J. Amer. Ceram. Soc.* 73(1990)1873.
23. J. Haggerty, "Production of Fibers by a Floating Zone Fiber Drawing Technique", Final Report, NASA Report # CR-120984, May 1972. p. 52
24. Metals Handbook, Volume 2, Nineth Edition, ASM International, Metals Park, OH, 1979. p. 779.
25. Metals Handbook, Volume 2, Tenth Edition, ASM International, Metals Park, OH, 1990. pp. 567-568.
26. B. Lawn, A. Evans, and D. Marshall, *J. Amer. Ceram. Soc.* 63(1980)574.
27. Reference 16, p. 363.
28. P.M. Fabis, *J. Vac. Sci. Technol.* A5(1987)75.
29. M. Emiliani, M. Richman, and R. Brown, *J. Mat. Sci.* 25(1990)137.
30. M. Emiliani, M. Richman, and R. Brown, *J. Mat. Sci.* 25(1990)144.
31. R. Birringer, *Mat. Sci. Eng.* A117(1989)33.
32. D.J. Srolovitz, *J. Vac. Sci. Technol. A* 6(1986)2925.
33. M. Kuwabara, J.C.H. Spence, and M. Rühle, *J. Mater. Res.* 4(1989)972.
34. F.S. Ohuchi, *J. Mater. Sci. Lett.* 8(1989)1427.
35. J. Kennedy and G. Geschwind in Titanium Science and Technology, Volume 4, R.I. Jaffee and H.M. Burte, Eds., Plenum Press, New York, NY, 1973, p. 2299.

3.6 REFERENCES, CONTINUED

36. J.H. Selverian, M. Bortz, F.S. Ohuchi, and M.R. Notis in Electronic Packaging Materials Science III, R. Jaccodine, K.A. Jackson, and R.C. Sundahl, Eds., Materials Research Society Symposium Proceedings Volume 108, Pittsburgh, PA, 1988. p. 107.
37. M. Bortz and F.S. Ohuchi, *J. Appl. Phys.* 64(1988)2054.
38. S. Morozumi, M. Kikuchi, and T. Nishino, *J. Mater. Sci.* 16(1981)2137.
39. Y. Ishida, H. Ichinose, J. Wang, and T. Suga, *Proc. 46th Annual Meeting of EMSA,* 1988, p. 728.
40. R. Naslain, O. Dugne, A. Guette, J. Sevely, C.R. Brosse, J-P. Rocher, and J. Cotteret, *J. Amer. Ceram. Soc. 74(1991)2482.*
41. H.E. Dève and M.J. Maloney, *Acta metall. mater.* 39(1991)2275.
42. R.C. Weast, Ed., CRC Handbook of Chemistry and Physics, 68th Ed., CRC Press, Inc., Boca Raton, FL, 1987. p. D-51 and D-92.
43. J.A. Thornton in Deposition Technologies for Thin Films and Coatings, R.F. Bunshah, et al., Noyes Publications, Park Ridge, NJ, 1982.
44. M.F. Ashby and D.R.H. Jones, Engineering Materials, Pergamon Press, New York, NY, 1980. Chapters 3 and 4.
45. M.L. Scott in Laser-Induced Damage in Optical Materials, NBS Special Publication 688, November 1985.
46. R.W. Hoffman in Thin Films: Stresses and Mechanical Properties, Materials Research Society Symposium Proceedings, Vol. 130, J.C. Bravman, W.D. Nix, D.M. Barnett, and D.A. Smith, MRS, Pittsburgh, PA, 1989.
47. T.P. Weihs, S. Hong, J.C. Bravman, and W.D. Nix in Thin Films: Stresses and Mechanical Properties, Materials Research Society Symposium Proceedings, Vol. 130, J.C. Bravman, W.D. Nix, D.M. Barnett, and D.A. Smith, Eds., MRS, Pittsburgh, PA, 1989.
48. J.D. Horner in Testing of Metallic and Inorganic Coatings, W.B. Harding and G.A. Bari, Eds., ASTM STP 947, ASTM, Philadelphia, PA, 1987. p. 96.

CHARACTERIZATION OF CONTINUOUS
DUAL LAYER COATED SINGLE CRYSTAL
ALUMINA MONOFILAMENT

4.1 INTRODUCTION

The development of structural intermetallic and ceramic matrix composites will likely require the use of fiber/matrix interfacial coatings. The interface coating developed must an integral part of the composite system development process to ensure applicability. A key feature of composite development is the application of reproducible and well-characterized single, dual, or tri-layer coatings to large quantities of continuous fiber. In addition, continuous fiber coating techniques are essential for the fabrication of large numbers of composite coupons needed to establish material design databases.

The present study examines fiber coatings applied by two continuous processing techniques: direct current (DC) hollow cathode magnetron sputtering and sol-gel. Single layer molybdenum and tungsten coatings were applied to 125 μm diameter sapphire monofilament to assess its viability as a debond coating in γ-TiAl matrices. Dual layer sol-gel Al_2O_3/Mo and sol-gel Al_2O_3/W were applied to 125 μm diameter sapphire monofilament to assess its viability as a debond coating in Al_2O_3 matrices. The fabrication and evaluation of these composites was performed by researchers at the University of California at Santa Barbara(UCSB).

Dual layer sol-gel Al_2O_3/Mo and sol-gel Al_2O_3/W on 125 μm diameter sapphire monofilament were evaluated by analytical transmission electron microscopy (TEM), Auger electron spectroscopy (AES), and secondary ion mass spectroscopy (SIMS) to establish the microstructure and purity of the as-deposited coatings prior to compositing.

4.2 EXPERIMENTAL

4.2.1 Sputtered Coatings

The fiber coated in this study was nominally 125 μm diameter (0001) single crystal alumina monofilament produced by Saphikon, Inc. (Milford, NH). The fiber was purchased without the standard polymeric sizing, and coated by hollow cathode magnetron sputtering in the as-received condition.

The hollow cathode sputtering equipment used to coat fibers continuously was custom-built by Pratt & Whitney, and shown in Figure 1. The pay-off spool of as-received sapphire fiber is enclosed in a bell jar and attached to the take-up spool. The hollow cathode contains two cylinders of the material to be deposited onto the fiber (i.e. target). The cylinders, 0.95 cm thick and 12.2 cm outside diameter, are stacked on top of each other to produce a 12.7 cm long coating zone.

Molybdenum and tungsten interface coatings were selected based upon discussions with researchers at the UCSB. Molybdenum hollow cathode sputtering targets with 99.5 wt.% purity were obtained from GTE Products Corp. (Towanda, PA). The targets were fabricated by extrusion and machined to final tolerances. Tungsten sputtering targets with 99.95 wt.% purity were obtained from Schwarzkopf Development Corp. (Holliston, MA). The targets were fabricated by sintering tungsten powder and machined to final tolerance. The density was >95%.

The deposition rate is enhanced by the use of two external copper coils (i.e. magnetrons) whose magnetic field strength is controlled by the applied current. The system is evacuated and backfilled with argon. The fiber passes through the hollow cathode and is coated to a thickness that depends upon the applied target and magnetron power, argon gas pressure, take-up speed, and target surface area. Coating thicknesses ranged from 0.2-1.5 μm. Typical deposition parameters are shown in Table 1. More detailed description of the sputtering process can be found in reference 1.

TABLE 1 - HOLLOW CATHODE SPUTTERING PARAMETERS

COATING	TARGET POWER Watts	MAGNETRON POWER Watts	ARGON PRESSURE mtorr	FIBER THROUGHPUT cm/hr.
Molybdenum	41.4	1500	50	1800
Tungsten	54	1500	50	76

Tungsten coating was deposited at a much lower rate due to the difficulty in sputtering materials with high atomic mass [1]. The as-coated fiber was found to have improved handleability as a result of the protective metal coating [2]. A summary of all continuous fiber coating runs performed in support of UCSB is presented in the Appendix (Table A2).
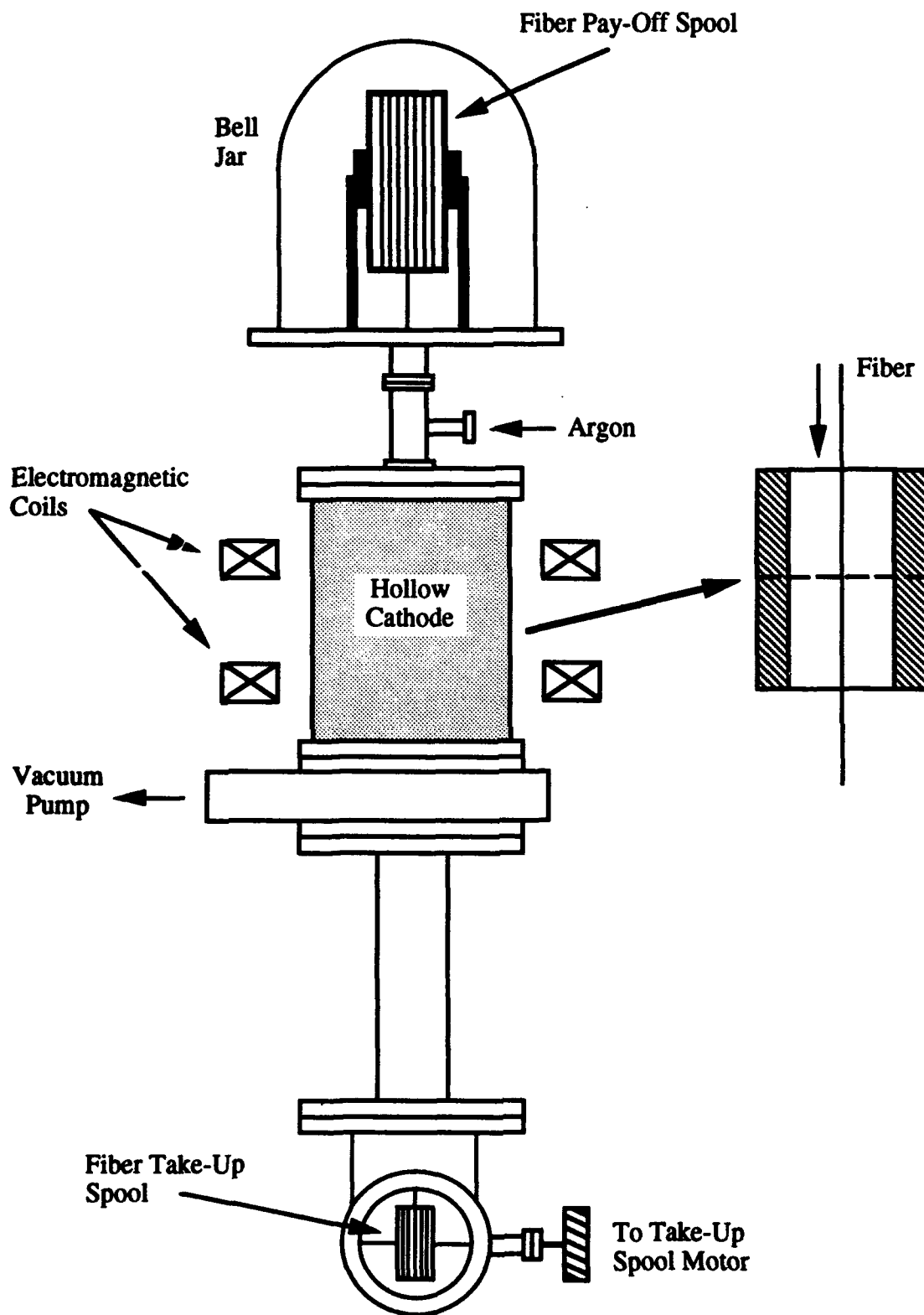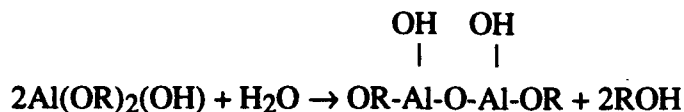
Figure 1. Schematic diagram of the continuous hollow cathode magnetron sputtering system. The sputtering target material consists of two stacked hollow rings 12.2 cm in diameter and 0.95 cm wall thickness (above right).

41

4.2.2 Sol-Gel Coatings

Sol-gel processing was used to apply aluminum oxide coatings ~2 μm thick onto molybdenum or tungsten coated sapphire monofilament. The sol-gel solution was prepared using a modified aluminum alkoxide $(Al(OR)_3)$ route [3,4]. The hydrolyzation reactions occur by mixing aluminum sec butoxide $(Al(OC_4H_9)_3)$ or aluminum isopropoxide $(Al(OC_3H_7)_3)$ precursors in water:

$$Al(OR)_3 + H_2O \rightarrow Al(OR)_2(OH) + R(OH)$$

$$2Al(OR)_2(OH) + H_2O \rightarrow \overset{\displaystyle OH \quad OH}{\underset{\textstyle OR\text{-}Al\text{-}O\text{-}Al\text{-}OR}{\mid \qquad \mid}} + 2ROH$$

The distilled hydroxide is the peptized using nitric acid. The resultant $AlO(OH)_x$ sol contains 60-80 wt.% Al_2O_3.

A schematic diagram of the P&W custom-built continuous fiber coating equipment is shown in Figure 2. The fiber from the pay-off spool is threaded through the sol-gel processing chamber, tube furnace, and attached to the take-up spool. Approximately 1 liter of sol solution is placed in a reservoir that is re-circulated through the sol-gel coating chamber. The fiber is then coated at a rate of ~100 m/hr. for a ~2 μm coating thickness. The fiber passes through a tube furnace maintained at ~650°C to obtain a dehydrated alumina coating. A summary of all continuous single and dual layer fiber coating runs performed in support of UCSB is presented in the Appendix (Table A2).
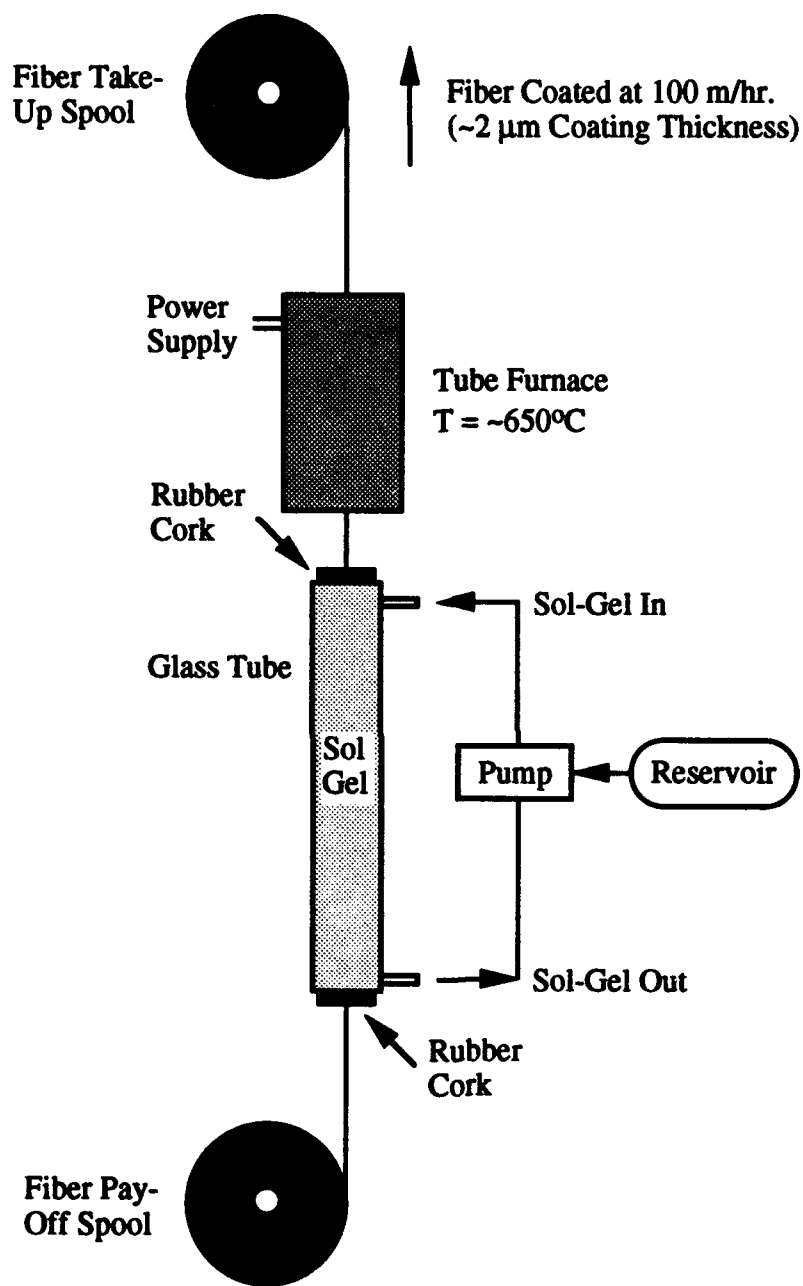
42

Figure 2. Schematic diagram of the continuous sol-gel fiber coating equipment.

4.3 CHARACTERIZATION OF COATED FIBER

The materials selected for characterization are shown in Table 2 [5]. Both samples were dual-layer coated fiber.

TABLE 2 - MATERIAL SELECTED FOR CHARACTERIZATION

FIBER	SPUTTERED INNER COATING	SOL-GEL OUTER COATING
Saphikon (125 μm diam.)	~1.2 μm Mo (A2-92-010)	~1.5 μm Al_2O_3 (J920303-06)
Saphikon (125 μm diam.)	~1.2 μm W (A2-92-024)	~1.5 μm Al_2O_3 (CJ920520-20)

4.3.1 Light Microscopy

Single pieces of coated fiber were placed in 7.6 cm long and 0.95 cm diameter plastic tube filled with Epon 815 epoxy resin and allowed to cure overnight at ambient temperature. The plastic tube was then machined off, and a circumferential notch made in the surface of the epoxy cylinder. The cylinder was then suspended in liquid nitrogen for 15 min., removed and fractured at the notch site. The fracture surfaces were cleaned and dried with Freon gas. Several 1 cm sections were cut from the remainder of the tube and placed in 3.2 cm metallographic mounts. These were again set in Epon 815 epoxy resin and cured overnight at ambient temperature. The mounts were ground using 600 grit paper, then polished with 6 μm and 1 μm diamond paste. Polishing was continued with 1 μm diamond until the fiber surface became optically flat.

4.3.2 Scanning Electron Microscopy

Segments of single coated fiber were embedded in a cylinder of epoxy resin. The coated fiber/epoxy assembly was then fractured to form a transverse fracture surface through the coated fiber without spalling off either coating. The fracture surfaces were carbon coated, then examined with an Amray "1800 Series" field emission scanning electron microscope operated at 15 kV.

4.3.3 Auger Electron Spectroscopy

Short lengths of coated fiber were cleaved and mounted in the scanning Auger spectrometer with the fiber axis oriented at an 80° angle from both the electron beam direction and to the electron optics analyzer so as to reduce static charging induced by the electron beam. A thin coating of colloidal carbon paint was applied to each specimen surface to aid in charge dissipation. Surface spectra were collected from each specimen prior to depth profiling to ensure that the sol/gel alumina was present.

Depth profiles where obtained using 4 keV Ar as the sputter etching source. Spectral information was collected approximately at every 10 nm of depth for the elements Al, C, Mo or W, and O. The spectral data was processed using principal component analysis to improve the dynamic range sensitivity for these elements, and to deconvolute any spectral interferences.

4.3.4 Secondary Ion Mass Spectrometry

Secondary ion mass spectrometry was performed on a similar sample to determine the presence of contaminants using a 20 keV Ga+ ion beam. The elements tracked in the depth profile were those of the known components and contaminates seen in a full spectrum of 1-100 atomic mass units (amu). The masses tracked (in amu) were 12 (C), 16 (O), 23 (Na), 27 (Al), 39 (K), 52 (Cr), 56 (Fe), and 98 (Mo) or 184 (W). The atomic mass data points were collected at approximately 22 nm intervals.

4.3.5 Analytical Transmission Electron Microscopy

Pieces of the dual-coated Saphikon fiber were sectioned with a low-speed rotary saw into ˜4 mm lengths. Six fibers were placed beside each other so as to form a single layer, with the longitudinal axis of each fiber oriented approximately parallel to the eventual foil plane. These grouped fiber lengths were embedded in epoxy resin, cut to fit within a 3 mm circle, and ground and lapped on both sides to ˜75 μm thickness. The samples were dimpled from one side by mechanical grinding to a depth of ˜40 μm, mounted on molybdenum support rings, and thinned to perforation by argon ion milling at 5 kV and 0.5 mA in a liquid nitrogen cooled stage. Thin foils were mounted in a double-tilt analytical goniometer, and examined with a Philips EM400T TEM/STEM operated at 120 kV. Information concerning chemical composition at specific locations within the microstructure was obtained by ultra-thin window energy-dispersive X-ray spectroscopy (EDXS), and by parallel electron energy loss spectroscopy (PEELS).

4.4 RESULTS AND DISCUSSION

4.4.1 Sol-Gel Al_2O_3/Mo/Saphikon

4.4.1.1 Light Microscopy

The sol-gel alumina coating exhibited some variation in thickness (Figure 3). The interface between the sol-gel alumina delaminated during grinding and polishing in every specimen observed.

4.4.1.2 Scanning Electron Microscopy

It was apparent that in contrast to the sol-gel/Mo interface, the Mo/sapphire interface is extremely adherent. This is unexpected since metal films deposited on sapphire are not always particularly adherent [6] and a {001} Mo || {11$\bar{2}$0} Al_2O_3 epitaxial relationship is expected to have the lowest interfacial energy [7]. However, the Saphikon fiber surface changes orientation from {1$\bar{1}$00} to {11$\bar{2}$0} every 30° (the fiber axis is parallel to [0001]). Consequently, a variation in Saphikon/Mo adherence with surface crystal orientation might be reasonably expected, but no microstructural features suggesting poor adhesion (i.e. regions of delamination or voids) were observed. Secondary electron images of the fractured specimen are shown in Figures 4 and 5. The columnar grain structure of the Mo layer is evident in Figure 5, and indicates the grain diameter is in the range of 20-40 nm.

45

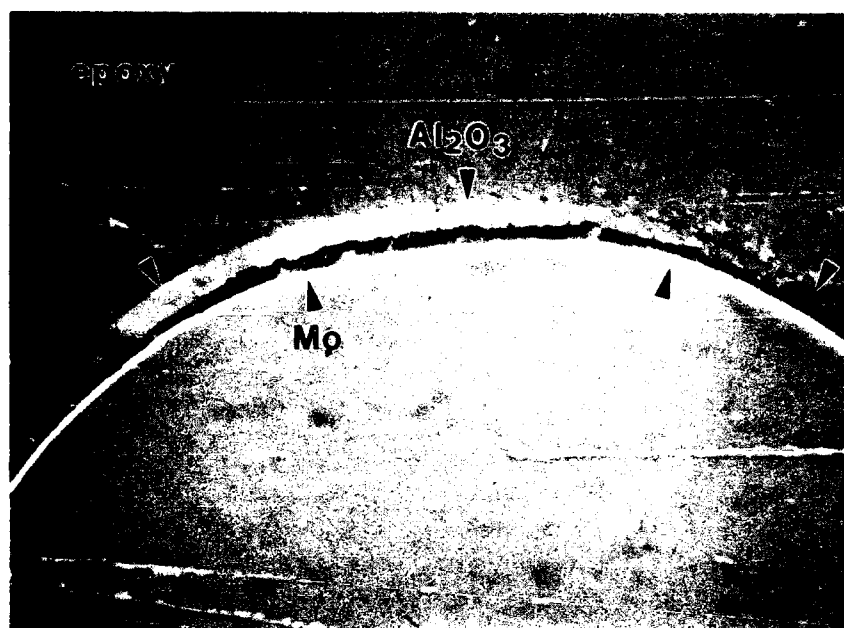Figure 3. Light micrograph of sol-gel Al_2O_3/Mo dual layer coating on single crystal sapphire monofilament. Note the variation in sol-gel Al_2O_3 thickness from left to right.
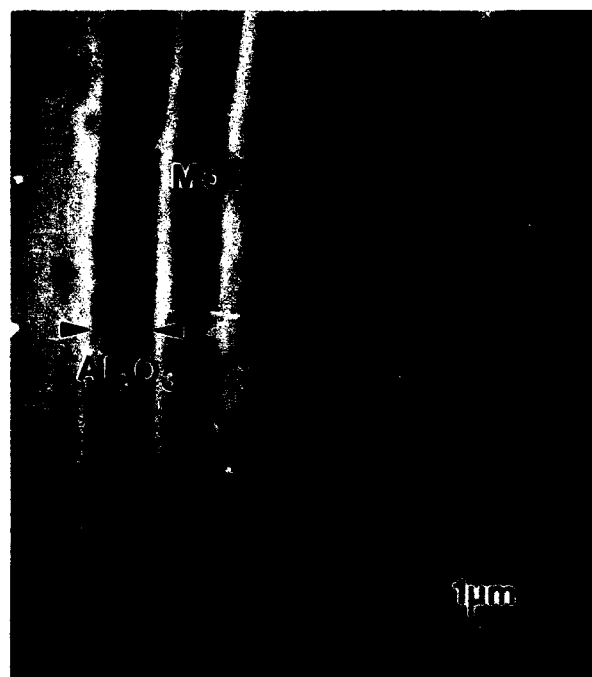

Figure 4. Sol-gel Al_2O_3/Mo dual layer coating on single crystal sapphire monofilament.

46

Figure 5. Secondary electron image of fracture surface showing the sol-gel Al_2O_3 and Mo coatings.

4.4.1.3 Auger Electron Spectroscopy

A segment of the dual layer specimen with the outer sol-gel coating intact is shown in Figure 6. The Auger depth profile (Figure 7) shows that the sol-gel outer layer has the correct Al-O stoichiometry. Some carbon contamination was observed (<0.1 at.%), and assumed to be residue from the sol-gel synthesis or continuous coating process. Much of the apparent variation in carbon concentration in this region was due to specimen charging and uncertainty in data normalization.

The Mo layer contains significant oxygen and carbon contamination. The detection of oxygen appears to be particularly significant, since research concerning the addition of Cr to the metal side of similar interfaces [8] suggests that O might improve the adhesion of Mo to Al_2O_3. Conversely, previously reported to reduce adhesion at metal/ceramic interfaces (e.g., sulfur) [9] were not detected.

4.4.1.4 Secondary Ion Mass Spectrometry

A qualitative SIMS depth profile from the sapphire/Al_2O_3/Mo specimen is plotted as uncorrected intensity vs. sputtering depth in Figure 8. The very low Mo signal across the region where this layer is present is not unusual in SIMS when using Ga ions as the analyzing probe. The Al_2O_3 matrix encapsulating the Mo layer is an oxide and the Mo is mostly metallic, even though some oxide was observed in the AES depth profile analysis. The enhancement of the secondary ion yield is typically three orders of magnitude.

47

In this analysis, if the oxygen ion beam could be focused down to the dimension of the Ga probe, the resulting depth profile would show a significant increase in the Mo ion signal. The depth profile shows detectable signal strength for O, C, Na, and K. The carbon signal confirms that AES data for the presence of carbon in the sol-gel alumina. It is difficult to observe the carbon in the Mo layer; there is a dramatic drop in signal intensity because of the reduction in ion yield between the alumina and molybdenum layers. However, since the Na and K signals remain relatively strong, It appears that the Mo layer is the source for the Na and K. These elements also appear to have diffused into the overlaying and underlying alumina.

Figure 6. Sol-gel Al2O3/Mo dual layer coating on sapphire monofilament. Specimen mounted for composition depth profile by Auger electron spectroscopy. The outer layer of sol-gel Al2O3 has spalled off.
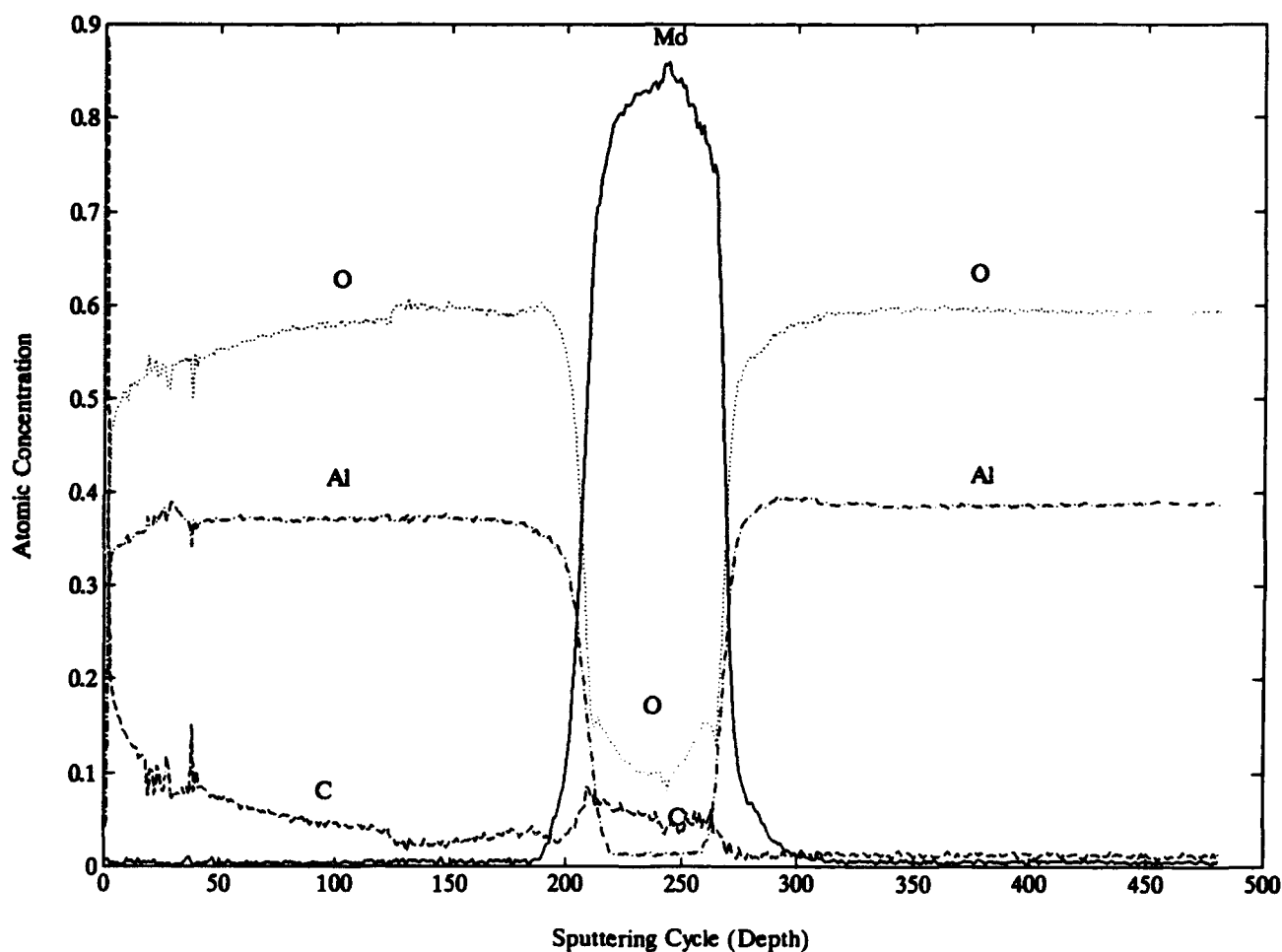
Figure 7. Concentration profile vs. depth obtained by Auger electron spectroscopy. The sol-gel Al_2O_3 coating has contains the correct Al-O stoichiometry (compare to right side showing sapphire Al-O stoichiometry), but contains 3-10 at.% carbon as a contaminant. The Mo coating contains 5-10 at.% C and 10-15 at.% O. Note the higher concentrations of O near the sol-gel Al_2O_3/Mo and Mo/sapphire interfaces. The outer surface is at 0 depth.

Figure 8. Concentration profile vs. depth obtained by SIMS using 20 keV Ga+ ion beam. The depth profile shows detectable levels of O, C, Na, and K. The latter two elements appear to be in the Mo coating.

4.4.1.5 Analytical Transmission Electron Microscopy

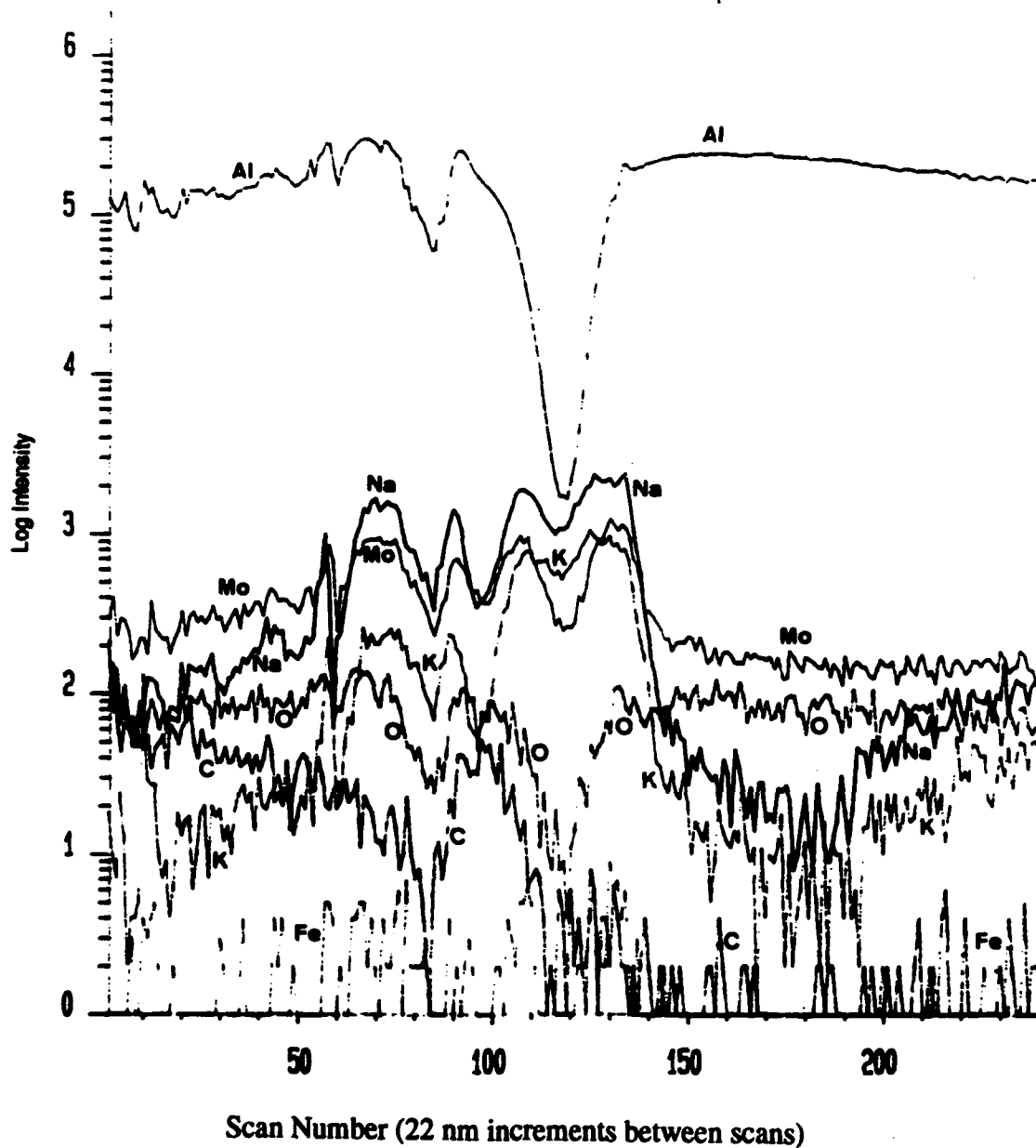The strong adherence of the Mo to the sapphire monofilament, noted during specimen preparation procedures, was reflected in the sharp, narrow appearance of this interface in TEM thin foils. No evidence of delamination or void formation was observed at any magnification. In contrast, the sol-gel delaminated from the Mo quite readily, but was retained and observed in the thin foil specimens.

As suggested by the SEM fractographs, the sputtered Mo layer possessed a distinctly columnar grain structure (Figure 9). A few of the areas in bright contrast are likely subgrains (boundaries of $<10^\circ$ rotation), but the dark field image verifies that the Mo grains are ~20-40 nm in diameter and extend across the entire width of the layer (~1 μm).

Although the pronounced columnar grain structure of the Mo layer suggests that it might possess a sharp crystallographic texture, it was not immediately evident what the crystallographic relationship of the Mo to the sapphire might be. The [101] direction was often, but not always observed to lie parallel to the major axis of the grains (Figure 9). In general, selected area diffraction patterns showed that <110>Mo was also aligned with the [0001] fiber axis. Dark field images using 110Mo ‖ 0006Al$_2$O$_3$ in the same area have similar contrast (Figure 10 vs. the left side of Figure 11) suggesting that this relationship persists. It is probable that the Mo planes parallel to the circumferential surface of the fiber assume a least energy orientation within the <110>Mo zone. "Satellite" spots surrounding the main diffraction spots within selected area diffraction patterns (SADP's), indicative of a periodic defect structure at the Mo/sapphire interface [10] were not observed. Table 3 lists the observed and calculated interplanar spacings found in the Mo coating.

TABLE 3 - ANALYSIS OF SADP FROM MOLYBDENUM COATING (Fig. 12)

RING	PLANE	Mo Interplanar Spacings (nm)	
		OBSERVED	CALCULATED
1	110	0.222	0.2225
2	200	0.156	0.1573
3	211	0.128	0.1284
4	220	0.1105	0.1112

A very faint, irregular ring could be observed on the negative, but not on the print shown in Figure 12, which indexed as 0.236 nm, consistent with the interplanar spacing of (200), Mo$_2$C [11]. This is not definitive evidence for the presence of the carbide, since most SADP's from the Mo coating contained no strong diffraction evidence for Mo$_2$C.

An attempt was made to obtain additional information about the Mo/sapphire interface by means of low resolution lattice imaging. This was only partially successful in the case of the sol-gel Al$_2$O$_3$/Mo/sapphire specimens, since the best areas for observation had accumulated significant electron beam damage. A (0003) image was obtained from the sapphire monofilament (Figure 13). (Note that α-Al$_2$O$_3$ is trigonal, not hexagonal, hence 0002 spots do not occur in any zone axis pattern). However, sufficiently thin areas that also has some Mo present were significantly beam damaged and did not yield useful information. The interface appeared well defined on a scale of nanometers.

51

Dark field images of the sol-gel coating (Figure 14) revealed that it was nearly amorphous, with some small (<0.1 μm), discrete crystalline grains, whose structure was not identified. The diffraction patterns from such areas suggested that the material was beginning to form the crystal structure of a cubic spinel named gamma (common engineering practice) or eta (scientific literature) [12,13].
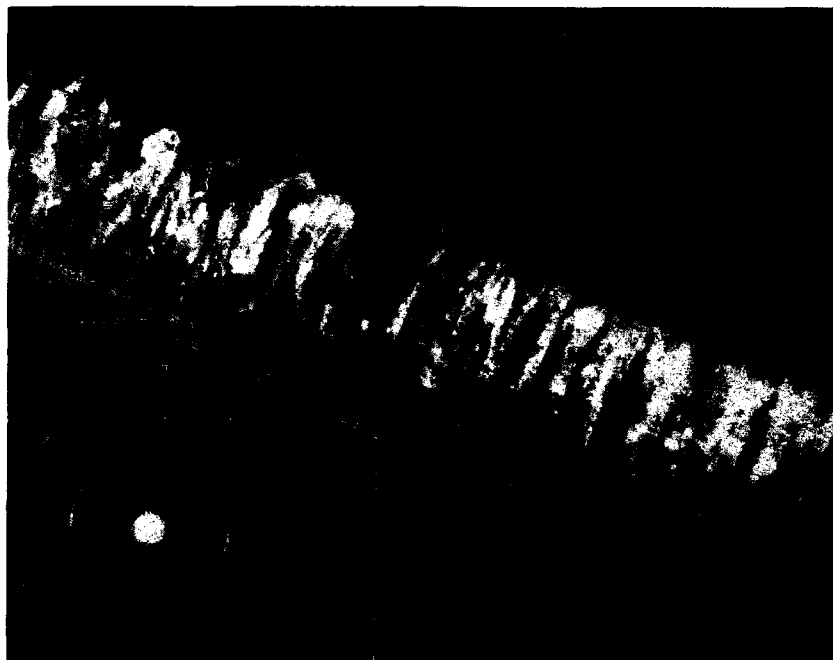
Figure 9. Dark field TEM micrograph of the molybdenum coating on single crystal sapphire monofilament. Diffraction contrast is produced from a short arc of 110Mo diffracted intensity (arrow). The sol-gel alumina was not retained in this area of the ion milled thin foil.
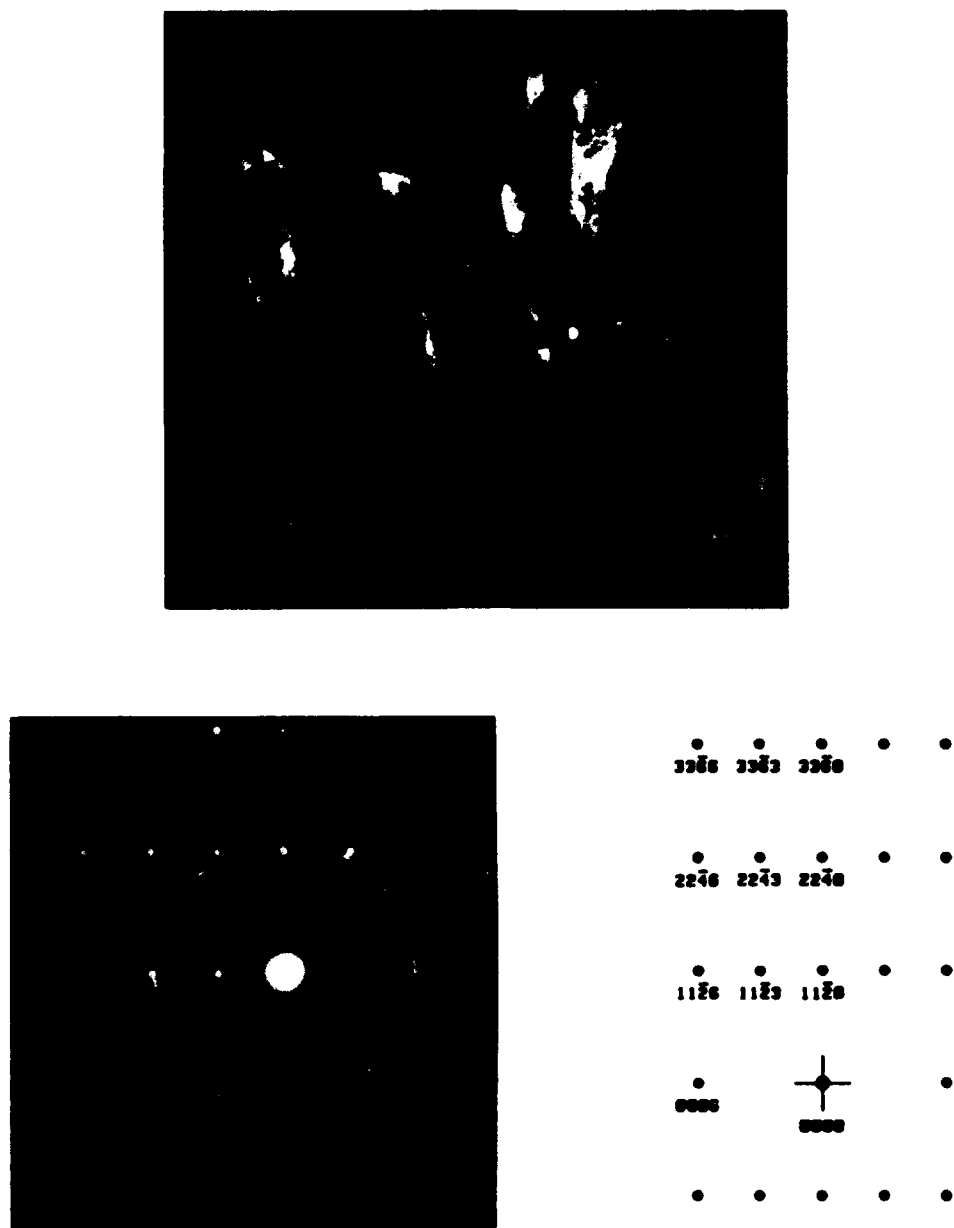
Figure 10. Dark field TEM image and associated SADP for the molybdenum coating. The image is formed by both $0006Al_2O_3$ and $110Mo$ diffracted intensity. Beam direction near $[1\bar{1}00]Al_2O_3$. The 0003 and 0009 spots are present due to double diffraction. The lattice parameters are a = 0.4759 nm and c = 1.2991 nm.
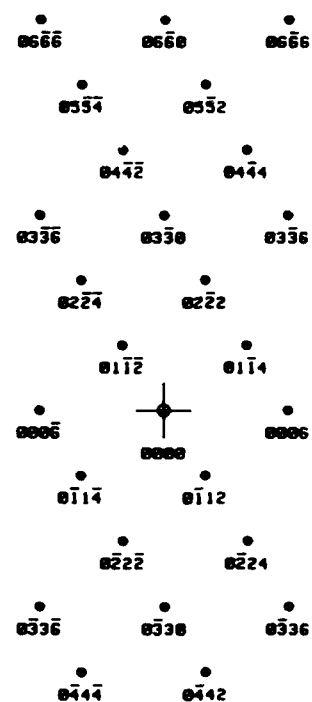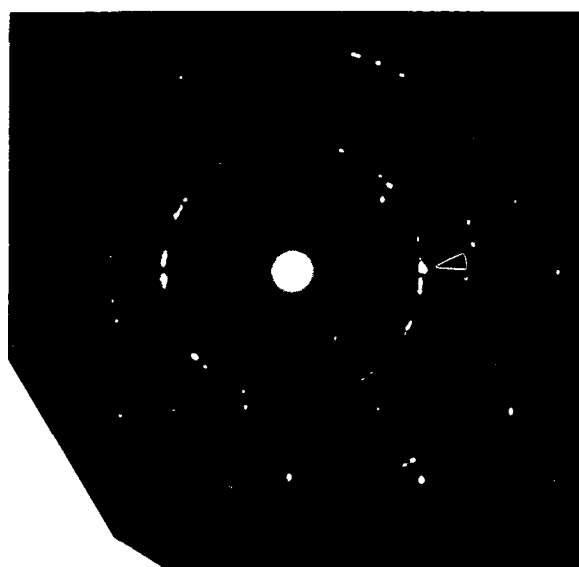
Figure 11. Dark field TEM image and associated SADP for the molybdenum coating. Image formed by combined $0006Al_2O_3$ and $110Mo$ diffracted intensity. The specimen is tilted so that the beam direction is near $[\bar{2}110]Al_2O_3$.
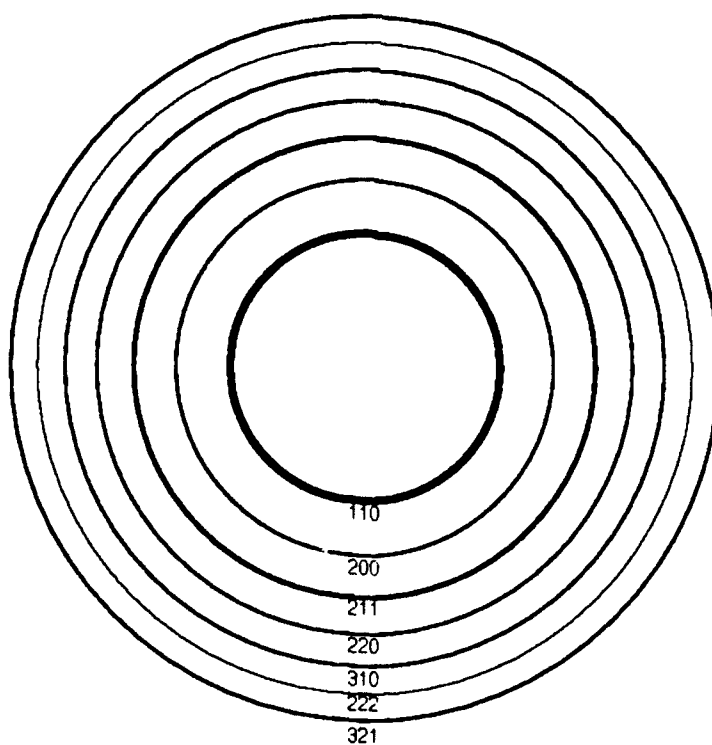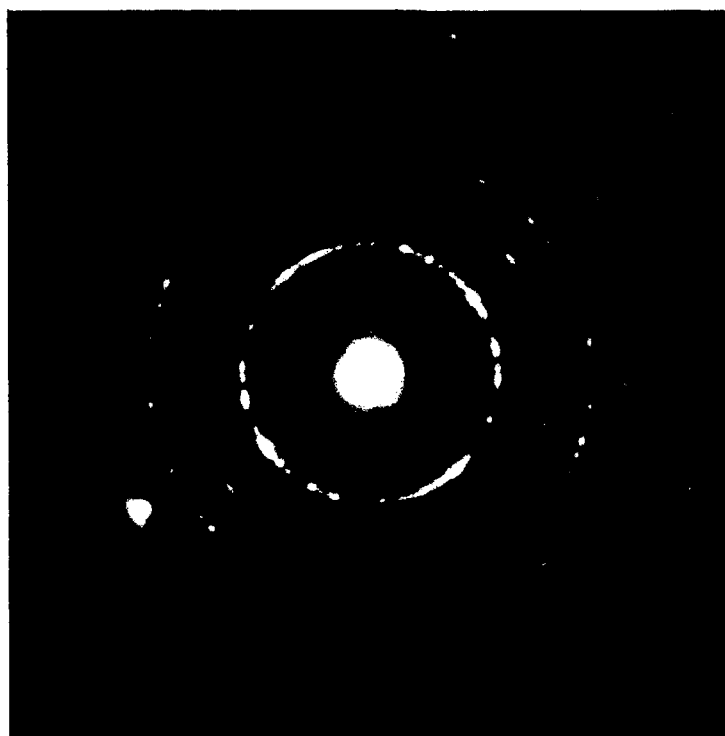
Figure 12. Selected area diffraction pattern from the molybdenum coating shown in Figure 9. The Kikuchi lines and the strong diffraction spot are from the sapphire monofilament, which was not oriented near a major Al_2O_3 zone axis. The diffraction rings were identified as Mo (Table 3).

Figure 13. Low resolution (0003) lattice image of the single crystal sapphire monofilament near its outer surface. The line spacing is 0.433 nm. B = [1$\bar{1}$00], axial illumination. The diffraction conditions and size of variable condenser aperture are as shown. The light spots and dark strain centers are artifacts due to electron beam damage.

Figure 14. Dark field TEM image of the sol-gel alumina coating formed from diffuse 400gamma Al_2O_3 diffracted intensity, with one sharp spot in the objective aperture. The SADP indicates that the coating is beginning to crystallize.

56

4.4.2 Sol-Gel Al₂O₃/W/Saphikon

4.4.2.1 Light Microscopy

The sol-gel alumina coating exhibited relative uniform thickness of ~2-3 μm (Figure 15). However, the interface between the sol-gel alumina delaminated during grinding and polishing.

4.4.2.2 Scanning Electron Microscopy

It is apparent that, as in the case of the Mo/sapphire interface, the W/sapphire interface was extremely adherent. On the other hand, the sol-gel alumina coating could not be retained in an observable location in the fractured specimens. A secondary electron fractograph of the fractured specimen is shown in Figure 16, and clearly reveal the columnar grain structure of the W coating. As in the case of the Mo coating described earlier, the grain diameter of the W coating appears to be in the range of 20-40 nm.

4.4.2.3 Auger Electron Spectroscopy

As in the case of Mo, the Auger depth profile (Figure 17) shows that the sol-gel outer coating has the correct Al-O stoichiometry. There is little carbon contamination, but a significant amount of oxygen was observed in the W, particularly near the sol-gel Al₂O₃/W and W/sapphire interfaces.

4.4.2.4 Secondary Ion Mass Spectrometry

The SIMS depth profile from the sol-gel Al₂O₃/W specimen is plotted as uncorrected intensity vs. sputtering depth (Figure 18). As in the case of the Mo specimen, there is a very low W signal across the region where this coating is present. The origin of the strong amu 27 signal (normally Al) from the region of the W may be due to the presence of an ethylene (C_2H_3, amu 27) in this coating. The depth profile also shows detectable signal strength for Na, and K, particularly in the W coating.

4.4.2.5 Analytical Transmission Electron Microscopy

A low magnification dark field image which contains both the sol-gel Al₂O₃ and the sputtered W coatings is shown in Figure 19. Unfortunately, the sol-gel/W interface delaminated in all observably thin areas. As with the Mo specimen, the W coating was confirmed to have a distinctly columnar structure (Figures 20 and 21) containing grains ~20-40 nm in diameter. The SEM fractographs indicate that the W grains extend across the entire width of the coating (~1 μm), although this could not be confirmed by TEM observation, as the W transmits 120 kV electrons less efficiently than Mo. The <101> directions was often observed to lie parallel to the long axis of the grains (Figure 21), but the orientation of 110W ‖ 0006Al₂O₃ was much less frequently observed, compared to the sputtered Mo specimens.

Evidence for small quantities of other crystalline phases in the W near the W/sapphire interface was manifested as a faint ring of spots well within the 110W ring in SADP's (Figure 22). (The W near the former sol-gel/W interface was usually too thick for observation). The diameter of this ring corresponded to in interplanar spacing of 0.380±0.001 nm, and is consistent with the interplanar spacings of the {200} family of planes for tungsten oxides of stoichiometry WO$_{2.9}$-WO₃ [14]. In view of the complexity of the crystal structures of tungsten oxide [15], further diffraction analysis was not attempted. Dark field imaging using portions of this ring yielded extremely weak and inconclusive contrast.

Low resolution lattice imaging was utilized in an attempted to determine the physical location of the phases assumed to be tungsten oxide. This was successful, in that many small (3-6 nm) regions were observed in the W, characterized by lattice fringe spacings in the range of 0.32-0.4 nm (Figure 23). These are probably small grains of tungsten oxide, as suggested by the Auger depth profile (Figure 17). They cannot originate from pure W, which would be manifested as a maximum line spacing of 0.2238 nm (110)W, which is greater than the resolution of the TEM used.

As in the case of the Mo specimen, dark field images of the sol-gel alumina coating (Figure 24) revealed that it was nearly amorphous. Selected area diffraction patterns from such areas suggested that this coating was beginning to form the crystal structure of a cubic spinel. Parallel electron energy loss spectroscopy of the sapphire fiber and sol-gel alumina (Figure 25) revealed only Al and O edges. No other elements were detected by this technique.
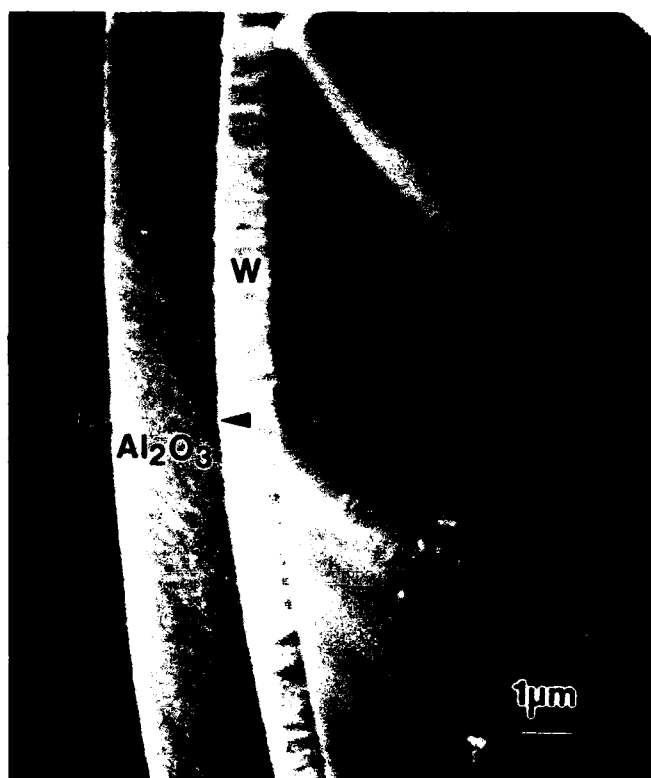
Figure 15. Micrograph of the sol-gel Al_2O_3/W dual layer coating on single crystal sapphire monofilament.

58

Figure 16. High resolution SEM images of the tungsten fracture surface. The sol-gel Al$_2$O$_3$ coating has delaminated and is not present in this photomicrograph.
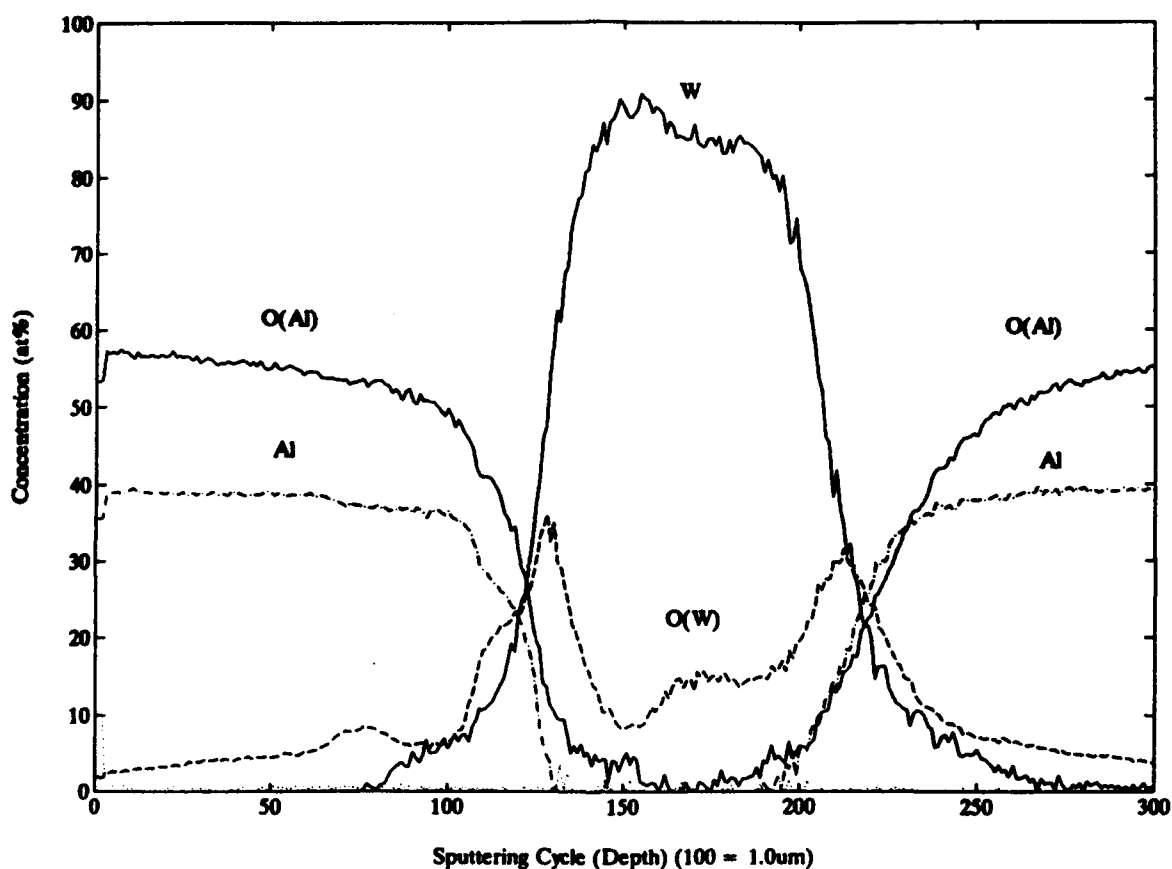
Figure 17. Concentration profile vs. depth obtained by Auger electron spectroscopy. The sol-gel Al_2O_3 coating has contains the correct Al-O stoichiometry (compare to right side showing sapphire Al-O stoichiometry). There is less carbon contamination, but higher concentrations of O (~35 at.%) near the sol-gel Al_2O_3/W and W/sapphire interfaces. The outer surface is at 0 depth.
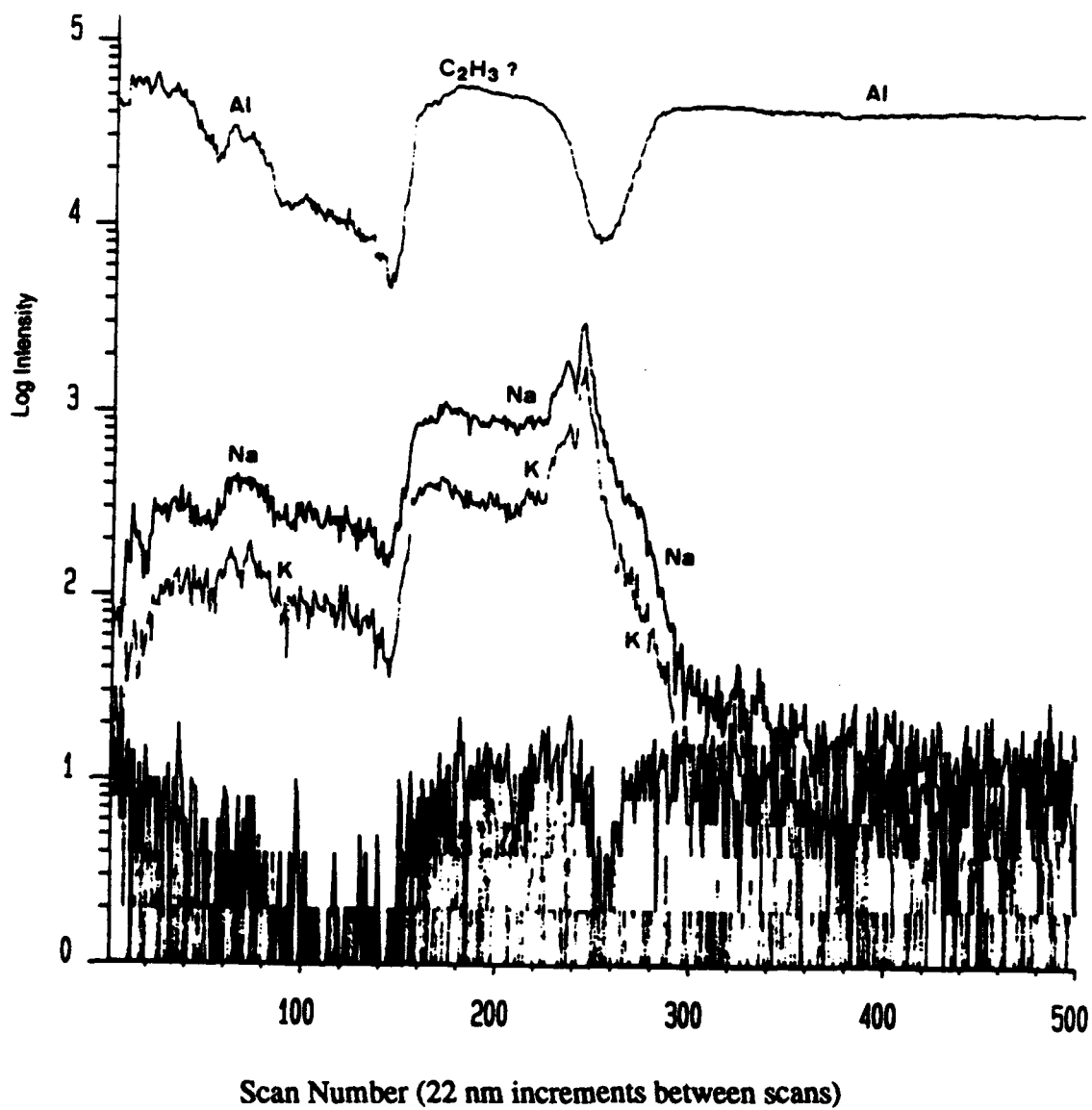
Figure 18. Concentration profile vs. depth obtained by SIMS using 20 keV Ga+ ion beam. The depth profile shows detectable levels of Na and K in the W coating.

Figure 19. Low magnification dark field TEM micrograph of the sol-gel alumina and tungsten coatings on single crystal sapphire monofilament. Arbitrary diffraction conditions.
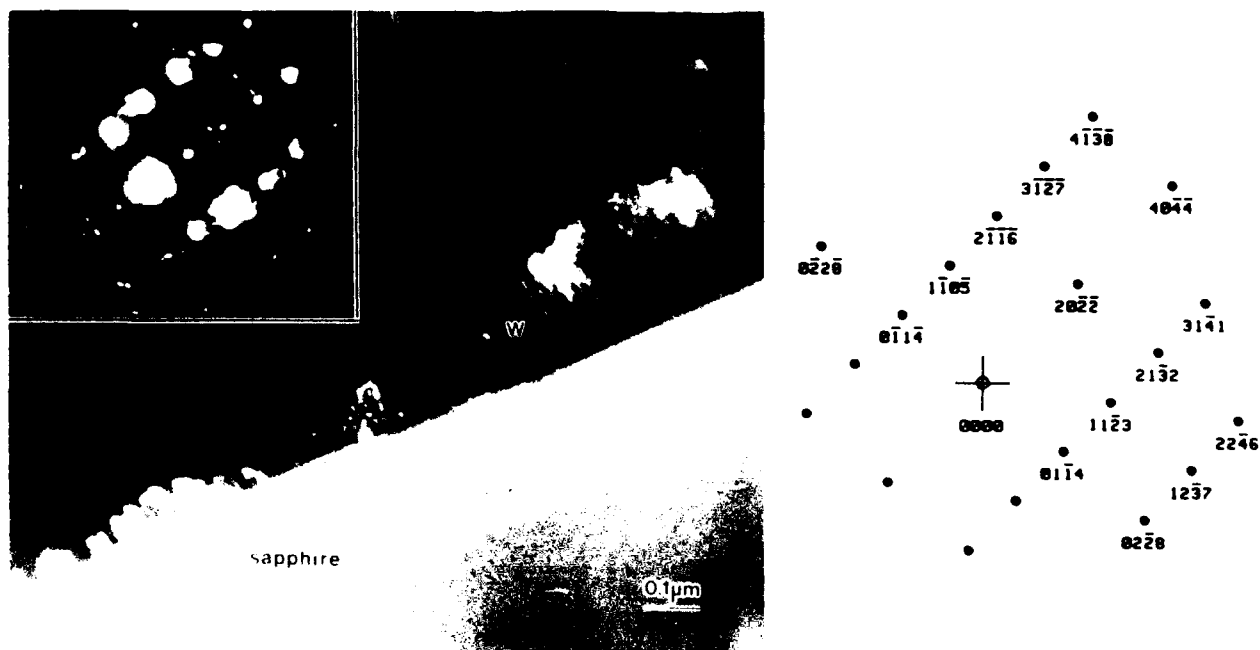
Figure 20. Dark field TEM image and associated SADP of the tungsten coating. Pointer marks both $\bar{2}022Al_2O_3$ and $\bar{1}10W$ diffracted intensity used to form image. The beam direction is near $[\bar{2}3\bar{1}\bar{1}]Al_2O_3$. The $10\bar{1}\bar{1}$ and $30\bar{3}\bar{3}$ spots present due to double diffraction.

62
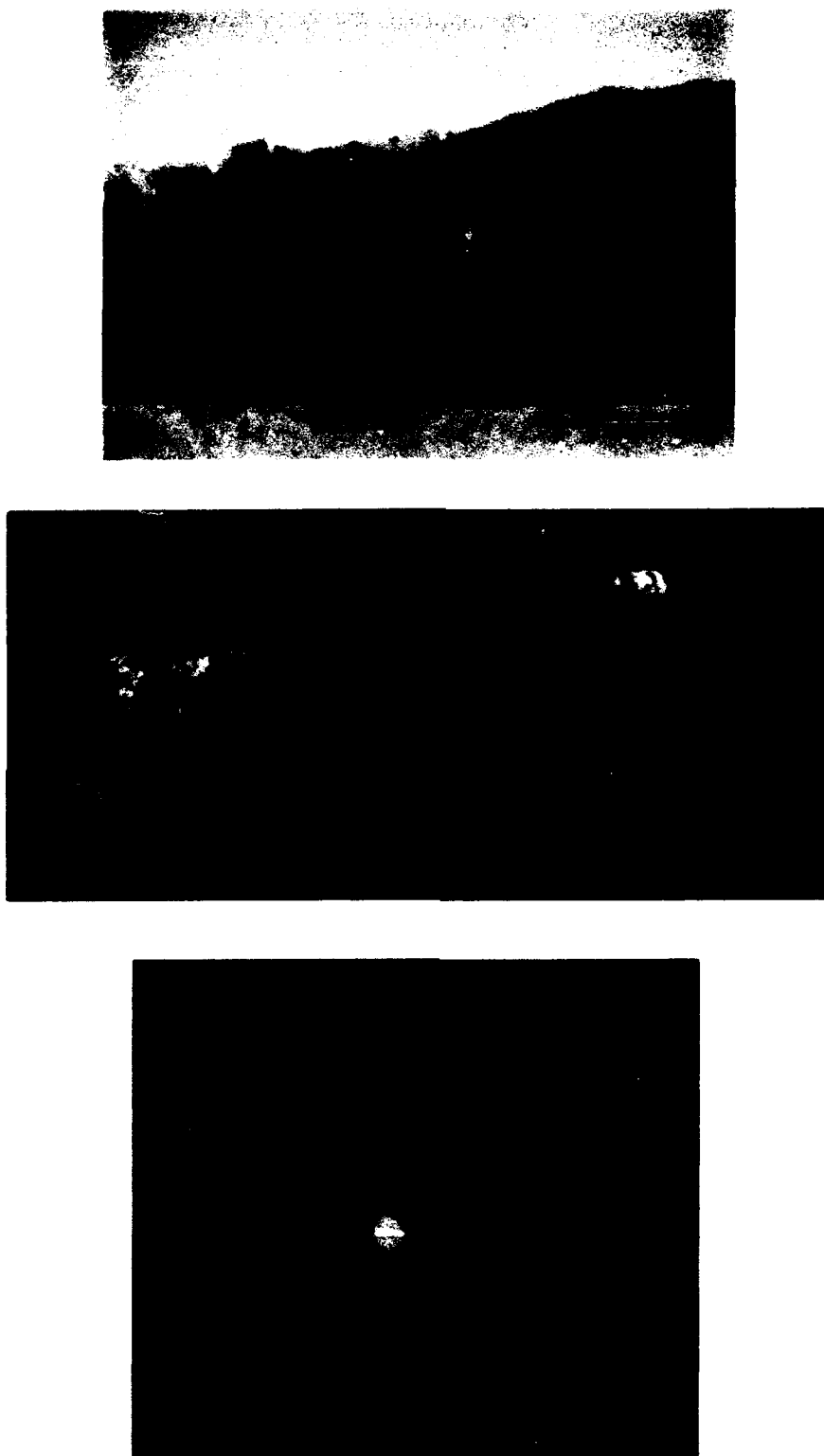
Figure 21. Tungsten coating on single crystal sapphire monofilament. (a) Bright field TEM micrograph. The outer sol-gel coating is not present in this region of view. (b) Dark field TEM at lower magnification. Left side of (b) overlaps right side of (a). (c) Associated SADP. Arrow marks the two 110W spots used to form image. The Kikuchi lines and outer intense spots are from the Al_2O_3 monofilament fiber.

63

Figure 22. Superimposed selected area diffraction patterns from the area shown in Figure 20. The zone axis of the sapphire monofilament pattern is [2$\bar{1}\bar{1}$0]. The faint inner ring is attributed to the presence of tungsten oxide.

Figure 23. Low resolution (01̄12) lattice image of single crystal sapphire monofilament with tungsten coating attached. Line spacing 0.348 nm. B̄ = [2̄1̄10], axial illumination. The diffraction conditions and condenser aperture size are as shown. The short arcs in the diffraction pattern are from 110W. Lattice images in the tungsten coating near the interface (arrows) suggest the presence of tungsten oxide.
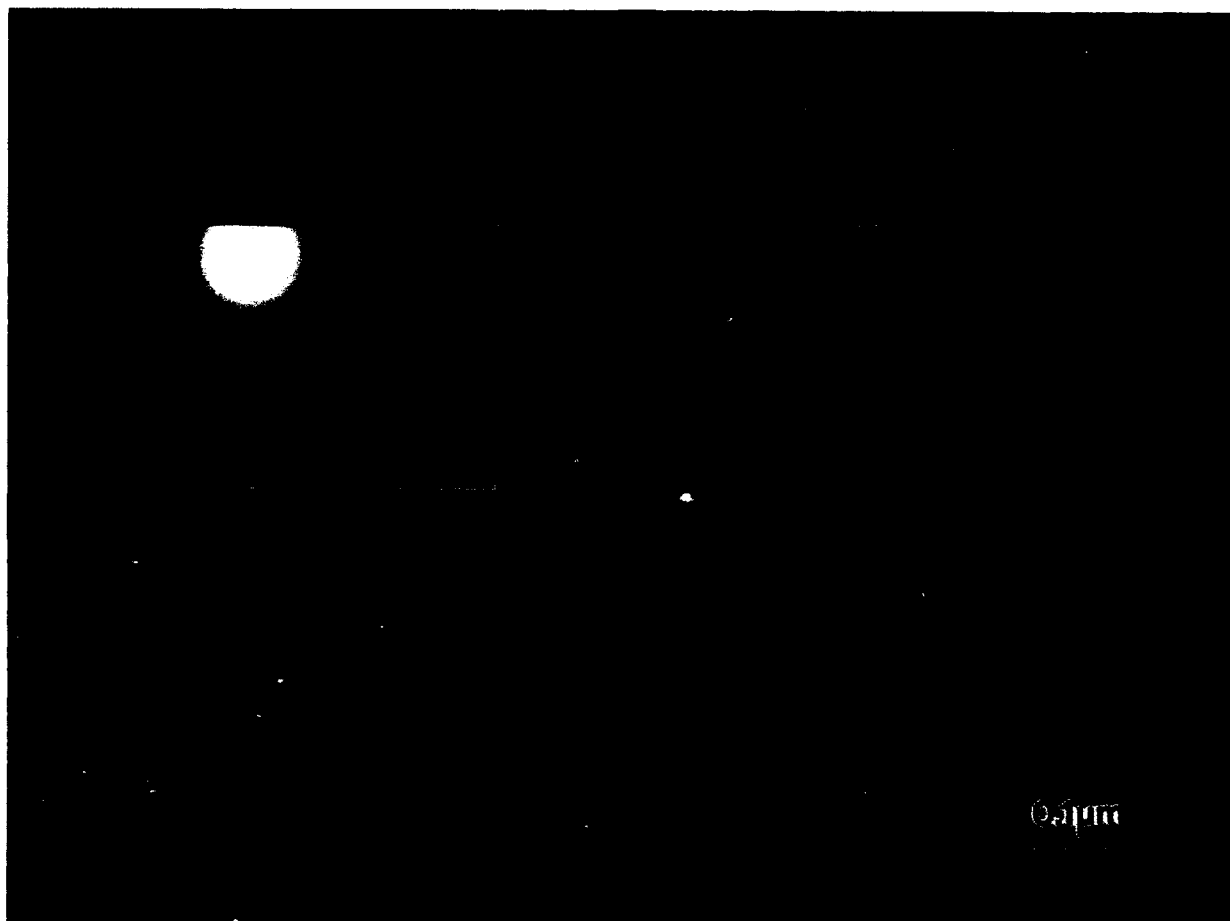
Figure 24. Sol-gel alumina coating shown in Figure 19. Dark field TEM image formed from diffuse 400gamma Al_2O_3 diffracted intensity. The SADP indicates that most of this area of the sol-gel coating is beginning to crystallize.

66

Aluminum L Edges

Saphikon Fiber

Sol-Gel Alumina Coating

Aluminum L2,3 Edges

Aluminum L1 Edge

Photodiode Counts × 1000 (y-axis)
Energy-Loss (eV) (x-axis)

Oxygen K Edges

Saphikon Fiber

Sol-Gel Alumina Coating

Photodiode Counts (y-axis)
Energy-Loss (eV) (x-axis)
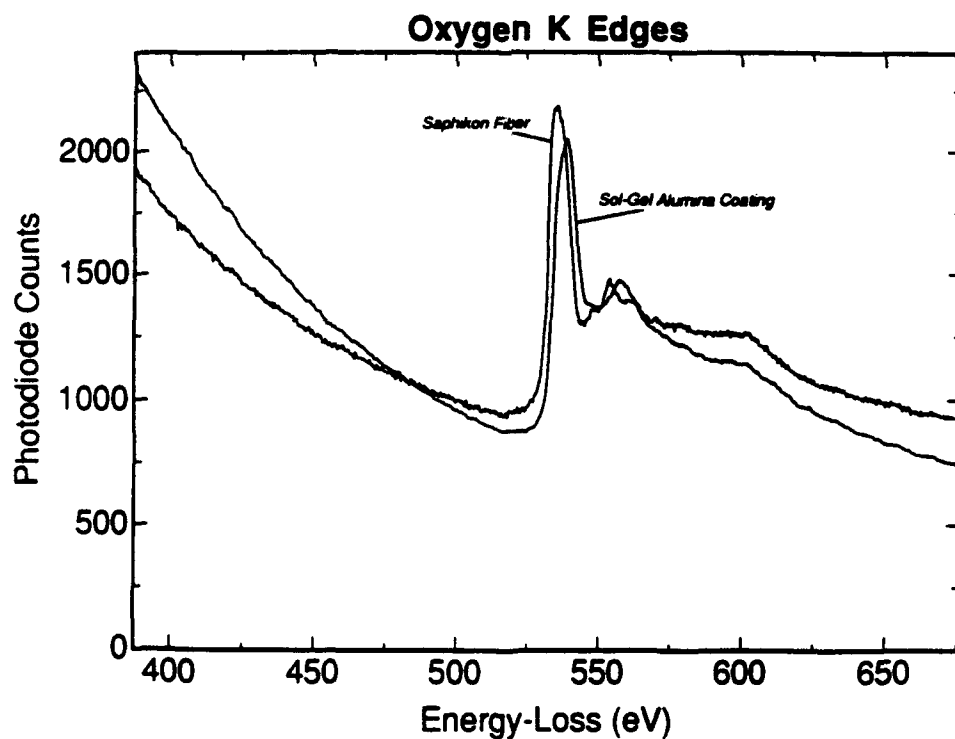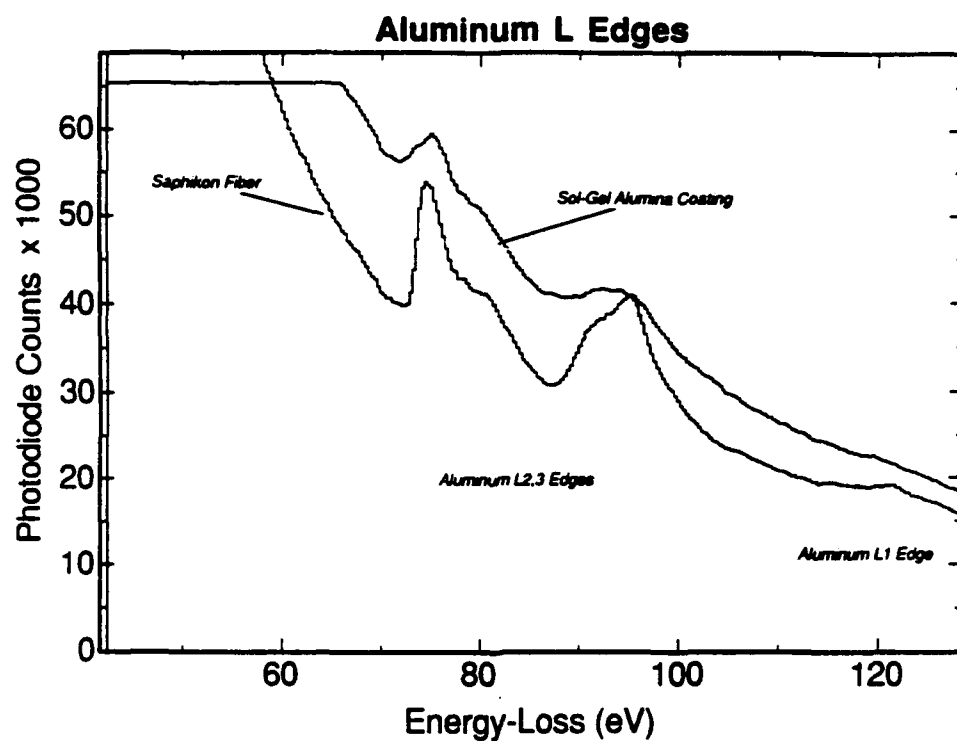
Figure 25. Aluminum and oxygen edges within parallel electron energy loss spectra from the sol-gel coating and sapphire monofilament within the region shown in Figure 19. No other elements were detected by this technique.

67

4.5 CONCLUSIONS

Both of the specimen groups evaluated were confirmed to have an outer coating of ~3 μm of sol-gel alumina and an ~1 μm inner coating of either molybdenum or tungsten. The sol-gel coating on the Mo coated specimens appeared to have more variability in thickness (2-4 μm). Most of the sol-gel outer coating consisted of nearly amorphous alumina, which appeared to be transforming to microcrystalline γ-alumina (cubic spinel). Both the Mo and W coatings consisted of columnar grains, 20-40 nm in diameter, and extending across the full coating width.

The only significant impurities detected by AES or SIMS were C and O in the Mo coating and O in the W coating, particularly near the sol-gel and sapphire interfaces. Evidence for 3-6 nm regions of tungsten oxide in the W coating near the sapphire monofilament was found by low resolution lattice imaging and selected area diffraction. Both the Mo and W coatings exhibited a tendency for grain orientations with <101> parallel to the fiber radius and <110> parallel to the [0001] fiber axis.

The sol-gel Al_2O_3/Mo and sol-gel Al_2O_3/W interfaces were extremely friable, while the corresponding interfaces with the sapphire monofilament were extremely adherent. Oxide interfaces adjacent to the metal coatings contained significantly higher concentrations of oxygen than in the bulk, presumably due to sputtering and sol-gel processing conditions that exposed the fiber to ~650°C.

68

4.6 REFERENCES

1. B.N. Chapman, Glow Discharge Processes, J. Wiley and Sons, New York, NY, 1980.
2. H. Landis, J. Unnam, S.V.N. Naidu, and W. Brewer, SAMPE Quarterly, July 1991.
3. B.E. Yoldas, *Ceram. Bull.* 54(1975)289.
4. B.E. Yoldas, *J. Mater. Sci.* 10(1975)1856.
5. D.B. Snow and G.G. Peterson, "Characterization of Single and Dual Layer Coated Fiber", UTRC Report No. R92-271552-1, 14 August 1992.
6. A. J. Pedraza and M. J. Codbole, *Metall. Trans. A*, 23A(1992)1095.
7. M. Kuwabara, J. C. H. Spence, and M. Rühle, *J. Mater. Res.* 4(1989)972.
8. P. Kritsalis et al., *Acta Metall. Mater.*, 40(1992)1167.
9. D. P. Pope and M. A. Smith, "The Effect of Trace Element Segregation to Fe/Sapphire Interfaces," in Structure and Properties of Interfaces in Materials, W. A. T. Clark, U. Dahmen, and C. L. Briant, Eds., Materials Research Society Symposium Proceedings Vol. 238, Materials Research Society, Pittsburgh, 1992, pp. 427-432.
10. L. A. Tietz and C. B. Carter, *J. Amer. Ceram. Soc.*, 75(1992)1097.
11. F. A. Shunk, Constitution of Binary Alloys, Second Supplement, McGraw-Hill, New York, New York, 1969, p. 150.
12. K. Wefers and G. M. Bell, "Oxides and Hydroxides of Aluminum," Technical Paper No. 19, Alcoa Research Laboratories, 1972.
13. C. G. Levi et al., *J. Mater. Res.*, 3(1988)969.
14. JCPDS Search Manual for Selected Powder Diffraction Data for Metals and Alloys, First Edition, JCPDS, 1978, Swarthmore, PA, p. 149.
15. R. P. Elliott, Constitution of Binary Alloys, First Supplement, McGraw-Hill, New York, New York, 1965, pp. 705-706.

5.0 CONCLUSIONS

The results of the base and option program studies have demonstrated, in collaboration with researchers at the University of California at Santa Barbara, a systematic approach to identifying fiber/matrix interfacial coatings. Candidate coatings applied by batch sputtering were evaluated by UCSB in model systems, then downselected and applied by P&W using continuous processing techniques. The continuous coated fiber was supplied to UCSB for the fabrication of composite coupons and validation of model results. Interfacial coatings have been developed for selected composite systems that are capable of promoting interfacial debonding (see publications cited in the Appendix, p. 71).

The principal technical accomplishments of the P&W focused studies include:

- Indentation tests could not be easily used as a screening test for candidate coatings to assess their fracture toughness, interfacial fracture toughness, or specific fracture energy.

- The calculated fracture toughness of as-deposited Y_2O_3 coatings on sapphire was similar to reported values for bulk Y_2O_3.

- The low fracture toughness and specific fracture energy of the Y_2O_3-Nb interface is attributed to differences in coating microstructure and weak bonding between as-deposited coatings and the substrates.

- Y_2O_3-coated Nb has an atomically sharp interface after hot-pressing that has a lower fracture energy compared to Nb/Al_2O_3, resulting in improved debonding and fracture toughness in Nb-reinforced TiAl.

- Predictive guidelines could not be developed to select debond and protective coatings due to the complicated interdependence of numerous variables.

- Dual layer metal/oxide coatings on sapphire monofilament contained a nearly amorphous γ-alumina (cubic spinel). Both the Mo and W coatings consisted of columnar grains, 20-40 nm in diameter and extending across the entire coating thickness.

- C and O were found in the Mo coating, and O in the W coating. Increased concentrations of O were found near the sol-gel alumina and sapphire interfaces.

- Tungsten oxide particles, 3-6 nm in diameter, were found near the sapphire fiber.

- Mo and W coatings exhibited a tendency for grain orientations with <101> parallel to the fiber radius and <110> parallel to the [0001] fiber axis.

- The sol-gel Al_2O_3/Mo and sol-gel Al_2O_3/W interfaces were friable, while the corresponding interfaces with the sapphire fiber were adherent.

70

6.0 APPENDIX

During this contract, Pratt & Whitney also provided direct support to several scientists at the University of California at Santa Barbara (UCSB) whose research was dedicated towards improving the fracture toughness of brittle matrix composites. Thus, a variety of single and dual layer coatings have been applied in support of these activities at no cost to UCSB.

Table A1 summarizes coatings applied in the base program for UCSB from 15 May 1989 to 14 March 1991. Over 180 samples were coated during this period.

Table A2 summarizes coatings applied in the base program for UCSB from 15 March 1991 to 14 August 1992. Over 200 samples were batch coated by RF sputtering, and over 2600 m of fiber was continuously coated using hollow cathode sputtering and sol-gel.

The following are selected journal papers published or in press describing the results of studies using P&W coated material produced in this program:

- H. Dève, A.G. Evans, G.R. Odette, R. Mehrabian, M. L. Emiliani, and R. J. Hecht, *Acta metall. mater.* 38(1990)1491.
- J.B. Davis, E. Bischoff, and A.G. Evans in Advanced Composite Materials, M.D. Sacks, Ed., American Ceramic Society, Westerville, OH, 1991, p. 631.
- T.C. Lu, Y.G. Yeng, C.G. Levi, and R. Mehrabian in Advanced Metal matrix Composites for Elevated Temperatures, M.N. Gungor et al., Eds., ASM Conference Proceedings, ASM International, Metals Park, OH, 1991.
- J. Davis, H.C. Cao, G. Bao, and A.G. Evans, *Acta metall. mater.* 39(1991)1019.
- A.G. Evans, F.W. Zok, and J.B. Davis, in *Composites Sci.& Tech.*, 42(1991)3.
- T.C. Lu, A.G. Evans, R.J. Hecht, and R. Mehrabian, *Acta metall. mater.* 39(1991)1853.
- A.G. Evans, A. Bartlett, J.B. Davis, B.D. Flinn, M. Turner, and I.E. Reimanis, *Scripta Metall. et Mater.* 25(1991)1003.
- M-Y. He, A. Bartlett, and A.G. Evans, *J. Amer. Ceram. Soc.* 74(1991)767.
- M.L. Emiliani and H.E. Dève, *J. Amer. Ceram. Soc.* 75(1992)1935.
- M. Emiliani, "Debond Coating Requirements for Brittle Matrix Composites". Submitted to *J. Mat. Sci.*
- J.B. Davis, J.P.A. Löfvander, A.G. Evans, E. Bischoff, and M.L. Emiliani, "Some Fiber Coating Concepts for Brittle Matrix Composites". Submitted to *J. Amer. Ceram. Soc.*
- R. Hanson et al., "A Fiber Coating Concept for TiAl Reinforced with Oxide Fibers" in preparation.

TABLE A1 - MATERIALS COATED[a,b] (5/15/89 - 3/14/91)

NUMBER & TYPE OF SUBSTRATES	COATING RUN NO.	COATING & THICKNESS	NOTES
3 - Al_2O_3 Wafers	6-89-036	Y_2O_3 - 2 μm	Coat Both Sides
3 - Al_2O_3 Wafers	6-89-037	Y_2O_3 - 2 μm	Coat Both Sides
1 - Al_2O_3 Wafers	6-89-038	Y_2O_3 - 2 μm	Coat Both Sides
2 - Al_2O_3 Discs	6-89-042	ZrO_2 - 2 μm	Coat One Side
2 - Al_2O_3 Discs	6-89-045	NiAl - 2 μm	Coat One Side
2 - Al_2O_3 Discs	6-89-046	Mo - 2 μm	Coat One Side
2 - Al_2O_3 Discs	6-89-048	Nb - 2 μm	Coat One Side
3 - Al_2O_3 Discs	6-89-049	Y_2O_3 - 2 μm	Coat One Side
2 - Al_2O_3 Discs	6-89-057	Nb - 2 μm	Coat One Side
1 - Al_2O_3 Discs	6-89-058	Nb - 5 μm	Coat One Side
1 - Al_2O_3 Discs	6-89-059	Nb - 10 μm	Coat One Side
2 - Al_2O_3 Discs	6-89-061	Y_2O_3 - 2 μm	Coat One Side
1 - Tungsten Foil	6-89-062	Y_2O_3 - 4 μm	Coat One Side
1 - Niobium Foil	6-89-063	Y_2O_3 - 4 μm	Coat One Side
1 - Tungsten Foil	6-89-064	Al_2O_3 - 2 μm	Coat Both Sides
1 - Al_2O_3 Disc	6-90-004	Pt - 2 μm	Coat One Side
1 - Al_2O_3 Disc	6-90-005	Mo - 2 μm	Coat One Side
1 - Al_2O_3 Disc	6-90-006	W - 2 μm	Coat One Side
1 - Al_2O_3 Disc	6-90-007	W - 2 μm	Coat One Side
7 - Saphikon Fibers	6-90-008	Mo - 6 μm	-
7 - Saphikon Fibers	6-90-009	ZrO_2 - 6 μm	-
7 - Saphikon Fibers	6-90-010	C - 2 μm	-
7 - Saphikon Fibers	6-90-011	C - 2 μm	Double Layer
7 - Saphikon Fibers	6-90-012	TiAl - 6 μm	Coating
7 - Saphikon Fibers	6-90-013	TiAl - 6 μm	-
1 - Niobium Foil	J900208-06	Al_2O_3 - 2 μm	Sol-Gel Coating
1 - Niobium Foil	J900208-06	Y_2O_3 - 2 μm	Sol-Gel Coating
2 - Al_2O_3 Discs	J900208-06	Y_2O_3 - 2 μm	Sol-Gel Coating
2 - Al_2O_3 Discs	6-90-014	Mo - 2 μm	Coat One Side
2 - Al_2O_3 Discs	6-90-015	ZrO_2 - 2 μm	Coat One Side
2 - Niobium Foils	6-90-019	Y_2O_3 - 2 μm	Coat One Side
2 - Al_2O_3 Wafers	6-90-036	Mo - 7 μm	Coat One Side
2 - Al_2O_3 Discs	6-90-036	Mo - 7 μm	Coating Spalled
2 - Al_2O_3 Discs	6-90-037	Zr - 8 μm	Coating Spalled
2 - Al_2O_3 Discs	6-90-038	Zr - 2 μm	Coat One Side
2 - Al_2O_3 Discs	6-90-039	Cr - 2 μm	Coat One Side
2 - Al_2O_3 Discs	6-90-040	W - 2 μm	Coating Spalled
2 - Al_2O_3 Discs	6-90-041	Ta - 2 μm	Coat One Side
2 - Al_2O_3 Discs	6-90-042	Zr - 2 μm	Coat One Side
2 - Al_2O_3 Discs	6-90-043	Mo - 2 μm	Coat One Side
3 - Al_2O_3 Rods	6-90-044	Mo - 2 μm	-

a Coatings thicknesses are nominal.
b Al_2O_3 wafers, discs, and rods, with a few exceptions, are single crystal sapphire (0001) orientation.

72

TABLE A1, CON'T. - MATERIALS COATED[a,b] (5/15/89 - 3/14/91)

NUMBER & TYPE OF SUBSTRATES	COATING RUN NO.	COATING & THICKNESS	NOTES
3 - Al_2O_3 Rods	6-90-044	Mo - 2 μm	Double Layer
3 - Al_2O_3 Rods	6-90-045	ZrO_2 - 0.5 μm	Coating
9 - Sapphire Discs	6-90-053	W - 2 μm	Coat One Side
6 - Saphikon Fibers	6-90-056	Mo - 5 μm	-
1 - TiAl Disc	6-90-057	W - 3 μm	Coat One Side
8 - Sigma Fibers	6-90-057	Mo - 2 μm	-
6 - Saphikon Fibers	6-90-058	C - 2 μm	-
8 - Sigma Fibers	6-90-058	C - 2 μm	-
8 - Sigma Fibers	6-90-059	Al_2O_3 - 5 μm	-
6 - Saphikon Fibers	6-90-060	$MoSi_2$ - 5 μm	-
8 - Sigma Fibers	6-90-060	$MoSi_2$ - 5 μm	-
2 - Al_2O_3 Discs	6-90-063	Ta-Ti - 5 nm	Coat One Side
2 - Al_2O_3 Discs	6-90-064	Ta-Ti - 10 nm	Coat One Side
2 - Al_2O_3 Discs	6-90-067	Mo - 2 μm	Double Layer
2 - Al_2O_3 Discs	6-90-068	ZrO_2 - 2 μm	Coating
1 - Al_2O_3 Disc	6-90-068	ZrO_2 - 2 μm	Coat One Side
1 - Al_2O_3 Disc	6-90-068	ZrO_2 - 2 μm	Coat One Side
2 - Al_2O_3 Discs	6-90-069	W - 2 μm	Coat One Side

a Coatings thicknesses are nominal.

b Al_2O_3 wafers, discs, and rods, with a few exceptions, are single crystal sapphire (0001) orientation.

TABLE A2 - MATERIALS COATED[a,b] (3/15/91 - 08/14/92)

NUMBER & TYPE OF SUBSTRATES	COATING RUN NO.	COATING & THICKNESS	NOTES
2 - Sapphire Discs	6-91-022	Ta/Ti - 10 μm	Coating Spalled
2 - Sapphire Discs	6-91-023	Ta/Ti - 1.5 μm	-
2 - Sapphire Discs	6-91-024	Ta/Ti - 2.7 μm	-
11 - Saphikon Fibers	6-91-025	Mo - 3.5 μm	-
3 - Sapphire Rods	6-91-026	C - 0.6 μm	-
70 - Saphikon Fibers	6-91-029	W - 1.5 μm	-
4 - SCS-6 SiC Fibers	6-91-030	W - 1.5 μm	-
2 - Sapphire Discs	6-91-032	Cr - 0.2 μm	-
1 - Sapphire Disc	6-91-035	Mo - 2.0 μm	-
1 - Y_2O_3 Plate	6-91-035	Mo - 2 μm	-
30 - Saphikon Fibers	6-91-035	Mo - 2 μm	Dual Layer Coating
	6-91-036	ZrO_2 - 0.4 μm	-
30 - Saphikon Fibers	6-91-037	W - 0.8 μm	Dual Layer Coating
	6-91-038	ZrO_2 - 0.8 μm	-
2 - Sapphire Discs	6-91-039	Mo - 5 μm	-
31 - Saphikon Fibers	6-91-041	Mo - 1 μm	Single Layer
30 - Saphikon Fibers	6-92-013	Mo - 6 μm	Dual Layer
30 - Saphikon Fibers	6-92-014	SiO_2 - 0.5 μm	
	6-92-015	Y - 1.0 μm	Single Layer
65 m - Saphikon Fiber	A2-92-009	Mo - 0.7 μm	Single Layer
65 m - Saphikon Fiber	A2-92-011	Mo - 0.8 μm	Single Layer
65 m - Saphikon Fiber	A2-92-013B	Mo - 0.25 μm	Single Layer
65 m - Saphikon Fiber	A2-92-016	Mo - 1.5 μm	Dual Layer
65 m - Saphikon Fiber	A2-92-008	Mo - 0.7 μm	
	J920226-05	Al_2O_3 - 1.5 μm	Dual Layer
65 m - Saphikon Fiber	A2-92-010	Mo - 0.8 μm	
	J920303-06	Al_2O_3 - 1.5 μm	Dual Layer
65 m - Saphikon Fiber	A2-92-013A	Mo - 0.2 μm	
	J920312-08	Al_2O_3 - 1 μm	Single Layer
165 m - Saphikon Fiber	A2-92-018	Mo - 1.4 μm	Single Layer
165 m - Saphikon Fiber	A2-92-020	Mo - 0.7 μm	Single Layer
165 m - Saphikon Fiber	A2-92-022	Mo - 0.2 μm	Single Layer
165 m - Saphikon Fiber	A2-92-025	W - 1 μm	Single Layer
165 m - Saphikon Fiber	A2-92-023	W - 0.5 μm	Single Layer
165 m - Saphikon Fiber	A2-92-029	W - 0.2 μm	Single Layer
165 m - Saphikon Fiber	A2-92-017	Mo - 1.4 μm	Dual Layer
	J920402-10	Al_2O_3 - 1 μm	
165 m - Saphikon Fiber	A2-92-021	Mo - 0.7 μm	Dual Layer
	CJ920415-13	Al_2O_3 - 1 μm	
165 m - Saphikon Fiber	A2-92-022	Mo - 0.2 μm	Dual Layer
	CC920422-14	Al_2O_3 - 1 μm	
165 m - Saphikon Fiber	A2-92-025	W - 1 μm	Dual Layer
	CJ92-520-20	Al_2O_3 - 1.5 μm	
165 m - Saphikon Fiber	A2-92-023	W - 0.5 μm	Dual Layer
	CC920424-15	Al_2O_3 - 1.5 μm	
165 m - Saphikon Fiber	A2-92-029	W - 0.2 μm	Dual Layer
	CJ920624-26	W - 1 μm	
165 m - Saphikon Fiber	A2-92-026	Al_2O_3 - 1 μm	Dual Layer
	J920625-27		

a Coatings thicknesses are nominal.

b Al_2O_3 wafers, discs, and rods are single crystal sapphire (0001) orientation.